AC electro-osmosis in nanochannels

Wouter Sparreboom

2009

ISBN: 978-90-365-2815-3

AC electro-osmosis in nanochannels

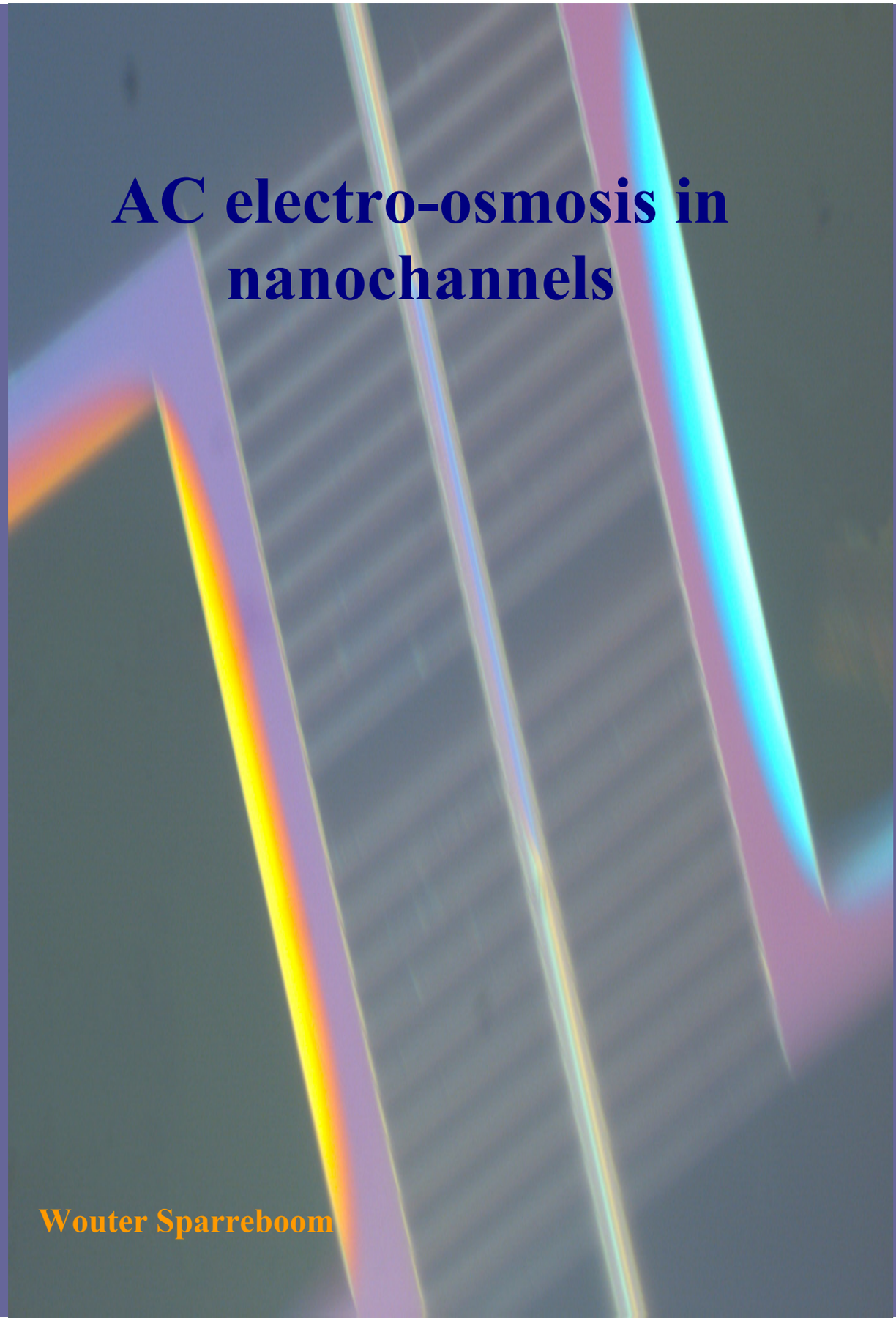

Wouter Sparreboom

AC ELECTRO-OSMOSIS IN NANOCHANNELS

Wouter Sparreboom

Members of the committee:

Chairman	prof. dr. ir. J. van Amerongen	University of Twente
Promotor	prof. dr. ir. A. van den Berg	University of Twente
Assistant promoter	dr. J.C.T. Eijkel	University of Twente
Members	prof. dr. J.G.E.Gardeniers	University of Twente
	prof. dr. ir. P.H. Veltink	University of Twente
	prof. dr. S. Lemay	TU Delft
	prof. dr. H. Morgan	University of Southampton

Sparreboom, Wouter
AC electro-osmosis in nanochannels
PhD thesis University of Twente, Enschede, The Netherlands
ISBN 978-90-365-2815-3

Publisher: Wöhrmann Print Service, Zutphen, The Netherlands

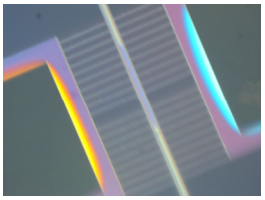

On the cover a photograph of a test structure for the wall integrated electrodes is depicted during etching. The particular color scheme is due to the application of a differential interference contrast (DIC) filter recorded by a color CCD camera. The nanochannel runs from top to bottom while the electrodes are perpendicular to the nanochannel. The part of the channel that has a blue colour is un-etched chromium; the yellow parts on both ends are open nanochannels with the two etch fronts approaching each other.

AC ELECTRO-OSMOSIS IN NANOCHANNELS

PROEFSCHRIFT

ter verkrijging van
de graad van doctor aan de Universiteit Twente,
op gezag van de rector magnificus,
prof. dr. H. Brinksma,
volgens het besluit van het College voor Promoties
in het openbaar te verdedigen
op donderdag 2 april 2009 om 13.15 uur

door

Wouter Sparreboom
geboren op 23 december 1979
te Rheden

Dit proefschrift is goedgekeurd door:

Promotor:	prof. dr. ir. A. van den Berg
Assistent promotor:	dr. J.C.T. Eijkel

Voor mijn meiden

Table of contents

Chapter 1

Scope and outline

In the first chapter the position of the work in the field of Lab-on-Chip or micro-Total Analysis Systems is described. In a second section the background of this project is given. Then the field of AC electro-osmosis is introduced and finally an outline of this thesis is presented.

1.1 Introduction

In the past years the scientific community has gained a lot of knowledge on the downscaling of fluidic systems for biomedical and environmental applications. The miniaturized systems are named Lab-on-Chip (LOC) or micro-Total Analysis Systems (μ-TAS) [1, 2]. In the Netherlands amongst others the BIOS-chair has done a considerable amount of research in this area [3-12].

In the LOC research area mainly microchannels are used (microfluidics), but in the past years the use of nanochannels has become increasingly important (nanofluidics). Nanochannels are generally defined as fluidic channels with a height and/or width that is 100 nm or smaller. Fluidic channels larger than 100 nm but smaller than 1 μm are named sub-micronchannels. This distinction is made here since only below 100 nm behavior of liquid, ions and dissolved molecules begins to deviate from behavior in microchannels. Note that unless stated otherwise aqueous solutions are considered in this thesis. The advantages for both the LOC and the μ-TAS platforms to explore downscaling of (parts of) the system to the nanoscale is interesting since it allows chemistry with unique, ultra-low fluid quantities in the order of femto (10^{-15}) litres. State-of-the-art larger microsystems demonstrated the advantages of miniaturization, such as low chemicals consumption, improved reaction controllability and quality, fast thermal control and improved safety for microreactors, and rapid equilibration, fast mixing and fast separations for microanalysis systems. Downsizing towards nanosystems, furthermore, offers the possibility of increased control of the properties of the enclosed solution, such as its chemistry, electrical potential, temperature, enabling extremely selective chemistry and interrupt reactions by ultra fast thermal control. This increased control becomes possible since the surface to volume ratio increases upon downscaling. Surfaces in nanochannels become increasingly important, also offering new opportunities for use of modified channel surfaces (e.g. by mono layer deposition). Finally, downscaling below 100 nm brings the size of the systems in the order of the length scale over which electrical interactions play a dominant role. This may lead to new phenomena upon the application of electric fields and more importantly new applications.

1.2 Flow sensing and control in nanochannels

This PhD project is named: “Flow sensing and control in nanochannels”. It is part of the Nanoned program. NanoNed is a national nanotechnology R&D initiative that combines the Dutch strengths in nanoscience and technology in a national network with scientifically, economically and socially relevant research and infrastructure projects. The total budget amounts to 235 M€ and the program runs from 2003 until 2009. The Nanoned program is divided into 11 so-called flagships. In these flagships different application areas in which nanotechnology is believed to have an impact are being explored. This project is part of the Nanofluidics flagship. The aim of the Nanofluidics flagship is to investigate, control and exploit new physico-chemical phenomena in structures with nanometer dimensions for use in high-throughput biomolecular characterization. In this PhD project methods for generating and monitoring flow in fluidic channels are reviewed on applicability in nanochannels. Early in the project, based on reviewing available methods, the choice was made to explore AC-

electrokinetic methods to generate flow in microchannels. For flow monitoring also different methods were reviewed, and finally the choice was made to monitor flow electrically.

1.3 AC-electrokinetic pumps

Pumping in nanofluidic channels is challenging, because of the high fluidic resistance. Pressure driven flow velocity scales inversely proportional with channel height squared and is, therefore, hard to practically perform in nanochannels. Therefore, electrokinetic methods seem favorable, because the required electric field does not scale with or depend on channel height. DC-EOF as an electrokinetic method has already received a lot of attention in literature and generally requires high driving voltages, so we chose to look into AC-electrokinetics as a pumping method. Implementing this method in nanochannels is new, and the expectation was that new phenomena would be encountered. In this respect, we were indeed not disappointed. In microchannels, AC-electrokinetics has been performed both at actively controlled wall-integrated electrodes and electrically floating wall-integrated electrodes. In the first method the potential at the electrodes is directly varied by applying sinusoidal potential waves to the electrodes [13-17]. This method is commonly referred to as Alternating Current-Electro-Osmotic Flow (AC-EOF). In the second method the potential at the electrodes is varied by applying a large AC-field along the channel that induces potential differences between the electrodes and the liquid [18-20]. This method is commonly referred to as Induced Charge-Electro-Osmotic Flow (IC-EOF). In this thesis only AC-EOF as a pumping method will be treated. In AC-EOF a flow in the axial direction of a channel is induced by applying a low potential (<5 V) sinusoidal wave to an array of wall-integrated pairs of electrodes. In order to turn such a device into a fluidic pump, asymmetry is needed to generate a net flow. Asymmetry can be implemented in several ways, however, the most often employed method in literature is an asymmetry in electrode size or shape. Another way to implement asymmetry is by applying sinusoidal waves to an array consisting of pairs of three or more electrodes that can be addressed individually. This is in literature referred to as Traveling Wave-Electro Osmotic Flow (TW-EOF) [21]. In this thesis the main focus will be on AC-EOF devices applied to nanochannels with an asymmetry in electrode size. However, in chapter 3 the design and fabrication of a TW-EOF device consisting of an electrode array of pairs of four individually addressable electrodes integrated into the wall of a 50 nm high channel is presented.

1.4 Outline

In this first chapter a general introduction explaining some advantages of nanofluidics is given. Also some details about the project goals and the background of the project are provided. Moreover, since a choice was made for AC-electrokinetic pumps, a brief overview of such systems applied to microchannels was given.

The second chapter reviews methods of generating and monitoring flow and their application to nanochannels. Here, flow does not only consider the flow of liquid molecules, but also that of ions and dissolved molecules and their interaction with one

another and the wall molecules. In this review physico-chemical laws are presented and reviewed on their applicability to flow in nanochannels, indicating the spatial dimension limits of several modeling methods. Using this as background several applications of flow in nanochannels are discussed also providing a section on flow monitoring.

The third chapter describes the design and fabrication of a TW-EOF device. The method described is general for this type of devices and also applies to the fabrication of the AC-EOF devices of which the experimental results are given in chapter 6.

During fabrication of the TW-EOF devices we found out that etching of a chromium sacrificial layer is very much enhanced (>10 times increase in etch rate) by the galvanic coupling of gold electrodes to it. In chapter 4 the exact process parameters of the etching process are given. Moreover, a simple analytical equation for describing and predicting the etch rate is derived and explained. This equation is finally tested experimentally by performing an electrochemical measurement.

Since we found some unexpected experimental results measuring with AC-EOF devices, we decided to make a numerical model to better understand and predict the device behavior. The description of this model is given in chapter 5. Moreover, theoretical results are given by varying several parameters important for device behavior such as applied AC-potential and frequency. The theoretical results show behavior that fundamentally differs from the behavior of AC-EOF microchannel devices, for example a pumping direction opposite to that in microchannels, and twice a flow direction reversal with increasing frequency.

In chapter 6 experimental results are described and discussed. In this chapter the experimental results are compared to the theoretical results described in chapter 5, and found to be roughly in accordance. Moreover, some more background theory necessary for the interpretation of the experimental results is given.

Finally in chapter 7 a summary of conclusions is given. Subsequently, some recommendations are given for future research.

References

1. Manz, A., N. Graber, and H.M. Widmer, *Miniaturized Total Chemical-Analysis Systems - a Novel Concept for Chemical Sensing.* Sensors and Actuators B-Chemical, 1990. **1**(1-6): p. 244-248.
2. van den Berg, A. and T.S.J. Lammerink, *Micro total analysis systems: Microfluidic aspects, integration concept and applications.* Microsystem Technology in Chemistry and Life Science, 1998. **194**: p. 21-49.
3. Bohm, S., *The comprehensive integration of microdialysis membranes and silicon sensors.* Thesis, University of Twente, 2000(ISBN 90-365-1462-2).
4. Emmelkamp, J., *An integrated micro bi-directional dosing system for single cell analysis on-chip.* Thesis, University of Twente, 2007(ISBN 978-90-365-2506-0).
5. Herber, S., *Development of a hydrogel-based carbon dioxide sensor : a tool for diagnosing gastrointestinal ischemia.* Thesis, University of Twente, 2005(ISBN 90-365-2144-0).
6. Krommenhoek, E.E., *Integrated sensor array for on-line monitoring micro bioreactors.* Thesis, University of Twente, 2007(ISBN 978-90-365-2593-0).

7. Langereis, G.R., *An integrated sensor system for monitoring washing processes.* Thesis, University of Twente, 1999(ISBN 90-365-1272-7).
8. Timmer, B.r.H., *AMINA-chip : a miniaturized measurement system for ambient ammonia.* Thesis, University of Twente, 2004(ISBN 90-365-2048-7).
9. Valero, A., *Single cell electroporation on chip.* Thesis, University of Twente, 2006(ISBN 90-365-2416-4).
10. van der Wouden, E.J., *Field effect control of electro-osmotic flow in microfluidic networks.* Thesis, University of Twente, 2006(ISBN 90-365-2453-9).
11. Vrouwe, E.X., *Quantitative microchip capillary electrophoresis for inorganic ion analysis at the point of care.* Thesis, University of Twente, 2005(ISBN 90-9019293-X).
12. Wolbers, F., *Apoptosis chip for drug screening.* Thesis, University of Twente, 2007(ISBN 978-90-365-2499-5).
13. Mpholo, M., C.G. Smith, and A.B.D. Brown, *Low voltage plug flow pumping using anisotropic electrode arrays.* Sensors and Actuators B-Chemical, 2003. **92**(3): p. 262-268.
14. Olesen, L.H., H. Bruus, and A. Ajdari, *ac electrokinetic micropumps: The effect of geometrical confinement, Faradaic current injection, and nonlinear surface capacitance.* Physical Review E, 2006. **73**(5): p. -.
15. Prost, J., et al., *Asymmetric Pumping of Particles.* Physical Review Letters, 1994. **72**(16): p. 2652-2655.
16. Ramos, A., et al., *AC electric-field-induced fluid flow in microelectrodes.* Journal of Colloid and Interface Science, 1999. **217**(2): p. 420-422.
17. Studer, V., et al., *Fabrication of microfluidic devices for AC electrokinetic fluid pumping.* Microelectronic Engineering, 2002. **61-2**: p. 915-920.
18. Bazant, M.Z. and T.M. Squires, *Induced-charge electrokinetic phenomena: Theory and microfluidic applications.* Physical Review Letters, 2004. **92**(6): p. -.
19. Squires, T.M. and M.Z. Bazant, *Induced-charge electro-osmosis.* Journal of Fluid Mechanics, 2004. **509**: p. 217-252.
20. Squires, T.M. and M.Z. Bazant, *Breaking symmetries in induced-charge electro-osmosis and electrophoresis.* Journal of Fluid Mechanics, 2006. **560**: p. 65-101.
21. Ramos, A., et al., *Pumping of liquids with traveling-wave electroosmosis.* Journal of Applied Physics, 2005. **97**(8): p. -.

Chapter 2

Nanofluidic Transport: Principles and Applications

In this chapter transport through nanochannels is assessed, both of liquids and of dissolved molecules or ions. First we review principles of transport at the nanoscale, which will involve the identification of important length scales where transitions in behavior occur. We also present several important consequences that a high surface to volume ratio has on transport. We review liquid slip, chemical equilibria between solution and wall molecules, molecular adsorption to the channel walls and wall surface roughness.

In a second section, recent developments and trends in the field of nanofluidics are identified, key differences with microfluidic transport addressed and applications reviewed. Hereby novel opportunities are accentuated, enabled by the unique behavior of liquids at the nanoscale.

2.1 Introduction

During the past two decades there has been a tremendous development in microfluidics. Initially the focus was on the investigation and characterization of special features of classical fluidics and analytical chemical phenomena, such as transport, mixing, dosing and separation. Later the accent shifted towards a large variety of relevant new applications, for example in the fields of analytical and clinical chemistry and biochemistry. More recently, with most microfluidic phenomena well-characterized, research has moved to nanofluidic phenomena. Here, nanofluidic is defined as fluid motion through or past structures with a size in one or more dimensions in the 0-100 nm range. This was at least driven by the following observations. First, an important motivation has been the wish to replace entangled polymers (which are typically used for gel-based DNA separations) by an engineered solid state version [1]. The free volume in such polymers typically had a dimension of a few nanometers up to around a micron. Second, it was realized that interesting new phenomena were to be expected when fluidic dimensions go down to or below the characteristic dimensions determining the mechanical (fluidic slip length) or electrochemical (electrical double) behavior. These unique phenomena observed in nanofluidic systems, mostly stem from exploitation of fluid interactions with the walls, which are very prominent, because of the large surface to volume ration that is inherent to nanofluidics. Third, recent nanofabrication allows for engineering both one- and two-dimensional nano-confinements. Fourth and final, nanofluidic devices provide new tools to investigate and describe fluid behavior on the nanometer scale, and thus enables the coupling of macroscopic continuum descriptions and microscopic molecular dynamics descriptions in real devices.

Although nanofluidics is a reasonably young research field, in the last decade the number of publications on nanofluidics has doubled every two years, indeed indicating a strongly increasing interest in nanofluidics. And while in recent years several reviews in the nanofluidics field have appeared, none have reviewed the basic principles of transport of both liquids and dissolved molecules or ions at the nanofluidic scale. In ref. [2] nanofluidics in general is reviewed, mainly discussing the state of the art and philosophizing about future devices and opportunities. Others discussed technological issues [3-5] and recently also two reviews dedicated mainly to electrokinetic transport in nanochannels have been published [6,7]. The aim of this chapter is discussing the basic principles of nanofluidic transport and from this perspective review recent applications in nanofluidics. In the first section theory and models will be described that are used to describe transport in nanochannels. In this section key differences with transport in microchannels will be addressed. In the next section developments and trends in nanofluidic transport are discussed. This section will be divided into two subsections: flow detection and applications. Finally, there will be a conclusion and an outlook into future devices employing nanofluidic transport.

2.2 Theory

Modeling of transport in nanofluidic systems differs from microfluidic systems because changes in transport caused by the walls become more dominant and the fluid consists of fewer molecules. This has consequences on the applicability of models used to describe microfluidic transport. Therefore, in this section we will present different models used in microfluidics and discuss their applicability for nanofluidic transport. Also, electrokinetic transport differs from that in microfluidic systems because the influence of the electrical double layer is more prominent. Finally, because of the large surface to volume ratio in nanofluidic systems a subsection dedicated to wall effects is included.

2.2.1 Continuum or discrete modeling

Since a cubic nanometer of a typical solvent such as water contains less than 50 molecules, the discrete nature of molecules can become important when considering nanofluidic transport. This means that modeling of such a system by applying continuum equations may lead to errors and individual molecules and interaction amongst them need to be considered. This can be done by molecular dynamics simulations, wherein only van der Waals and electrostatic interactions are considered. Since the pioneering work of Alder and Wainwright in 1959 [8] in recent years an explosive increase in the number of publications using molecular dynamics simulations and their influence on nanofluidic transport [9-29] can be noticed. The reason for this is probably twofold. First, technology for fabricating nanofluidic devices has matured a lot in the last decade, whereas before nanofluidic phenomena were mainly studied in membrane science [30] and in colloid and interface science [2,31]. Secondly, computational capacity has increased exponentially, resulting in the ability to simulate the behavior of millions of molecules, instead of the several hundreds of Alder and Wainwright. However as pointed out by Succi et al.[32], when considering fluid transport, the difference between continuum modeling and discrete modeling is small and is usually limited to deviating behavior of a few molecular layers into the liquid. In the following subsection more comparisons will be made between continuum and discrete modeling. Consequences for both liquid and electrokinetic transport will be discussed. For more information on different modeling techniques for fluid mechanics we refer to ref. [33].

2.2.2 Transport equations

2.2.2.1 Liquid transport

As is known from microfluidics, the physics describing transport in fluidic channels is somewhat altered to that used in modeling macroscale device behavior. That is, the ratios of competing physical processes changes as a function of characteristic device length, causing different physical processes to be dominant at different length scales. A way of estimating the order of magnitude of the influence of different processes on transport is using dimensionless numbers. Dimensionless numbers originate from well-

known equations describing flow, such as the Navier-Stokes [34] equations. In [2] the most important dimensionless numbers for mass transport in nanofluidic systems are reviewed. The main conclusion that can be drawn from applying dimensionless numbers to nanofluidics is that gravitational and inertial forces are dominated by viscous and surface tension forces. Since in this chapter only single phase transport is considered, the effects of surface tension forces in nanofluidics will not specifically be considered. In [35] a review on multiphase flows in nanochannels can be found. The fact that viscous interactions dominate over inertial forces is expressed in a low Reynolds number [2] and already applies on the microfluidics length scale. Since Reynolds numbers typically encountered in microfluidic systems are smaller than 1, flow at the microscale is generally accepted to show laminar viscous or simply Stokes flow. For nanochannels with one of their dimensions smaller than 100 nm this rule of thumb holds for velocities even beyond 1 $m.s^{-1}$ which are highly unlikely for nanochannels with zero or little slip velocity at their walls [36].

However, to apply Stokes flow for modeling liquid transport in nanochannels, also the assumptions made for the derivation of the full Navier-Stokes equations need to be examined. These assumptions are: First, the fluid is assumed to be a continuum. Second, viscosity is assumed to be independent of the shear rate (i.e. the fluid is Newtonian). Furthermore, the fluid can be assumed to be incompressible (the equations then are often referred to as the Navier-Stokes equations for incompressible flow). Well known and often used equations used to calculate fluidic resistance in microfluidics [37] are, amongst other assumptions all based on the assumption of incompressible flow.

The applicability of continuum theory is often checked by introducing the Knudsen number. For gases this is the ratio of the mean free path of a molecule and the system characteristic length, L.

$$Kn = \frac{l}{L} \tag{1}$$

In liquids however, the molecules are densely packed and a mean free path is not a meaningful quantity. For liquids therefore l is defined as the interaction length. This interaction length is based on the number of molecules with which a molecule of interest interacts. As a rule of thumb 10 molecular lengths is used for l. If we substitute l in equation (1) with the interaction length for water and define a Kn-value of 1 to correspond with the transition between continuum and discrete flow, the continuum approach can be applied to channels or processes inside a larger channel with a characteristic length down to ~3 nm. Later in this chapter we show that this rule of thumb value for transition in behavior appears to be very close to theoretical and empirical values found in literature.

The next assumption for the Navier-Stokes equation is that the liquid is Newtonian. As mentioned above interactions of solute molecules with the walls are dominant in nanofluidics, therefore, shear rates might become more important for the description of liquid flow behavior. As proposed and checked via molecular dynamics simulations by Loose and Hess [38] liquids act Newtonian up to strain rates twice the molecular frequency, $1/\tau$, which is defined below.

$$\gamma = \frac{\partial u}{\partial y} \geq \frac{2}{\tau}$$
$$\tau = \sqrt{\frac{m\sigma^2}{\varepsilon}} \quad (2)$$

Here γ [s^{-1}] represent the shear rate, u and y represent the axial velocity and the perpendicular coordinate, respectively; τ is the time-scale on which molecular movement occurs; m [$kg.mol^{-1}$] represents the molecular mass; σ [m] is the molecular length scale and ε [J/mol] equals the product of Avogadro's number, N_A [mol^{-1}], Boltzmann´s constant, k [$J.K^{-1}$]and the absolute temperature T [K] and represents the molecular energy scale. The above is based on the Lennard-Jones model [39]. In [40-55] the Lennard-Jones parameters for water are determined using different water models. From this the average σ and ε are determined to be $3.16*10^{-10}$ m and 690 $J.mol^{-1}$, respectively. This results in a molecular characteristic time in the order of a picosecond and a maximum shear rate of $1.24*10^{12}$ s^{-1}. This compares approximately to a gradient in velocity of 400 $m.s^{-1}$ across a single molecular layer. Since encountered velocities in nanochannels with zero slip at their walls (the zero slip condition will be explained below) are typically much smaller (i.e. in the order of 1 $mm.s^{-1}$), the break-up of the Newtonian assumption is not likely to occur. However, although this observation is already based on molecular interactions, Qiao and Aluru [11] show in molecular dynamics simulations that for a channel having a width of 4 to 5 (~1.5 nm) molecular layers the Newtonian assumption does break down. Induced flow rates presented in [11] are, however, unpractically high, which causes much higher shear rates than experimentally assumable.

Finally, since required pressure differences to drive liquids through nanochannels are high the influence of incompressibility also needs to be assessed. The compressibility of water [56] predicts an approximate 1% volume decrease of water per 20 MPa, which for a constant cross-section results in a 1% decrease in water column length. This is considerably small and will only have an effect at high applied pressures (> 10 MPa) if the influence of changes in dynamical pressure variations on transport are assessed.

The conclusion from the above analysis is, that for channels with both perpendicular dimensions at least 10 nm, Stokes flow can reasonably well be applied. Mathematically Stokes flow is described as:

$$\eta\nabla^2 u + f = \nabla P \quad (3)$$

Here η [Pa.s] represents the viscosity; u [$m.s^{-1}$] the linear velocity; f [$N.m^{-3}$] a body force exerted on the liquid molecules and ∇P [Pa] the applied pressure gradient. For f in equation (3) any force acting on the volume of liquid inside the channel can be substituted. For example, to obtain f in the case an electric field is applied, the electric field strength is multiplied by the net charge inside the channel volume to obtain the Coulomb force.

For Stokes flow the velocity profile of a cross-section perpendicular to the channel wall is governed solely by viscous forces, is continuous and can be described by

neighboring laminae of approximately equal speed shearing along each other. As in microchannels, each channel geometry has its own velocity profile and therewith its own equivalent fluidic resistance. Here, only the solutions for the velocity profile, $\tilde{u}$, and the fluidic resistance, R, between two infinite parallel plates and inside a cylindrical capillary will be given which are commonly referred to as Poiseuille flow [57,58].

Parallel plate a: half distance between plates b: width of the plates	Cylindrical capillary a: radius
$\tilde{u} = \frac{1}{2}\left(x^2 - a^2\right)$	$\tilde{u} = \frac{1}{2}\left(r^2 - a^2\right)$
$R = \frac{3\eta L}{2a^3 b}$	$R = \frac{8\eta L}{\pi a^4}$

(4)

Velocity profiles and fluidic resistances of more exotic channel geometries can be found in textbooks such as [57-59].

For nanofluidic devices or parts of interest of larger systems that are smaller than ~10 nm, some of the above assumptions do not apply and the influence of individual molecules needs to be considered. This can be done either in a molecular dynamics fashion or by discretizing important parameters such as the viscosity per molecular layer adjacent to the channel wall. Here the former method has the advantage that no assumptions are made concerning the shape of the flow profile and other macro parameters such as for example viscosity, which immediately also entails a disadvantage because of the large number of degrees of freedom and thus computational time needed. The latter had the advantage of fewer degrees of freedom and therefore larger systems can be considered. However, it has the disadvantage that assumptions are made about the viscosity distribution a priori. Qiao and Aluru [11] discus both possibilities using both molecular dynamics simulations and continuum modeling in the case of electro-osmotic flow. Boundaries in terms of channel heights for continuum, modified continuum (both modified ionic interactions and a viscosity change at the walls was incorporated) and molecular dynamics modeling are given in table 1.

The general trend following from [11] is that continuum modeling tends to overestimate flow rates in case of electro-osmotically driven flows. The reason for this is that water and ion layering and thus density changes at the walls are not taken into account. This in turn gives rise to an overestimation of mobile counter-ionic charge concentrations and according to several sources [13,60-62] also to an increase in viscosity. Zhang et al. [63] report on similar density and corresponding viscosity changes for pressure driven flow. Their conclusion is that in nanofluidic systems of a five molecular layer diameter or smaller viscosity changes are very dominant and will alter the Poiseuille flow profile drastically. Another important conclusion from their work is that systems consisting of a more dense liquid (e.g. electrolytes) the effects are more pronounced. These computational results compare well to empirical findings of Israelachvili and Pashley [64,65]. In their experiments Israelachvili and Pashley

observed discrete water layering by fluctuations in surface force obtained via surface force measurements on KCl solutions at mica surfaces.

Table 1: Modeling strategies for different size regimes according to [32]

Channel height, h [nm]	Type of model	Breakdown of which assumption?
h>10	Continuum	/
<2h<10	Modified continuum using molecular dynamics results	Continuum, since liquid and ionic parameter vary across the channel height
h<1.5	Molecular dynamics	Water becomes non-Newtonian*

*In [11] very high field strengths (550 $MV.m^{-1}$) are used as compared to most experiments. This causes a velocity in the order of tens of $m.s^{-1}$ which is, although much higher than that practically applied (i.e. often in the order of 100 $kV.m^{-1}$), somewhat lower than the limit posed by Loose and Hess [38] discussed above. However, since the influence of the high applied velocities on the breakdown of the Newtonian assumption is not discussed, it is not clear if this breakdown would also occur for more practical flow velocities.

Although continuum modeling might not always give accurate results, it provides a good tool for estimating the order of magnitude of different competing physical processes. As a result it is useful in assessing different methods of generating fluid transport in nanochannels. It must be remarked that the above considerations only applied for ideally flat walls with no-slip conditions and without surface adsorption. In section 2.3 the influence of the walls will be taken into account and deviations from the above described behavior will be treated, mainly caused by a non-zero velocity at the walls.

2.2.2.2 The electrical double layer

The previous subsection showed that deviations from continuum theory describing liquid flow can be found in systems smaller than 10 nm. In this subsection the influences of confinement on ionic distributions will be shown.

In this subsection glass walls and aqueous solutions around neutral pH will be assumed. Since a glass wall at its interface consists of amphoteric silanol (SiOH) groups it can be (de)-protonated as a function of pH, which is typically described using a site binding or dissociation model such as described in refs. [66,67]. This causes the walls to be charged which can be described by a constant wall potential model, a constant surface charge density model or a constant surface charge density model which takes the chemical equilibrium into account [68]. In this subsection mainly the constant wall potential model will be used, the other boundary conditions will be treated in the next subsection where wall effects are discussed.

To determine the concentration of ions inside a nanochannel the potential profile in the so-called electrical double layer (EDL) needs to be calculated. This is usually done by coupling the Poisson and the Boltzmann equation as shown in equation (5).

$$-\nabla^2\psi = \frac{e}{\varepsilon}\sum_i c_i z_i \exp\left[\frac{-z_i e\psi}{kT}\right] \tag{5}$$

Here, $\nabla^2\psi$ [V.m^{-2}] represents the divergence of the gradient in electrostatic potential, which can for parallel flat walls be reduced to the second derivative with respect to the perpendicular coordinate y [m] (i.e. $d^2\psi/dy^2$); ε [F.m^{-1}] represents the permittivity of the liquid; e [C] is the unit charge; c_i [mol.m^{-3}] and z_i [.] are the concentration and the ionic valence of the i^{th} ionic species, respectively; ψ [V.m^{-2}] represents the electrostatic potential and k [J.K^{-1}] and T [K] represent Boltzmann's constant and temperature, respectively. By linearizing equation (5) (i.e. assuming $ze\psi<<kT$) and solving for a 1/exp(1) decay in potential (i.e. corresponding to a situation where the potential energy equals the thermal energy) the typical distance over which the Coulomb interactions are dominant over the thermal interactions is defined. The result is named the Debye length and is often used as a rule of thumb.

$$\lambda_D = \sqrt{\frac{\varepsilon kT}{\sum_i N_A c_i {z_i}^2 e^2}} \tag{6}$$

Here N_A [mol^{-1}] is Avogadro's number and the rest of the variables and constants is defined as above. For systems with walls that are separated over a distance on the order of λ_D, ion enrichment and exclusion effects are particularly strong (though they can already occur in larger channels). In such systems the concentration of ions that are oppositely charged to the wall or counter-ions can be orders of magnitude larger than that of ions of equal charge or co-ions. Plecis et al. [69] considered ion enrichment and exclusion in detail, providing both theory and experimental results. This situation is generally referred to as double layer overlap. If the EDLs hardly overlap, which is defined as $8\lambda_D \leq h$, and the electrolyte is symmetric (i.e. $z_+ = z_-$) the electrostatic potential perpendicular to two infinite parallel walls can be described as a superposition of the potential distributions of both walls as follows [7].

$$\psi(y) = \frac{4kT}{ze}\left(\tanh^{-1}\left[\tanh\left(\frac{ze\zeta}{4kT}\right)\exp\left(-\frac{y}{\lambda_D}\right)\right] + \tanh^{-1}\left[\tanh\left(\frac{ze\zeta}{4kT}\right)\exp\left(-\frac{h-y}{\lambda_D}\right)\right]\right) \tag{7}$$

Here, y [m] is the coordinate in the direction perpendicular to the channel wall and ζ [V] equals the potential at the wall. Equation (7) is named the Gouy-Chapman equation. To calculate the potential profiles in the case of an asymmetric electrolyte Gouy and Chapman developed special functions that make equation (7) compatible for calculations with asymmetric electrolytes. The solutions are repeated in for example [7,61]. If one does not want to perform numerical simulations and still wants to know

the potential distribution in systems with strongly overlapping EDLs (i.e. $2\lambda_D \geq h$) the Debye-Hückel approximation can be applied [61,69,70]. This is a linearization of the Poisson-Boltzmann problem and is by definition only valid for $|\zeta| \leq 25$ mV.

$$\psi(y) = \frac{\zeta \cosh\left(\frac{\frac{h}{2} - y}{\lambda_D}\right)}{\cosh\left(\frac{h}{2\lambda_D}\right)} \tag{8}$$

From equation (8) the ionic distribution of ionic species i, $\tilde{c}_i$ [mol.m^{-3}], can be easily calculated using the Boltzmann equation.

$$\tilde{c}_i = c_i \exp\left[\frac{-z_i e \psi}{kT}\right] \tag{9}$$

To assess the error due to the use of the Debye-Hückel approximation on the predicted ion concentrations and potential distribution at zeta potentials higher than 25 mV, Conlisk [71] made an extensive comparison between the analytical results obtained by applying the Debye-Hückel approximation and numerical results. The conclusion is that errors up to 30% are made for zeta potentials higher than 25 mV.

2.2.2.3 Electro-osmotic flow

In nanochannels axial liquid transport can be induced by applying an axial electric field, just as in microchannels. This field displaces the ions in the EDL in a process called electro-osmosis. For nanochannels without double layer overlap the well-known Helmholtz-Smoluchowski equation can be applied to determine the flow velocity in the electroneutral bulk. This is a linear analytical solution of the Poisson-Boltzmann and the Stokes equation.

$$u = -\frac{\varepsilon \zeta E}{\eta} \tag{10}$$

The flow profile in the non-electroneutral double layer is defined by introducing a potential-dependent scalar into equation (10) resulting in equation (11)

$$u = -\frac{\varepsilon \zeta E}{\eta}\left[1 - \frac{\psi(y)}{\zeta}\right] \tag{11}$$

As proposed by Burgreen and Nakache [70] this scalar can be integrated over the double layer thickness resulting in a proportionality constant, G, that describes reduced flow as compared to non-overlapped electro-osmotic flow as a function of the amount of EDL overlap.

$$G = \frac{2\lambda_D}{h}\int_0^{h/2}\frac{\psi(y)}{\zeta}d\left(y/\lambda_D\right) \tag{12}$$

G has to be calculated numerically which is done by Burgreen and Nakache. Infinite series solutions of the problem are given by Levine et al. [72]. A comparable proportionality constant is determined for 40 nm and 100 nm channels both numerically and experimentally by Pennathur et al. [73-76] for a range of different electrolyte concentrations and hence amounts of EDL overlap.

2.2.2.4 Ionic and molecular transport

Ionic transport, J [mol.s^{-1}.m^{-2}] is usually assessed by the Nernst-Planck equations (13)

$$J_i = -D_i\left(\nabla c_i + \frac{z_i q}{kT}c_i\nabla\psi\right) + c_i u \tag{13}$$

Here, D_i [m^2.s^{-1}] is the diffusion constant and c_i [mol.m^{-3}] represents the molar concentration. The first term represents the contribution of diffusion and electro-migration to the molar flux. The second term represents convective contributions and can in case of electro-osmotic flow be used to assess the ionic transport by substituting equation (11) into (13). Due to the difference in ionic distribution between microchannels or reservoirs and nanochannels which is caused by the presence of the electrical double layer as discussed above, a number of specific transport phenomena occur. At the interface between micro and nano a flux gradient exists for ionic species due to their sudden spatial change in concentration, which will give rise to so-called concentration polarization. On one side of the nanochannel the salt concentration will rise and on the other side decrease. This phenomenon, since long known from membrane science and colloid chemistry, has also been demonstrated in nanochannels [77]. Another phenomenon that becomes important in small channels is surface conduction. Since the ionic concentration in the electrical double layer is higher than in the liquid bulk, the contribution of the conduction in the double layer, the so-called surface conduction, increases on downscaling. This phenomenon, also widely known in physical and colloid chemistry, has recently also been investigated for nanochannels [78].

Apart from the molecular charge, transport of all molecules including charged molecules through nanochannels is affected by the molecular size with respect to the lateral channel dimensions and also by considerations of molecular entropy. Molecules can be excluded from channels by ion exclusion, by steric hindrance or because the cost in internal entropy. On the basis of these three factors nanochannels work as molecular sieves which are much like membranes or sieves. These aspects have recently been reviewed by one of the authors [79] and also extensively by the group of Han [80]. Some more details will be given in the section on molecular separation.

2.2.2.5 Modeling ionic transport

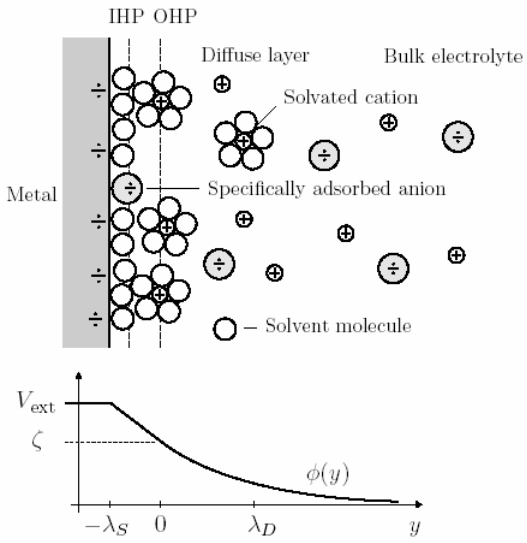

Figure 1: Schematic picture of the diffuse double layer in the electrolyte next to a negatively biased metal electrode. Cations are attracted to the electrode and anions are repelled so the interface appears charge neutral when seen from the bulk. The outer Helmholtz plane (OHP) defines the closest distance that the solvated cations can move towards the electrode. Also shown is φ(y), the mean-field potential variation from the electrode to the charge neutral bulk.

All theory concerning electrokinetics given above boils down to two equations, namely the Poisson-Boltzmann equation to describe the electrical double layer and the Nernst-Planck equation to describe ionic transport. Both equations are continuum equations and should thus be tested on their applicability to ionic transport in nanochannels. This can be done by comparing continuum results with molecular dynamic results. Furthermore, the Nernst-Planck equation is valid for a dilute electrolyte solution (i.e. ions do not influence each other) and just as the Poisson-Boltzmann theory considers ions to be ideal point sources with an infinitely small size. Over the years different patches have been developed to overcome these assumptions. The limitation posed by the dilute electrolyte assumption is usually circumvented by using empirical activity constants instead of concentrations [34,81]. These activity constants are strongly dependent on ion type and can decrease the effective transport rate up to 20 times for a 1 M solution [56] as compared to dilute solutions. Changes of a few percent can already be expected at concentrations of 500 μM [56]. The influence of a finite ion size is in case of EDL theory often implemented by a Stern modification [34,81]. By using the Stern modification one assumes that ions are hydrated and because of that have a minimum distance of approach to the wall surface. Here, the Stern model stems from the more elaborate Helmholtz model which is shown in

combination with the diffuse Gouy-Chapman model in figure 1. Other models that take the finite size and the interaction of different ions into account are those who model steric effects. A recent review of these models and its implications for the Poisson-Nernst-Planck equations by Kilic et al. is found in [82,83]. The question whether electrokinetics in nanochannels ought to be modeled taking molecular dynamics into account is answered in refs. [11,84]. The general conclusion is that molecular behavior should be taken into account to model electrokinetics in systems consisting of 10 molecular layers (~3 nm) or less. The reason for this is that strong density fluctuations of species (i.e. water molecules and ions) in the first few molecular layers adjacent to the wall cause strong deviations from Poisson-Boltzmann theory. Furthermore, using the results from molecular dynamics simulations and plugging them as lumped parameters into the Poisson-Boltzmann and Stokes equations (the modified continuum model mentioned in subsection 2.2.1) is beneficial in modeling electrokinetic behavior in larger nanofluidic systems (3-10 nm).

2.2.2.6 Modeling molecular transport

Also molecular transport can be modeled using the Nernst-Planck equations. However, diffusion and migration often need to be assessed separately employing modified diffusion and electrophoretic mobility constants. For example, Balducci et al. describe modified diffusion of double stranded DNA molecules in 100 nm high nanoslits [85]. Ajdari and Prost present a model to account for modified electrophoretic mobility of DNA molecules [86]. And Salieb-Beugelaar, Teapal et al. report on retardation effects in electrophoretic transport of 48 bp DNA molecules in 20 nm high nanoslits at higher electric fields (>30 $kV.m^{-1}$) [87]. In all cases interactions with walls and entropic effects will have to be taken into account and will have an influence on all three transport meganisms, also convection which is of course known from chromatography. Once modified transport constants are found, their influence can be assessed by substitution into (in case of diffusion and electrophoresis) and scaling (in case of convection) of the Nernst-Planck equations.

2.2.3 Wall effects

As mentioned in the introduction, effects that happen at the channel walls become increasingly important when decreasing channel height. Typical examples of these effects are the occurrence of EDLs, slip [57, 109] and specific adsorption effects [89-93]. Moreover, also surface roughness can have a pronounced effect on transport properties. For example, Qiao et al. [17] performed molecular dynamics simulations and found that surface roughness can strongly affect electro-osmotic flow (causing up to 50 % decrease in velocity). Another example is the large flow enhancements found by Cotin-Bizonne [94] that occur because of increased slip due to air trapped at hydrophobic walls caused by a large surface roughness. A wall effect that up to now has hardly received attention in nanofluidic literature is the chemical equilibrium between surface silanol (SiOH) groups and the liquid. The authors strongly believe that this equilibrium will have a profound effect on so-called gating as done in nanofluidic transistors first described in a synthetic nanochannel by Karnik et al. [95] since the equilibrium can be shifted by applying a different potential at the wall. This shift in equilibrium will result in a strong release or uptake of protons inside the liquid thereby

changing pH and thus influencing the resulting wall potential. Indeed recent experiments reported by Jansen et al. [96] indicate a large proton release from nanochannel walls on capillary filling, acidifying the filling solution and titrating its constituents. Moreover, since protons are highly conductive, proton uptake or release by the wall can strongly affect the conductivity of the liquid, as discussed by van der Heyden et al. [68]. These authors found that replacing the constant potential or constant surface charge condition by a chemical equilibrium condition leads to the best fit with the experimental surface conduction data.

In the following sections the influence on transport of slip and adsorption effects will be discussed.

2.2.3.1 Liquid slip

In this subsection the influence of a non-zero velocity of liquid molecules at the channel wall (also known as liquid slip) will be discussed. Whereas no slip represents a situation where the liquid in the first molecular layer is stagnant and all other molecules are sheared past the first molecular layer, the first molecular layer does move in slip flow, though with strong friction with the wall. The lower this friction with the wall, for example by employing very hydrophobic walls, the less force is needed for a given flow velocity. Therefore, slip is very important in nanofluidics since it drastically reduces the required pressure in pressure driven flows. Whitby and Quirke review very low-friction flows in carbon nanotubes and nanopipes and discuss several approaches to a functional device in ref. [97].

It has theoretically been predicted for some time that also electro-osmotic flow would be strongly enhanced in the case of slip, and recently the first experimental evidence for this was found [98-100]. A theoretical case has also been made for strong flow enhancements in the case of diffusio-osmosis [101]. The fact that effects of slip are far more pronounced in nanochannels than in microchannels can be seen in equation 14, describing the average fluid velocity due to an applied pressure gradient in a rectangular channel of width >> height [102].

$$u = \frac{h^2}{12\eta}\left(-\frac{dP}{dx}\right)\left(1+\frac{6b}{h}\right) \tag{14}$$

Here a pressure difference, *dP/dx* is applied in the axial direction of the channels. *b* represents the slip length and is defined in figure 2. Comparable equations can be written down for electro-osmotic flow and diffusio-osmosis, with the difference that the channel height is replaced by respectively the Debye length and a length characterizing a molecular adsorption layer.

Recently one of the authors discussed the consequences of liquid slip on micro- and nanofluidics [36]. For reasons of clarity a figure from this paper is repeated, originally stemming from [103]. In figure 2 the consequences of slip on the velocity of liquid are clearly shown. The case on the right is particularly educational, because it represents a situation where liquid does not experience any friction with the wall and could theoretically be accelerated to the speed of light.

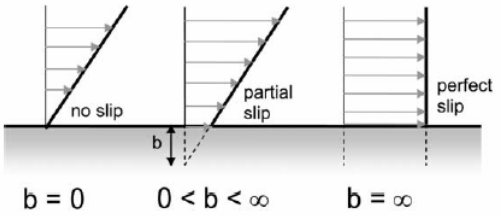

Figure 2: Three cases of slip flow past a stationary surface. The slip length b is indicated. Drawing after Lauga et al. [103]

Parameters that are known to influence slip in nanochannels are surface roughness and hydrophobicity [94,104]. Generally, the slip length is increased for increasing hydrophobicity and decreasing surface roughness when the channel walls are hydrophilic. There, however, is convincing evidence that surface roughness in case of hydrophobic channels leads to greater slip lengths (several tens of microns as compared to around 20 nm for smooth hydrophobic channels) because of air trapping in surface inhomogeneities [94]. For more detailed information on slip flow we refer to [36] and references therein.

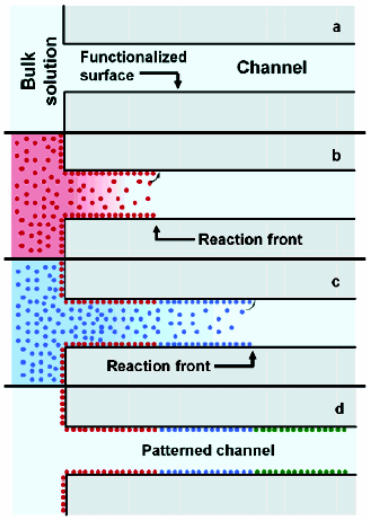

Figure 3: Diffusion-limited patterning (DLP). (a) DLP requires a channel that is accessible to the bulk solution only from its entrance. The surface is functionalized, so that reactants can bind to the channel surface. (b) Once a reactant (red) is introduced into the bulk solution, it diffuses into the channel, forming a sharp reaction front under certain conditions. (c) When a second reactant (blue) is introduced, it reacts with the region of the channel beyond the first reactant. (d) Repeating this process with different reactants results in patterning of the reactants inside the channel. Reprinted from [91]

2.2.3.2 Wall adsorption

In nanofluidic channels where the lateral dimension is often orders of magnitude smaller than the axial dimension, the effects of lateral diffusion are much more pronounced than in microfluidic channels. On transport through a nanochannel the frequency with which a molecule will hit a wall by lateral diffusion is greatly increased with respect to microchannels, since this frequency scales with $1/h^2$.

The tendency of molecules to adsorb on the channel wall material when they encounter it, can lead to a large decrease in transport rate of such molecules in a process equivalent to liquid chromatography [105]. This observation is reflected in the number of publications that appeared in recent years concerning modified transport in nanochannels of mainly cationic molecules [89-93,106]. On diffusion of adsorbing molecules through a nanochannel, the reduced transport rate is accompanied by a sharply defined diffusion front. Karnik et al. [91] demonstrate that this effect can be used to precisely pattern the surface of nanofluidic channels. The same phenomenon had previously been described by Delamarche for microchannel patterning [107]. In figure 3 a schematic drawing of this application is shown. Karnik et al. also present an analytical model to account for altered diffusion, introducing a modified diffusion constant that describes the change in transport as a function of cross sectional area, perimeter, surface density of adsorbed species and the concentration of the molecule under consideration at the channel entrance. Experimental evidence for transport rates in nanochannels supports this, and for proteins and positively charged dyes diffusion constants were reported that were from 4 orders of magnitude [90] to even 8 orders of magnitude [89] lower as compared to tabulated bulk values. These dramatic changes will for example have a profound influence in using such molecules as tracer molecules to assess the flow velocity, rendering this approach practically impossible.

2.3 Applications

In this section several applications of transport in nanochannels will be treated. Technology concerning the fabrication of nanofluidic devices employing transport will not be treated here, since already several extensive reviews on this subject have appeared [3-5]. Since in most cases transport needs to be assessed, in the first subsection flow detection methods will be reviewed on applicability to flow at the nanoscale. In the next subsection several applications found in literature will be treated. Often found applications range from pumping and transport control to energy conversion and separation of analytes.

2.3.1 Flow detection

In this subsection the detection of transport in nanochannels will be discussed. Whereas flow detection in microchannels often has evolved from macro-scale methods, flow detection in nanochannels is expected to run into more fundamental problems such as the minimal spatial resolution of around 300 nm for visible light [108]. This limiting spatial resolution prevents the detection of flow profiles across the height of the channel, but could possibly be improved by combining evanescent wave illumination and particle image velocimetry (PIV) as first discussed by Zettner and Yoda in 2003 [109]. Recently Bouziques et al. applied total internal reflection

fluorescence to perform PIV in a 200 nm thin layer adjacent to a microchannel wall [100]. A limited spatial resolution is however not the only problem experimental nanofluidics researchers are bound to encounter. Since transport in microchannels is often assessed by particle based visualization techniques (such as PIV), effects posed by the channel walls will certainly influence transport of such particles. Since nanochannel walls are often negatively charged, introduced particles have to be negatively charged to prevent sticking to the wall and as a consequence clogging of the channel. This will complicate introducing such particles into nanochannels, since equally charged particles and walls will lead to a high possibility of exclusion of the particle, dependent on the ionic strength. Electrical repulsion from the walls will furthermore cause particle enrichment in the center of the channel. Using physiological strength electrolytes, this limits the applicability of such techniques to channels larger than ~10 nm. Another very obvious problem is the limited minimal size of particles that are currently available which is currently around a few nanometer.

Moreover, there is also a limited applicability of tracer molecules to visualize microchannel flows. As mentioned in the previous section for particles, molecules of opposite or neutral charge adsorb to the wall. Same-charge molecules, however, can be excluded resulting in concentration reductions of several orders of magnitude as discussed in section 2.2.2, resulting in the need for a very low detection limit of the detector used (mostly fluorescent). To further complicate matters, neutral fluorescent molecules tend to be insoluble in water, making the application of such very limited. Modeling of the reduced transport properties with the model of Karnik et al. as discussed in section 2.3.2 could provide a way to indirectly determine flow properties using positively charged dye molecules. It should be noted, however, that adsorption of positively charged dye molecules to the wall is likely to decrease electro-osmotic flow drastically by decreasing the wall potential.

Other flow sensing methods employed in microchannels found in literature [108] are time of flight techniques such as heating of a small cross-sectional segment of liquid and subsequent detection downstream. Here the distance between the heat actuator and detector divided by the time between the application of the heat pulse and the detection is a measure of the time and space integrated velocity of liquid in the channel. The applicability of this technique to nanochannel flows is questionable since the induced temperature gradient is likely to be diminished by heat transfer to the walls which is very efficient in large surface to volume systems. Finally, Mela et al. [110] apply the current monitoring technique successfully to assess nanochannel electro-osmotic flow. This technique is also a time of flight technique and is done by measuring the time it takes to refresh an electrolyte of a given strength with another one having a different strength by measuring the current along the channel. This technique is often applied as a calibration technique for other flow visualization techniques [108] and was first described by Huang and co-workers [111] to assess the electro-osmotic flow rate in capillary zone electrophoresis. This technique is, however, only useful in obtaining a temporal and spatial average. Furthermore, its applicability is limited to electrolyte strengths and channels that are high enough such that surface conduction does not determine the axial conductivity of the channel. Stein et al. [78] show that surface conduction for 70 nm channels already becomes dominant for salt concentrations below 4 mM. Extrapolating the experimental data in [78] limits the applicability of the current monitoring technique to monitor nanochannel flows for

physiological solutions to a channel height of approximately 5 nm. Later in this thesis (chapter 6) we show that indeed surface conduction plays a large role in 50 nm high channels at a reservoir concentration of 100 μM, however, distinction between a 2 fold in-/decrease in concentration is still electrically measurable using wall integrated electrodes.

2.3.2 Liquid transport (pumping)

As discussed in the introduction, pumping of liquids in nanochannels is preferably performed by electrokinetics, amongst others because of its beneficial scaling behavior. This observation is reflected in the number of publications employing electrokinetic pumping in nanochannels that have appeared in recent years [7,9,11,17,20,25,28,60,70,72-76,84,110,112-125]. Whereas the above publications address flows with zero slip at the walls, Muller et al. [99] predicted that hydrodynamic slip will strongly enhance the magnitude of electro-osmotic flow in nanochannels, since the effect will scale with b/λ_D (with b the slip length and λ_D the Debye length) instead of with b/h as for pressure-driven flow (with h the channel height). This prediction was recently both theoretically and experimentally supported by Bocquet and coworkers, who found an increase of the electro-osmotic flow velocity at hydrophobic surfaces by a factor of two [98,100]. A much smaller amount of articles is published where pressure driven flow is employed [126-129] which, except for ref. [129] have an electrokinetic angle, because they consider power generation by generating streaming currents.

Several other driving forces are proposed in literature [130-134]. An example of a more exotic driving force is diffusio-osmosis [135-148]. Here, liquid transport is generated by a concentration difference between two ends of a channel or two sides of a particle. This concentration difference causes two types of transport named chemi-osmosis and electro-osmosis, caused by diffusion and migration of net charge, respectively. Transport in the latter case is caused by a difference in cationic and anionic flux, thereby inducing a potential gradient along the channel. This potential gradient in turn induces fluid motion in the channel equivalent to electro-osmosis except without the need of an externally applied potential difference. Flow speeds attained are in the order of $\mu m.s^{-1}$ which is probably the reason diffusio-osmosis has received less attention in literature than electro-osmosis. An interesting development in the field is the introduction of liquid slip to diffusio-osmotically driven pumps. Ajdari and Bocquet [101] theoretically proposed diffusio-osmosis as a viable pumping method in nanochannels, under the condition of a certain amount of liquid slip. In that case the diffusio-osmotic flow velocity would be amplified with a factor b/L_m, where L_m is a sub-nanometer molecular length scale. A 100-fold amplification of the diffusio-osmotic flow velocity would then be possible.

Eijkel et al. [130] communicate on their findings on liquid flow in 500 nm high all-polyimide channels induced by pervaporation or osmosis of the solution through the thin channel roof. Due to the use of a large pervaporation area, the measured flow rates are up to 70 $\mu m.s^{-1}$. The pervaporation of water induces fluid flow by the movement of water from high chemical potential in the channel to low chemical potential in the atmosphere as in trees, and the osmosis induces fluid flow by water movement from low salt concentration to high salt concentration. This technique is a typical example of

a technique that exploits the large surface to volume ratios in nanochannels, since pervaporation is a function of surface and the effect for equal pervaporation rates is more pronounced in small volumes.

Soare et al. [132] theoretically describe a system with active deformable walls to drive liquid through a nanochannel. And in an amazingly simple experiment by Huh et al. [149], PDMS nanochannels are deformed to pump liquid. Nanochannels in PDMS are created by applying mechanical stress to thickly oxidized PDMS layers. Cracks that are in this manner created have a controllable width and height of 688 and 58 nm, respectively and are triangular shaped. This shape in combination with the use of extra stiff PDMS probably helps this device from irreversibly sticking. Liquid pumping in these channels can be obtained by applying a relatively small pressure (22-42 kPa) to the PDMS. Here lower applied pressures can be used to control flow velocity and higher pressures to completely close the channels. This technique could have a comparable impact to nanofluidics as the systems of Quake et al. have to microfluidics [150], because of the relatively easy fabrication and potential for massive parallelization.

All other techniques exploit the dominance of surface tension and viscous forces over inertia in nanofluidic channels. For example Tas et al. [133] use capillary filling to induce liquid movement in small microchannels in a technique which could potentially be scaled to nanoconfined channels. Pumping is performed by first replacing water by gas by inducing a slight gas over-pressure and then gas by water by capillary pressure. A structural asymmetry in the system thereby provides directionality to the pumping.

Another more exotic way of exploiting surface tension and viscous forces is one where liquid flow is induced in a lipid nanotube between unilamellar vesicles [131]. This is done by continuously manipulating the shape of one of the vesicles by a micromanipulator and as such changing the surface tension causing a lipid flow in the nanotube from high to low surface tension which consequently drags the liquid in the nanotube along by viscous forces.

2.3.3 Control of molecular transport

In this subsection transport control of dissolved molecules in nanofluidic channels is discussed. With transport control we here mean active control over the transport of ionic or molecular species inside the liquid. In microchannels transport control is often (of course with the notable exception of separation techniques like chromatography and electrophoresis) concerned with flow control [151] where only the transport of the liquid is actively controlled and the ionic-molecular species inside it passively follow the flow lines. In nanochannels, however, active control of the transport properties of different ionic and/or molecular species becomes feasible. The reason for this is twofold. First, nanochannels have a size that is in the order of the EDL, making selective transport properties based on charge possible. Secondly, (bio)-molecules often have a size in the nanometer range, making selective transport properties and thus separation based on size a possibility. Both reasons boil down to the molecular filtering or sieving properties that nanochannels have, properties they share with membranes and filters [79]. Since in the next subsection separation is treated, in this subsection the discussion will be restricted to ways of controlling the transport properties inside nanochannels.

Flow control techniques in nanochannels are, just like the pumping techniques described above, dominated by electrokinetics [16,25,95,106,116,122,152-173]. Above the possibility of controlling the transport parameters of different ionic species inside the liquid inside a nanochannel was mentioned. Examples of experimental papers exploiting this possibility are [106,122,160,165]. Interesting to notice is that though all four articles have different ways of gaining control over the transport properties, all are based on electrostatics. Kuo et al. [122] and Schoch et al. [106] approach the problem mainly by altering the electrostatic potential by changing the chemical parameters pH and electrolyte strength. The main difference between the two is that Kuo et al. use a membrane and Schoch et al. a specifically engineered nanochannel. Karnik et al. [160] gain control by actively varying the electrostatic potential at the wall of a nanochannel by electrodes buried in the wall. This modifies the double layer charge, changing the electro-osmotic mobility and could eventually lead to flow inversion at high applied positive voltages (i.e. in case of a negatively charged wall). The effects are strongest at pH values close to the point of zero charge of the wall (around pH 2 for glass walls). The reason for this is that the chemical buffer capacity for protons of the walls is smallest in this region [174]. Finally, Miedema et al. [165] present the most direct way of transport control by altering the polarity of several surface groups inside a biological porin and therewith creating a nanofluidic diode (figure 4). A trend in nanofluidics in recent years is to manufacture the fluidic equivalent of well-known electrical circuit elements such as diodes [152,154,161,165] and transistors [95,157,158,160,164,171]. This preferably leads to large system integration on a single chip, as is known from electronic chips, which could for example be very beneficial for time and analyte consuming screening of new drugs [175]. Other examples of transport control by electrostatics are control by changing important chemical parameters such as pH and/or background concentration [106,122,167-169]. Finally Powell and coworkers present the controllable oscillating transport of ions through nanoscale pores by the transient formation and re-dissolution of nanoprecipitates [176].

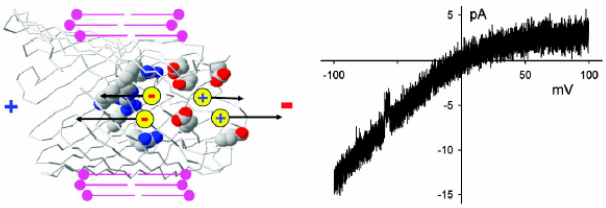

Figure 4: A biological poring engineered into a molecular, nanofluidic diode. Left: graphical interpretation of the system. Right: Typical I-V curve showing rectifying behavior. Reprinted from [165]

2.3.4 Energy conversion

Energy conversion from the liquid mechanical to the electrical domain is a topic of renewed increasing interest. Since the sixties when amongst others Osterle [177] and

Burgreen and Nakache [178] studied energy conversion in nanofluidic structures, the subject had not received a lot of attention. However, a technology sufficiently matured to fabricate with relative ease structures with nanometer dimensions and the probable advent of an energy crisis has fired researchers to rethink the problem mainly trying to solve the low efficiency [126-128,179-181] (which is currently around a few percent). Although the efficiency is low (i.e. especially compared to electromagnetic generation which can have an efficiency up to around 95 %), fluidic energy conversion would allow for massive parallelization on a relatively small surface area, therewith promising a high power density.

The increase of efficiency and the implementation of parallelization were recently theoretically discussed by Pennathur et al. [181] and by Ren and Stein [126]. The main conclusions of both papers is that in systems without slip the maximum achievable efficiency will be around 10 %, whilst with slip it can probably be around 30%. These effects could, however, practically be limited by the fact that systems that facilitate slip are often hydrophobic and are known to have a lower effective surface charge. According to Ren and Stein this could be solved by doping, surface modification or voltage biasing, which might in turn decrease the surface hydrophobicity and therewith the amount of slip. Here experiment will have to decide. Prospects however seem promising in view of the fact that slip-enhanced electro-osmotic flow has recently been experimentally observed, and the realization that the streaming potential is simply the experimental inverse of the electro-osmotic flow.

In terms of parallelization this technique holds great potential. Ren and Stein calculate that if nanotubes are to be applied, increasing the channel density to an effective nanotube area coverage of around 1 % could render $kW.m^{-2}$ power densities. Such massive parallelization could possibly be done by using highly oriented pyrolitic graphite. Although promising, the practicality of this system needs to be proven by experiment, since for one the efficiency of such a system might be smaller than expected because of the conductivity of highly oriented graphite which might facilitate current back flow and thereby diminishing the induced streaming current.

Further practical difficulties, which are not yet solved, arise when one wants to reliably electrically interface this system. This is up to now done by using Ag/AgCl reference electrodes which are known to have a rather limited lifetime especially when a large amount of current is passed through them. A more in depth analysis of nanofluidic transport on energy conversion can be found in [181].

2.3.5 Separation

Since it is not the main aim of this chapter to review separation in nanodevices, and this subject indeed would deserve a separate review, we will here treat it only briefly. Reviews of separation in nanoengineered devices have recently appeared [79,182], also providing some background theory. Phenomenologically, the same forces are encountered as in microscale systems namely hydrodynamic forces, electrostatic forces, van der Waals forces, solvation forces (like hydrogen bonding) and entropic forces. The use of micro- and nanotechnology now allows for better control of the separating structure, enabling improved separation performance or even entirely new separation methods.

Hydrodynamic forces are mainly employed in separation systems to transport the analytes from the injection point to the detection point, but a parabolic flow profile can also be used to perform hydrodynamic chromatography by the different average speed of large and small species in such a flow. Blom, Chmela et al. [183] showed hydrodynamic chromatography in channel of 1 μm height, separating beads of the order of 10 nm. Stein et al. [129] showed a size-dependent transport rate of DNA in nanochannels by pressure-driven transport of DNA, which they ascribed to a process similar to hydrodynamic chromatography. Ogston sieving (sieving only based on molecular size) can be regarded as a variant of hydrodynamic chromatography in a sieving matrix. The group of J. Han performs this type of sieving in a continuous flow fashion [184].
Electrostatic forces are employed in the direction of main transport (electrophoresis) but they will also always be present in the double layer, then acting perpendicular to the transport direction. In the latter case they alter the rate of passage of charged analytes through a sieve. Since the electro-osmotic flow profile in a nanochannel approaches a parabolic shape this modifies the transport rate of the counter-ions residing close to the wall with respect to co-ions residing in the middle of the channel. As a result the effective electrophoretic mobility is affected as was demonstrated by Pennathur et al. [73-76].

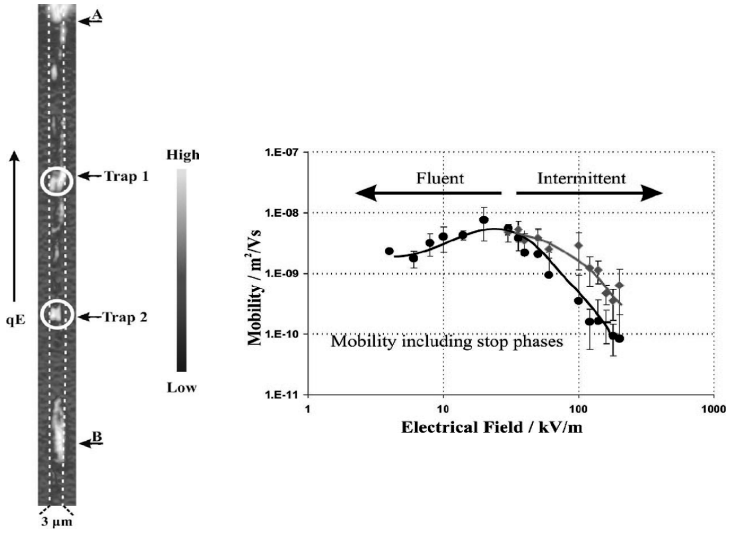

Figure 5: Electric field dependent movement of DNA in 20 nm high slit nanochannels. Left: transient trapping of DNA at higher electric fields. Right DNA mobility as a function of applied field, clearly indicating modified transport behavior at higher applied fields. Reprinted from [87].

Several groups have demonstrated electrophoretic separation of DNA in nanochannels [185]. Cross attributed the observed separation of 2-10kb long DNA molecules in 19 nm high nanoslits to a differential friction with the walls [186]. Pennathur et al. observed electrophoretic separation of DNA oligomers (10-100 bp) in

100 nm deep channels [187]. The observed dependence on ionic strength suggested an important role for the electrical double layer field. Salieb-Beugelaar, Teapal et al. observed a mobility of long DNA (48 and 2.8 kbp) in 20 nm nanoslits that depended on the DNA length and strongly on the applied field, with transient trapping observed at higher fields, figure 5 [87]. In view of the applied field strengths (up to 200 kV/m) dielectrophoresis and steric trapping were suggested as explanations.

In general the inevitable increase of entropy during a separation decreases the resolution obtained. In the case of the self-diffusion of the DNA molecule however, entropy can be used for separation. Nanofluidic confinement will take away entropic freedom from a DNA molecule, and as a result DNA tends to remain in a space where it can freely self-diffuse, or move to such a space if part of its chain already resides there. This 'entropic trapping' which is also known from large-pore gels [188] has been employed in nanofluidic devices for DNA separation both in batch-like and continuous formats [80,184] and was also employed in an entropic recoil device [189]. Time scales for separation however are long since diffusional steps are necessarily involved. A very eloquent view on separation by exploiting changes in entropy is written by Austin [190].

Leinweber et al. showed that entropy can also be counteracted electrochemically in a nanofluidic continuous flow de-mixing device [191]. On the application of an axial electrical field, de-mixing was observed at electrode islands embedded in the channel wall, separating ionic analytes in concentrated and diluted streams in the flow direction.

Liquid chromatography can strongly benefit from micromachining, which provides an entirely regular packing of the separation channel which considerably decreases peak broadening. The group of Desmet has strongly advanced in this area [192,193], which was started by the group of Regnier [194]. They employ micromachining to pack a separation channel with pillars of width and spacing in the order of 500 nm, and provide the necessary nanoporosity of the separation matrix by the use of porous silicon.

A drawback of nanofluidic separation systems is their low sample throughput, which gives rise to detection problems. This problem can be approached in several ways. Thus a continuous flow format can be adopted, which will improve the amount of separated analyte at the cost of the analysis time [80,182,184,195]. Also, the concentration polarization caused by a nanochannel can be employed to pre-concentrate analytes in a (perpendicular) microchannel [196]. In both cases the spatial architecture of the systems involved is only practically possible because of the use of micromachining methods, allowing 'smart design' that is non-random down to the 50 nm scale [197]. Another answer to the detection problem might be the use of parallel separation channels with parallel detection in each channel to avoid band broadening.

2.4 Conclusion and outlook

In conclusion, we have shown by reviewing both experimental and theoretical literature that liquid flow and electrokinetics in nanochannels concerning aqueous electrolytes can often be modeled using continuum theory (i.e. the Stokes and Nernst-Planck equations for the liquid flow and electrokinetic problems, respectively) for channels with a size down to 10 nm. Moreover we present several important consequences on transport of an increasing surface to volume ratio for decreasing channel height/diameter. We reviewed liquid slip, chemical equilibria between solution and wall molecules, adsorption of molecules to the channel walls and wall surface roughness.

Applications of transport in nanochannels range from pumping and transport control to energy conversion and separation. The main general conclusion that can be drawn is that all applications exploit the large surface to volume ratio in nanochannels. Because of this large surface to volume ratio, interactions of the solution and-or molecules inside it with the walls become increasingly important for decreasing channel dimensions, sometimes also causing problems like adsorption. Moreover, in contrast to transport in microfluidics, in nanofluidics (preferably with double layer overlap) transport control of individual charged molecules becomes feasible. Finally, liquid transport is always accompanied by a net charge displacement inducing potential and/or pressure gradients which have an increasing influence on transport properties for decreasing channel height.

Reviewing a decade in which many interesting novel devices empowered by the rapidly expanding field of nanofluidics have been presented, brings us to the conclusion that nanofluidics will most likely play a significant role in various application areas in years to come. We envision an important role of nanofluidics in the following fields:

- Analytical- and bio-chemistry: From single molecule detection towards spatial and temporal control of individual molecules inside aqueous solutions such as proteins and DNA molecules.
- Liquid transport and dosing: By exploring and exploiting liquid slip conditions to engineer precise and highly efficient transport and dosing systems.
- Energy conversion: Nanofluidics holds potential for high power density energy conversion at high efficiency if liquid slip is introduced.

Finally, with improved control of structures on the nanoscale made possible by nanotechnological developments, more phenomena and applications are anticipated.

References

1. Turner, S.W., A.M. Perez, A. Lopez, and H.G. Craighead, *Monolithic nanofluid sieving structures for DNA manipulation.* Journal of Vacuum Science & Technology B, 1998. **16**(6): p. 3835-3840.
2. Eijkel, J.C.T. and A. van den Berg, *Nanofluidics: what is it and what can we expect from it?* Microfluidics and Nanofluidics, 2005. **1**(3): p. 249-267.
3. Abgrall, P. and N.T. Nguyen, *Nanofluidic devices and their applications.* Analytical Chemistry, 2008. **80**(7): p. 2326-2341.
4. Mijatovic, D., J.C.T. Eijkel, and A. van den Berg, *Technologies for nanofluidic systems: top-down vs. bottom-up - a review.* Lab on a Chip, 2005. **5**(5): p. 492-500.
5. Perry, J.L. and S.G. Kandlikar, *Review of fabrication of nanochannels for single phase liquid flow.* Microfluidics and Nanofluidics, 2006. **2**(3): p. 185-193.
6. Schoch, R.B., J.Y. Han, and P. Renaud, *Transport phenomena in nanofluidics.* Reviews of Modern Physics, 2008. **80**(3): p. 839-883.
7. Yuan, Z., A.L. Garcia, G.P. Lopez, and D.N. Petsev, *Electrokinetic transport and separations in fluidic nanochannels.* Electrophoresis, 2007. **28**(4): p. 595-610.
8. Alder, B.J. and T.E. Wainwright, *Studies in Molecular Dynamics .1. General Method.* Journal of Chemical Physics, 1959. **31**(2): p. 459-466.
9. Duong-Hong, D., J.S. Wang, G.R. Liu, Y.Z. Chen, J. Han, and N.G. Hadjiconstantinou, *Dissipative particle dynamics simulations of electroosmotic flow in nano-fluidic devices.* Microfluidics and Nanofluidics, 2008. **4**(3): p. 219-225.
10. Gwan, J.F. and A. Baumgaertner, *Ion transport in a nanochannel.* Journal of Computational and Theoretical Nanoscience, 2007. **4**(1): p. 50-56.
11. Qiao, R. and N.R. Aluru, *Ion concentrations and velocity profiles in nanochannel electroosmotic flows.* Journal of Chemical Physics, 2003. **118**(10): p. 4692-4701.
12. Hanasaki, I. and A. Nakatani, *Microscopic structure of water flow through carbon nanotubes.* Advanced Structural and Functional Materials Design, Proceedings, 2006. **512**: p. 399-404.
13. Todd, B.D., *Cats, maps and nanoflows: some recent developments in nonequilibrium nanofluidics.* Molecular Simulation, 2005. **31**(6-7): p. 411-428.
14. Xu, D., D. Li, Y. Leng, and Y. Chen, *Molecular dynamics simulations of ion distribution in nanochannels.* Molecular Simulation, 2007. **33**(12): p. 959-963.
15. Raghunathan, A.V. and N.R. Aluru, *Self-consistent molecular dynamics formulation for electric-field-mediated electrolyte transport through nanochannels.* Physical Review E, 2007. **76**(1): p. -.
16. Chinappi, M., E. De Angelis, S. Melchionna, C.M. Casciola, S. Succi, and R. Piva, *Molecular dynamics simulation of ratchet motion in an asymmetric nanochannel.* Physical Review Letters, 2006. **97**(14): p. -.
17. Qiao, R., *Effects of molecular level surface roughness on electroosmotic flow.* Microfluidics and Nanofluidics, 2007. **3**(1): p. 33-38.

18. Qiao, Y., G.X. Cao, and X. Chen, *Effects of gas molecules on nanofluidic behaviors.* Journal of the American Chemical Society, 2007. **129**(8): p. 2355-2359.
19. Noy, A., H.G. Park, F. Fornasiero, J.K. Holt, C.P. Grigoropoulos, and O. Bakajin, *Nanofluidics in carbon nanotubes.* Nano Today, 2007. **2**(6): p. 22-29.
20. Kim, D. and E. Darve, *Molecular dynamics simulation of electro-osmotic flows in rough wall nanochannels.* Physical Review E, 2006. **73**(5): p. -.
21. Li, Z.G. and G. Drazer, *Fluid enhancement of particle transport in nanochannels.* Physics of Fluids, 2006. **18**(11): p. -.
22. Drazer, G., J. Koplik, A. Acrivos, and B. Khusid, *Adsorption phenomena in the transport of a colloidal particle through a nanochannel containing a partially wetting fluid.* Physical Review Letters, 2002. **89**(24): p. -.
23. Rauscher, M., S. Dietrich, and J. Koplik, *Shear flow pumping in open micro- and nanofluidic systems.* Physical Review Letters, 2007. **98**(22): p. -.
24. Gong, X.J., J.Y. Li, H.J. Lu, R.Z. Wan, J.C. Li, J. Hu, and H.P. Fang, *A charge-driven molecular water pump.* Nature Nanotechnology, 2007. **2**(11): p. 709-712.
25. Qiao, R. and N.R. Aluru, *Surface-charge-induced asymmetric electrokinetic transport in confined silicon nanochannels.* Applied Physics Letters, 2005. **86**(14): p. -.
26. Zeng, L., G.H. Zuo, X.J. Gong, H.J. Lu, C.L. Wang, K.F. Wu, and R.Z. Wan, *Water and ion permeation through electrically charged nanopore.* Chinese Physics Letters, 2008. **25**(4): p. 1486-1489.
27. Bock, H., K.E. Gubbins, and M. Schoen, *Anisotropic self-diffusion in nanofluidic structures.* Journal of Physical Chemistry C, 2007. **111**(43): p. 15493-15504.
28. Qiao, R. and N.R. Aluru, *Atypical dependence of electroosmotic transport on surface charge in a single-wall carbon nanotube.* Nano Letters, 2003. **3**(8): p. 1013-1017.
29. Chakraborty, S., *Generalization of interfacial electrohydrodynamics in the presence of hydrophobic interactions in narrow fluidic confinements.* Physical Review Letters, 2008. **1**(9): p. -.
30. de Jong, J., R.G.H. Lammertink, and M. Wessling, *Membranes and microfluidics: a review.* Lab on a Chip, 2006. **6**(9): p. 1125-1139.
31. Woyke, A., *Reflections about an embedding of nanotechnology in a continuum of the history of science and technology.* Berichte Zur Wissenschaftsgeschichte, 2008. **31**(1): p. 58-67.
32. Succi, S., A.A. Mohammad, and J. Horbach, *Lattice-Boltzmann simulation of dense nanoflows: A comparison with Molecular Dynamics and Navier-Stokes solutions.* International Journal of Modern Physics C, 2007. **18**(4): p. 667-675.
33. Gad-el-Hak, M., *The fluid mechanics of microdevices - The Freeman Scholar Lecture.* Journal of Fluids Engineering-Transactions of the Asme, 1999. **121**(1): p. 5-33.
34. Probstein, R.F., *Physicochemical hydrodynamics : an introduction*. 2nd ed. 1994, New York: John Wiley & Sons. xv, 400 p.
35. Shui, L.L., J.C.T. Eijkel, and A. van den Berg, *Multiphase flow in micro- and nanochannels.* Sensors and Actuators B-Chemical, 2007. **121**(1): p. 263-276.

36. Eijkel, J., *Liquid slip in micro- and nanofluidics: recent research and its possible implications.* Lab on a Chip, 2007. **7**(3): p. 299-301.
37. Laser, D.J. and J.G. Santiago, *A review of micropumps.* Journal of Micromechanics and Microengineering, 2004. **14**(6): p. R35-R64.
38. Loose, W. and S. Hess, *Rheology of Dense Model Fluids Via Nonequilibrium Molecular-Dynamics - Shear Thinning and Ordering Transition.* Rheologica Acta, 1989. **28**(2): p. 91-101.
39. Lennard-Jones, J.E., Transactions of the Faraday Society, 1929. **25**.
40. Abascal, J.L.F., E. Sanz, R.G. Fernandez, and C. Vega, *A potential model for the study of ices and amorphous water: TIP4P/Ice.* Journal of Chemical Physics, 2005. **122**(23): p. -.
41. Abascal, J.L.F. and C. Vega, *A general purpose model for the condensed phases of water: TIP4P/2005.* Journal of Chemical Physics, 2005. **123**(23): p. -.
42. Berendsen, H.J.C., J.R. Grigera, and T.P. Straatsma, *The Missing Term in Effective Pair Potentials.* Journal of Physical Chemistry, 1987. **91**(24): p. 6269-6271.
43. Cho, C.H., M. Chung, J. Lee, T. Nguyen, S. Singh, M. Vedamuthu, S.H. Yao, J.B. Zhu, and G.W. Robinson, *Time-Resolved and Space-Resolved Studies of the Physics and Chemistry of Liquid Water near a Biologically Relevant Interface.* Journal of Physical Chemistry, 1995. **99**(19): p. 7806-7812.
44. Grigera, J.R., *An effective pair potential for heavy water.* Journal of Chemical Physics, 2001. **114**(18): p. 8064-8067.
45. Horn, H.W., W.C. Swope, J.W. Pitera, J.D. Madura, T.J. Dick, G.L. Hura, and T. Head-Gordon, *Development of an improved four-site water model for biomolecular simulations: TIP4P-Ew.* Journal of Chemical Physics, 2004. **120**(20): p. 9665-9678.
46. Lamoureux, G., E. Harder, I.V. Vorobyov, B. Roux, and A.D. MacKerell, *A polarizable model of water for molecular dynamics simulations of biomolecules.* Chemical Physics Letters, 2006. **418**(1-3): p. 245-249.
47. Mahoney, M.W. and W.L. Jorgensen, *A five-site model for liquid water and the reproduction of the density anomaly by rigid, nonpolarizable potential functions.* Journal of Chemical Physics, 2000. **112**(20): p. 8910-8922.
48. Paricaud, P., M. Predota, A.A. Chialvo, and P.T. Cummings, *From dimer to condensed phases at extreme conditions: Accurate predictions of the properties of water by a Gaussian charge polarizable model.* Journal of Chemical Physics, 2005. **122**(24): p. -.
49. Rick, S.W., *Simulations of ice and liquid water over a range of temperatures using the fluctuating charge model.* Journal of Chemical Physics, 2001. **114**(5): p. 2276-2283.
50. Rick, S.W., *A reoptimization of the five-site water potential (TIP5P) for use with Ewald sums.* Journal of Chemical Physics, 2004. **120**(13): p. 6085-6093.
51. Stern, H.A., F. Rittner, B.J. Berne, and R.A. Friesner, *Combined fluctuating charge and polarizable dipole models: Application to a five-site water potential function.* Journal of Chemical Physics, 2001. **115**(5): p. 2237-2251.
52. Stilling.Fh and A. Rahman, *Improved Simulation of Liquid Water by Molecular-Dynamics.* Journal of Chemical Physics, 1974. **60**(4): p. 1545-1557.

53. Tan, M.L., J.T. Fischer, A. Chandra, B.R. Brooks, and T. Ichiye, *A temperature of maximum density in soft sticky dipole water.* Chemical Physics Letters, 2003. **376**(5-6): p. 646-652.
54. Wu, Y.J., H.L. Tepper, and G.A. Voth, *Flexible simple point-charge water model with improved liquid-state properties.* Journal of Chemical Physics, 2006. **124**(2): p. -.
55. Yu, H.B. and W.F. van Gunsteren, *Charge-on-spring polarizable water models revisited: From water clusters to liquid water to ice.* Journal of Chemical Physics, 2004. **121**(19): p. 9549-9564.
56. Lide, D.R., ed., *CRC Handbook of Chemistry and Physics, Internet version, http://www.hbcpnetbase.com*. CRC Press, Boca, Fl., 2005.
57. Fox, R.W. and A.T. McDonald, *Introduction to fluid mechanics*. 3rd ed. 1985, New York: Wiley. x, 741 p.
58. White, F.M., *Fluid mechanics*. 3rd ed. Schaum's outline series in mechanical engineering. 1994, New York: McGraw-Hill. xiii, 736 p.
59. Constantinescu, V.N., *Laminar viscous flow*. 1995, New York: Springer. xv, 488 p.
60. Freund, J.B., *Electro-osmosis in a nanometer-scale channel studied by atomistic simulation.* Journal of Chemical Physics, 2002. **116**(5): p. 2194-2200.
61. Hunter, R.J., *Zeta potential in colloid science : principles and applications*. 1981, London: Academic Press. xi, 386 p.
62. Lyklema, J., S. Rovillard, and J. De Coninck, *Electrokinetics: The properties of the stagnant layer unraveled.* Langmuir, 1998. **14**(20): p. 5659-5663.
63. Zhang, J.F., B.D. Todd, and K.P. Travis, *Viscosity of confined inhomogeneous nonequilibrium fluids.* Journal of Chemical Physics, 2004. **121**(21): p. 10778-10786.
64. Israelachvili, J.N. and R.M. Pashley, *Molecular Layering of Water at Surfaces and Origin of Repulsive Hydration Forces.* Nature, 1983. **306**(5940): p. 249-250.
65. Pashley, R.M. and J.N. Israelachvili, *Molecular Layering of Water in Thin-Films between Mica Surfaces and Its Relation to Hydration Forces.* Journal of Colloid and Interface Science, 1984. **101**(2): p. 511-523.
66. vanHal, R.E.G., J.C.T. Eijkel, and P. Bergveld, *A general model to describe the electrostatic potential at electrolyte oxide interfaces.* Advances in Colloid and Interface Science, 1996. **69**: p. 31-62.
67. Yates, D.E., S. Levine, and T.W. Healy, *Site-Binding Model of Electrical Double-Layer at Oxide-Water Interface.* Journal of the Chemical Society-Faraday Transactions I, 1974. **70**: p. 1807-1818.
68. van der Heyden, F.H.J., D. Stein, and C. Dekker, *Streaming currents in a single nanofluidic channel.* Physical Review Letters, 2005. **95**(11): p. -.
69. Plecis, A., R.B. Schoch, and P. Renaud, *Ionic transport phenomena in nanofluidics: Experimental and theoretical study of the exclusion-enrichment effect on a chip.* Nano Letters, 2005. **5**(6): p. 1147-1155.
70. Burgreen, D. and F.R. Nakache, *Electrokinetic Flow in Ultrafine Capillary Slits.* Journal of Physical Chemistry, 1964. **68**(5): p. 1084-&.

71. Conlisk, A.T., *The Debye-Huckel approximation: Its use in describing electroosmotic flow in micro- and nanochannels.* Electrophoresis, 2005. **26**(10): p. 1896-1912.
72. Levine, S., J.R. Marriott, and K. Robinson, *Theory of Electrokinetic Flow in a Narrow Parallel-Plate Channel.* Journal of the Chemical Society-Faraday Transactions Ii, 1975. **71**(1): p. 1-11.
73. Pennathur, S. and J.G. Santiago, *Electrokinetic transport in nanochannels. 1. Theory.* Analytical Chemistry, 2005. **77**(21): p. 6772-6781.
74. Pennathur, S. and J.G. Santiago, *Electrokinetic transport in nanochannels. 2. Experiments.* Analytical Chemistry, 2005. **77**(21): p. 6782-6789.
75. Pennathur, S. and J.G. Santiago, *Electrokinetic transport in nanochannels. 1. Theory (vol 77, pg 6772, 2005).* Analytical Chemistry, 2006. **78**(3): p. 972-972.
76. Pennathur, S. and J.G. Santiago, *Electrokinetic transport in nanochannels. 2. Experiments (vol 77, pg 6782, 2005).* Analytical Chemistry, 2006. **78**(3): p. 972-972.
77. Pu, Q.S., J.S. Yun, H. Temkin, and S.R. Liu, *Ion-enrichment and ion-depletion effect of nanochannel structures.* Nano Letters, 2004. **4**(6): p. 1099-1103.
78. Stein, D., M. Kruithof, and C. Dekker, *Surface-charge-governed ion transport in nanofluidic channels.* Physical Review Letters, 2004. **93**(3): p. -.
79. Eijkel, J.C.T. and A. van den Berg, *Nanotechnology for membranes, filters and sieves.* Lab on a Chip, 2006. **6**(1): p. 19-23.
80. Han, J. and H.G. Craighead, *Separation of long DNA molecules in a microfabricated entropic trap array.* Science, 2000. **288**(5468): p. 1026-1029.
81. Bard, A.J. and L.R. Faulkner, *Electrochemical methods : fundamentals and applications*. 2nd ed. 2001, New York: John Wiley. xxi, 833 p.
82. Kilic, M.S., M.Z. Bazant, and A. Ajdari, *Steric effects in the dynamics of electrolytes at large applied voltages. I. Double-layer charging.* Physical Review E, 2007. **75**(2): p. -.
83. Kilic, M.S., M.Z. Bazant, and A. Ajdari, *Steric effects in the dynamics of electrolytes at large applied voltages. II. Modified Poisson-Nernst-Planck equations.* Physical Review E, 2007. **75**(2): p. -.
84. Qiao, R. and N.R. Aluru, *Scaling of electrokinetic transport in nanometer channels.* Langmuir, 2005. **21**(19): p. 8972-8977.
85. Balducci, A., P. Mao, J.Y. Han, and P.S. Doyle, *Double-stranded DNA diffusion in slitlike nanochannels.* Macromolecules, 2006. **39**(18): p. 6273-6281.
86. Ajdari, A. and J. Prost, *Free-Flow Electrophoresis with Trapping by a Transverse Inhomogeneous Field.* Proceedings of the National Academy of Sciences of the United States of America, 1991. **88**(10): p. 4468-4471.
87. Salieb-Beugelaar, G.B., J. Teapal, J. van Nieuwkasteele, D. Wijnperle, J.O. Tegenfeldt, F. Lisdat, A. van den Berg, and J.C.T. Eijkel, *Field-dependent DNA mobility in 20 nm high nanoslits.* Nano Letters, 2008. **8**(7): p. 1785-1790.
88. Vinogradova, O.I., *Slippage of water over hydrophobic surfaces.* International Journal of Mineral Processing, 1999. **56**(1-4): p. 31-60.
89. Kievsky, Y.Y., B. Carey, S. Naik, N. Mangan, D. Ben-Avraham, and I. Sokolov, *Dynamics of molecular diffusion of rhodamine 6G in silica nanochannels.* Journal of Chemical Physics, 2008. **128**(15): p. -.

90. Durand, N.F.Y., A. Bertsch, M. Todorova, and P. Renaud, *Direct measurement of effective diffusion coefficients in nanochannels using steady-state dispersion effects.* Applied Physics Letters, 2007. **91**(20): p. -.
91. Karnik, R., K. Castelino, C.H. Duan, and A. Majumdar, *Diffusion-limited patterning of molecules in nanofluidic channels.* Nano Letters, 2006. **6**(8): p. 1735-1740.
92. Yamaguchi, A., M.M. Mekawy, Y. Chen, S. Suzuki, K. Morita, and N. Teramae, *Diffusion of metal complexes inside of silica-surfactant nanochannels within a porous alumina membrane.* Journal of Physical Chemistry B, 2008. **112**(7): p. 2024-2030.
93. Yamaguchi, A., T. Yoda, S. Suzuki, K. Morita, and N. Teramae, *Diffusivities of tris(2,2 '-bipyridyl)ruthenium inside silica-nanochannels modified with alkylsilanes.* Analytical Sciences, 2006. **22**(12): p. 1501-1507.
94. Cottin-Bizonne, C., C. Barentin, E. Charlaix, L. Bocquet, and J.L. Barrat, *Dynamics of simple liquids at heterogeneous surfaces: Molecular-dynamics simulations and hydrodynamic description.* European Physical Journal E, 2004. **15**(4): p. 427-438.
95. Karnik, R., R. Fan, M. Yue, D.Y. Li, P.D. Yang, and A. Majumdar, *Electrostatic control of ions and molecules in nanofluidic transistors.* Nano Letters, 2005. **5**(5): p. 943-948.
96. Janssen, K.G.H., H.T. Hoang, J. Floris, d.J. Vries, N.R. Tas, J.C.T. Eijkel, and T. Hankemeier, *Solution Titration by Wall Deprotonation During Capillary Filling of Silicon Oxide Nanochannels.* Analytical Chemistry, 2008. Accepted for publication.
97. Whitby, M. and N. Quirke, *Fluid flow in carbon nanotubes and nanopipes.* Nature Nanotechnology, 2007. **2**(2): p. 87-94.
98. Joly, L., C. Ybert, E. Trizac, and L. Bocquet, *Liquid friction on charged surfaces: From hydrodynamic slippage to electrokinetics.* Journal of Chemical Physics, 2006. **125**(20): p. -.
99. Muller, V.M., I.P. Sergeeva, V.D. Sobolev, and N.V. Churaev, *Boundary effects in the theory of electrokinetic phenomena.* Kolloidnyi Zhurnal, 1986. **48**(4): p. 718-727.
100. Bouzigues, C.I., P. Tabeling, and L. Bocquet, Physical Review Letters, 2008. **101**.
101. Ajdari, A. and L. Bocquet, *Giant amplification of interfacially driven transport by hydrodynamic slip: Diffusio-osmosis and beyond.* Physical Review Letters, 2006. **96**(18): p. -.
102. Navier, C.L.M.H., *Memoire sur les lois du mouvement des fluides.* Mem. Acad. Sci. Inst. France, 1823. **6**: p. 389-440.
103. Lauga, E., B. M.P., and H.A. Stone, *The no-slip boundary condition.* Springer Handbook of Experimental Fluid Mechanics, 2007. Part C(Chapter 19).
104. Cottin-Bizonne, C., B. Cross, A. Steinberger, and E. Charlaix, *Boundary slip on smooth hydrophobic surfaces: Intrinsic effects and possible artifacts.* Physical Review Letters, 2005. **94**(5): p. -.
105. Poppe, H., *Some reflections on speed and efficiency of modern chromatographic methods.* Journal of Chromatography A, 1997. **778**(1-2): p. 3-21.

106. Schoch, R.B., A. Bertsch, and P. Renaud, *pH-Controlled diffusion of proteins with different pl values across a nanochannel on a chip.* Nano Letters, 2006. **6**(3): p. 543-547.
107. Delamarche, E., A. Bernard, H. Schmid, B. Michel, and H. Biebuyck, *Patterned delivery of immunoglobulins to surfaces using microfluidic networks.* Science, 1997. **276**(5313): p. 779-781.
108. Sinton, D., *Microscale flow visualization.* Microfluidics and Nanofluidics, 2004. **1**(1): p. 2-21.
109. Zettner, C.M. and M. Yoda, *Particle velocity field measurements in a near-wall flow using evanescent wave illumination.* Experiments in Fluids, 2003. **34**(1): p. 115-121.
110. Mela, P., N.R. Tas, E.J.W. Berenschot, J. van Nieuwkasteele, and A. van den Berg, *Electrokinetic pumping and detection of low-volume flows in nanochannels.* Electrophoresis, 2004. **25**(21-22): p. 3687-3693.
111. Huang, X.H., M.J. Gordon, and R.N. Zare, *Current-Monitoring Method for Measuring the Electroosmotic Flow-Rate in Capillary Zone Electrophoresis.* Analytical Chemistry, 1988. **60**(17): p. 1837-1838.
112. Bhattacharyya, S., Z. Zheng, and A.T. Conlisk, *Electro-osmotic flow in two-dimensional charged micro- and nanochannels.* Journal of Fluid Mechanics, 2005. **540**: p. 247-267.
113. Bhattacharyya, S. and A.K. Nayak, *Electro-osmotic transport in charged cylindrical micro- and nano-channels.* International Journal of Engineering Science, 2007. **45**(1): p. 55-74.
114. Wang, M., J. Liu, and S. Chen, *Similarity of electroosmotic flows in nanochannels.* Molecular Simulation, 2007. **33**(3): p. 239-244.
115. Xuan, X.C. and D.Q. Li, *Electrokinetic transport of charged solutes in micro- and nanochannels: The influence of transverse electromigration.* Electrophoresis, 2006. **27**(24): p. 5020-5031.
116. Wang, S.N.A., X. Hua, and L.J. Lee, *Electrokinetics induced asymmetric transport in polymeric nanonozzles.* Lab on a Chip, 2008. **8**(4): p. 573-581.
117. Huang, K.D. and R.J. Yang, *Electrokinetic behaviour of overlapped electric double layers in nanofluidic channels.* Nanotechnology, 2007. **18**(11): p. -.
118. Dutta, D., *Electroosmotic transport through rectangular channels with small zeta potentials.* Journal of Colloid and Interface Science, 2007. **315**(2): p. 740-746.
119. Miao, J.Y., Z.L. Xu, X.Y. Zhang, N. Wang, Z.Y. Yang, and P. Sheng, *Micropumps based on the enhanced electroosmotic effect of aluminum oxide membranes.* Advanced Materials, 2007. **19**(23): p. 4234-+.
120. Chakraborty, S. and A.K. Srivastava, *Generalized model for time periodic electroosmotic flows with overlapping electrical double layers.* Langmuir, 2007. **23**(24): p. 12421-12428.
121. Jin, X.Z., S. Joseph, E.N. Gatimu, P.W. Bohn, and N.R. Aluru, *Induced electrokinetic transport in micro-nanofluidic interconnect devices.* Langmuir, 2007. **23**(26): p. 13209-13222.
122. Kuo, T.C., L.A. Sloan, J.V. Sweedler, and P.W. Bohn, *Manipulating molecular transport through nanoporous membranes by control of electrokinetic flow:*

Effect of surface charge density and debye length. Langmuir, 2001. **17**(20): p. 6298-6303.
123. Chakraborty, S. and S. Padhy, *Induced pressure gradients due to entrance and exit effects in electroosmotically driven flows through nanopores within the continuum regime.* Journal of Physics D-Applied Physics, 2008. **41**(6): p. -.
124. Chen, L. and A.T. Conlisk, *Electroosmotic flow and particle transport in micro/nano nozzles and diffusers.* Biomedical Microdevices, 2008. **10**(2): p. 289-298.
125. Rice, C.L. and Whitehea.R, *Electrokinetic Flow in a Narrow Cylindrical Capillary.* Journal of Physical Chemistry, 1965. **69**(11): p. 4017-&.
126. Ren, Y.Q. and D. Stein, *Slip-enhanced electrokinetic energy conversion in nanofluidic channels.* Nanotechnology, 2008. **19**(19): p. -.
127. van der Heyden, F.H.J., D.J. Bonthuis, D. Stein, C. Meyer, and C. Dekker, *Power generation by pressure-driven transport of ions in nanofluidic channels.* Nano Letters, 2007. **7**(4): p. 1022-1025.
128. Daiguji, H., P.D. Yang, A.J. Szeri, and A. Majumdar, *Electrochemomechanical energy conversion in nanofluidic channels.* Nano Letters, 2004. **4**(12): p. 2315-2321.
129. Stein, D., F.H.J. van der Heyden, W.J.A. Koopmans, and C. Dekker, *Pressure-driven transport of confined DNA polymers in fluidic channels.* Proceedings of the National Academy of Sciences of the United States of America, 2006. **103**(43): p. 15853-15858.
130. Eijkel, J.C.T., J.G. Bomer, and A. van den Berg, *Osmosis and pervaporation in polyimide submicron microfluidic channel structures.* Applied Physics Letters, 2005. **87**(11): p. -.
131. Karlsson, R., M. Karlsson, A. Karlsson, A.S. Cans, J. Bergenholtz, B. Akerman, A.G. Ewing, M. Voinova, and O. Orwar, *Moving-wall-driven flows in nanofluidic systems.* Langmuir, 2002. **18**(11): p. 4186-4190.
132. Soare, M.A., R.C. Picu, J. Tichy, T.M. Lu, and G.C. Wang, *Fluid transport through nanochannels using nanoelectromechanical actuators.* Journal of Intelligent Material Systems and Structures, 2006. **17**(3): p. 231-238.
133. Tas, N.R., J.W. Berenschot, T.S.J. Lammerink, M. Elwenspoek, and A. van den Berg, *Nanofluidic bubble pump using surface tension directed gas injection.* Analytical Chemistry, 2002. **74**(9): p. 2224-2227.
134. Prieve, D.C., J.L. Anderson, J.P. Ebel, and M.E. Lowell, *Motion of a Particle Generated by Chemical Gradients .2. Electrolytes.* Journal of Fluid Mechanics, 1984. **148**(Nov): p. 247-269.
135. Anderson, J.L., D.C. Prieve, and J.P. Ebel, *Chemically-Induced Migration of Particles across Fluid Streamlines.* Chemical Engineering Communications, 1987. **55**(1-6): p. 211-224.
136. Keh, H.J. and L.Y. Hsu, *Diffusioosmosis of electrolyte solutions in fibrous porous media.* Microfluidics and Nanofluidics, 2008. **5**(3): p. 347-356.
137. Keh, H.J. and H.C. Ma, *Diffusioosmosis of electrolyte solutions in fine capillaries.* Colloids and Surfaces a-Physicochemical and Engineering Aspects, 2004. **233**(1-3): p. 87-95.
138. Keh, H.J. and H.C. Ma, *Diffusioosmosis of electrolyte solutions along a charged plane wall.* Langmuir, 2005. **21**(12): p. 5461-5467.

139. Keh, H.J. and H.C. Ma, *Diffusioosmosis of electrolyte solutions in a fine capillary tube.* Langmuir, 2007. **23**(5): p. 2879-2886.
140. Keh, H.J. and H.C. Ma, *The effect of diffusioosmosis on water transport in polymer electrolyte fuel cells.* Journal of Power Sources, 2008. **180**(2): p. 711-718.
141. Keh, H.J. and Y.K. Wei, *Osmosis through a fibrous medium caused by transverse electrolyte concentration gradients.* Langmuir, 2002. **18**(26): p. 10475-10485.
142. Keh, H.J. and Y.K. Wei, *Diffusioosmosis and electroosmosis of electrolyte solutions in fibrous porous media.* Journal of Colloid and Interface Science, 2002. **252**(2): p. 354-364.
143. Ma, H.C. and H.J. Keh, *Diffusioosmosis of electrolyte solutions in a capillary slit with surface charge layers.* Colloids and Surfaces a-Physicochemical and Engineering Aspects, 2005. **267**(1-3): p. 4-15.
144. Ma, H.C. and H.J. Keh, *Diffusioosmosis of electrolyte solutions in a fine capillary slit.* Journal of Colloid and Interface Science, 2006. **298**(1): p. 476-486.
145. Ma, H.C. and H.J. Keh, *Diffusioosmosis of electrolyte solutions in a capillary slit with adsorbed polyelectrolyte layers.* Journal of Colloid and Interface Science, 2007. **313**(2): p. 686-696.
146. Qian, S.Z., B. Das, and X.B. Luo, *Diffusioosmotic flows in slit nanochannels.* Journal of Colloid and Interface Science, 2007. **315**(2): p. 721-730.
147. Wei, Y.K. and H.J. Keh, *Diffusioosmosis of nonelectrolyte solutions in a fibrous medium.* Colloids and Surfaces a-Physicochemical and Engineering Aspects, 2003. **221**(1-3): p. 175-183.
148. Wu, J.H. and H.J. Keh, *Diffusioosmosis and electroosmosis in a capillary slit with surface charge layers.* Colloids and Surfaces a-Physicochemical and Engineering Aspects, 2003. **212**(1): p. 27-42.
149. Huh, D., K.L. Mills, X.Y. Zhu, M.A. Burns, M.D. Thouless, and S. Takayama, *Tuneable elastomeric nanochannels for nanofluidic manipulation.* Nature Materials, 2007. **6**(6): p. 424-428.
150. Quake, S.R. and A. Scherer, *From micro- to nanofabrication with soft materials.* Science, 2000. **290**(5496): p. 1536-1540.
151. Schasfoort, R.B.M., S. Schlautmann, L. Hendrikse, and A. van den Berg, *Field-effect flow control for microfabricated fluidic networks.* Science, 1999. **286**(5441): p. 942-945.
152. Alcaraz, A., P. Ramirez, E. Garcia-Gimenez, M.L. Lopez, A. Andrio, and V.M. Aguilella, *A pH-tunable nanofluidic diode: Electrochemical rectification in a reconstituted single ion channel.* Journal of Physical Chemistry B, 2006. **110**(42): p. 21205-21209.
153. Cervera, J., A. Alcaraz, B. Schiedt, R. Neumann, and P. Ramirez, *Asymmetric selectivity of synthetic conical nanopores probed by reversal potential measurements.* Journal of Physical Chemistry C, 2007. **111**(33): p. 12265-12273.
154. Cheng, L.J. and L.J. Guo, *Rectified ion transport through concentration gradient in homogeneous silica nanochannels.* Nano Letters, 2007. **7**(10): p. 3165-3171.

155. Constantin, D. and Z.S. Siwy, *Poisson-Nernst -Planck model of ion current rectification through a nanofluidic diode.* Physical Review E, 2007. **76**(4): p. -.
156. Daiguji, H., Y. Oka, and K. Shirono, *Nanofluidic diode and bipolar transistor.* Nano Letters, 2005. **5**(11): p. 2274-2280.
157. Fan, R., S. Huh, R. Yan, J. Arnold, and P.D. Yang, *Gated proton transport in aligned mesoporous silica films.* Nature Materials, 2008. **7**(4): p. 303-307.
158. Fan, R., M. Yue, R. Karnik, A. Majumdar, and P.D. Yang, *Polarity switching and transient responses in single nanotube nanofluidic transistors.* Physical Review Letters, 2005. **95**(8): p. -.
159. Gracheva, M.E., J. Vidal, and J.P. Leburton, *p-n semiconductor membrane for electrically tunable ion current rectification and filtering.* Nano Letters, 2007. **7**(6): p. 1717-1722.
160. Karnik, R., K. Castelino, and A. Majumdar, *Field-effect control of protein transport in a nanofluidic transistor circuit.* Applied Physics Letters, 2006. **88**(12): p. -.
161. Karnik, R., C.H. Duan, K. Castelino, H. Daiguji, and A. Majumdar, *Rectification of ionic current in a nanofluidic diode.* Nano Letters, 2007. **7**(3): p. 547-551.
162. Kosinska, I.D., *How the asymmetry of internal potential influences the shape of I-V characteristic of nanochannels.* Journal of Chemical Physics, 2006. **124**(24): p. -.
163. Kosinska, I.D. and A. Fulinski, *Asymmetries and anomalous phenomena in ionic transport through nanochannels.* Acta Physica Polonica B, 2007. **38**(5): p. 1631-1645.
164. Kuo, T.C., D.M. Cannon, Y.N. Chen, J.J. Tulock, M.A. Shannon, J.V. Sweedler, and P.W. Bohn, *Gateable nanofluidic interconnects for multilayered microfluidic separation systems.* Analytical Chemistry, 2003. **75**(8): p. 1861-1867.
165. Miedema, H., M. Vrouenraets, J. Wierenga, W. Meijberg, G. Robillard, and B. Eisenberg, *A biological porin engineered into a molecular, nanofluidic diode.* Nano Letters, 2007. **7**(9): p. 2886-2891.
166. Ramirez, P., V. Gomez, J. Cervera, B. Schiedt, and S. Mafe, *Ion transport and selectivity in nanopores with spatially inhomogeneous fixed charge distributions.* Journal of Chemical Physics, 2007. **126**(19): p. -.
167. Schoch, R.B. and P. Renaud, *Ion transport through nanoslits dominated by the effective surface charge.* Applied Physics Letters, 2005. **86**(25): p. -.
168. Schoch, R.B., H. van Lintel, and P. Renaud, *Effect of the surface charge on ion transport through nanoslits.* Physics of Fluids, 2005. **17**(10): p. -.
169. van der Heyden, F.H.J., D. Stein, K. Besteman, S.G. Lemay, and C. Dekker, *Charge inversion at high ionic strength studied by streaming currents.* Physical Review Letters, 2006. **96**(22): p. -.
170. Vidal, J., M.E. Gracheva, and J.P. Leburton, *Electrically tunable solid-state silicon nanopore ion filter.* Nanoscale Research Letters, 2007. **2**(2): p. 61-68.
171. Vlassiouk, I. and Z.S. Siwy, *Nanofluidic diode.* Nano Letters, 2007. **7**(3): p. 552-556.
172. Wang, X.W., J.M. Xue, L. Wang, W. Guo, W.M. Zhang, Y.G. Wang, Q. Liu, H. Ji, and Q.Y. Ouyang, *How the geometric configuration and the surface*

charge distribution influence the ionic current rectification in nanopores. Journal of Physics D-Applied Physics, 2007. **40**(22): p. 7077-7084.
173. White, H.S. and A. Bund, *Ion current rectification at nanopores in glass membranes.* Langmuir, 2008. **24**(5): p. 2212-2218.
174. van der Wouden, E.J., D.C. Hermes, J.G.E. Gardeniers, and A. van den Berg, *Directional flow induced by synchronized longitudinal and zeta-potential controlling AC-electrical fields.* Lab on a Chip, 2006. **6**(10): p. 1300-1305.
175. Gijs, M.A.M., *Device physics - Will fluidic electronics take off?* Nature Nanotechnology, 2007. **2**(5): p. 268-270.
176. Powell, M.R., M. Sullivan, I. Vlassiouk, D. Constantin, O. Sudre, C.C. Martens, R.S. Eisenberg, and Z.S. Siwy, *Nanoprecipitation-assisted ion current oscillations.* Nature Nanotechnology, 2008. **3**(1): p. 51-57.
177. Osterle, J.F., *Unified Treatment of Thermodynamics of Steady-State Energy Conversion.* Applied Scientific Research Section a-Mechanics Heat Chemical Engineering Mathematical Methods, 1964. **12**(6): p. 425-&.
178. Burgreen, D. and F.R. Nakache, *Efficiency of Pumping and Power Generation in Ultrafine Electrokinetic Systems.* Journal of Applied Mechanics, 1965. **32**(3): p. 675-&.
179. Davidson, C. and X.C. Xuan, *Electrokinetic energy conversion in slip nanochannels.* Journal of Power Sources, 2008. **179**(1): p. 297-300.
180. Davidson, C. and X.C. Xuan, *Effects of Stern layer conductance on electrokinetic energy conversion in nanofluidic channels.* Electrophoresis, 2008. **29**(5): p. 1125-1130.
181. Pennathur, S., J.C.T. Eijkel, and A. van den Berg, *Energy conversion in microsystems: is there a role for micro/nanofluidics?* Lab on a Chip, 2007. **7**(10): p. 1234-1237.
182. Han, J.Y., J.P. Fu, and R.B. Schoch, *Molecular sieving using nanofilters: Past, present and future.* Lab on a Chip, 2008. **8**(1): p. 23-33.
183. Blom, M.T., E. Chmela, R.E. Oosterbroek, R. Tijssen, and A. van den Berg, *On-chip hydrodynamic chromatography separation and detection of nanoparticles and biomolecules.* Analytical Chemistry, 2003. **75**(24): p. 6761-6768.
184. Fu, J.P., R.B. Schoch, A.L. Stevens, S.R. Tannenbaum, and J.Y. Han, *A patterned anisotropic nanofluidic sieving structure for continuous-flow separation of DNA and proteins.* Nature Nanotechnology, 2007. **2**(2): p. 121-128.
185. Tegenfeldt, J.O., C. Prinz, H. Cao, R.L. Huang, R.H. Austin, S.Y. Chou, E.C. Cox, and J.C. Sturm, *Micro- and nanofluidics for DNA analysis.* Analytical and Bioanalytical Chemistry, 2004. **378**(7): p. 1678-1692.
186. Cross, J.D., E.A. Strychalski, and H.G. Craighead, *Size-dependent DNA mobility in nanochannels.* Journal of Applied Physics, 2007. **102**(2): p. -.
187. Pennathur, S., F. Baldessari, J.G. Santiago, M.G. Kattah, J.B. Steinman, and P.J. Utz, *Free-solution oligonucleotide separation in nanoscale channels.* Analytical Chemistry, 2007. **79**(21): p. 8316-8322.
188. Viovy, J.L., *Electrophoresis of DNA and other polyelectrolytes: Physical mechanisms.* Reviews of Modern Physics, 2000. **72**(3): p. 813-872.

189. Turner, S.W.P., M. Cabodi, and H.G. Craighead, *Confinement-induced entropic recoil of single DNA molecules in a nanofluidic structure.* Physical Review Letters, 2002. **88**(12): p. -.
190. Austin, R., *Nanofluidics - A fork in the nano-road.* Nature Nanotechnology, 2007. **2**(2): p. 79-80.
191. Leinweber, F.C., J.C.T. Eijkel, J.G. Bower, and A. van den Berg, *Continuous flow microfluidic demixing of electrolytes by induced charge electrokinetics in structured electrode arrays.* Analytical Chemistry, 2006. **78**(5): p. 1425-1434.
192. De Malsche, W., H. Eghbali, D. Clicq, J. Vangelooven, H. Gardeniers, and G. Desmet, *Pressure-driven reverse-phase liquid chromatography separations in ordered nonporous pillar array columns.* Analytical Chemistry, 2007. **79**(15): p. 5915-5926.
193. De Malsche, W., H. Gardeniers, and G. Desmet, *Experimental study of porous silicon shell pillars under retentive conditions.* Analytical Chemistry, 2008. **80**(14): p. 5391-5400.
194. He, B., J.Y. Ji, and F.E. Regnier, *Capillary electrochromatography of peptides in a microfabricated system.* Journal of Chromatography A, 1999. **853**(1-2): p. 257-262.
195. Han, A.P., N.F. de Rooij, and U. Staufer, *Design and fabrication of nanofluidic devices by surface micromachining.* Nanotechnology, 2006. **17**(10): p. 2498-2503.
196. Wang, Y.C., A.L. Stevens, and J.Y. Han, *Million-fold preconcentration of proteins and peptides by nanofluidic filter.* Analytical Chemistry, 2005. **77**(14): p. 4293-4299.
197. Eijkel, J.C.T., *Scaling revisited.* Lab on a Chip, 2007. **7**(12): p. 1630-1632.

Chapter 3

Design and Fabrication of Traveling Wave Driven Pumps in Nanochannels

In this chapter the design and fabrication of traveling wave driven pumps in nanochannels is presented. Both the design and the fabrication also apply to the technologically more simple pumps which are actuated by AC voltage driven asymmetric electrode arrays. Design choices based on technological, physical and time-management considerations are discussed thoroughly. All fabrication steps are explained and described using relevant cross sections of the device during subsequent fabrication steps. Furthermore, the resulting device is tested both electrically and optically. The results of these tests show that the device behaves within the window of the demands given at the start of this chapter. Optical tests show an 18% and a 30% difference in lateral dimensions of the nanochannels and the electrodes, respectively, as compared to the designed masks. This was caused by an under-etch of the photo-resist layer and is, therefore, most pronounced for narrow structures.

3.1 Introduction

The difference in design and fabrication of nanochannels with integrated electrodes as compared to microchannels is not trivial. Scaling down well below 1 µm means that every irregularity on or parallel to the electrodes with the same order of magnitude as the channel height potentially causes leakage problems. Therefore, we had to develop a new method to create nanochannels with integrated bare metal electrodes. An important part of this new method, namely, the etching of a sacrificial layer is discussed in more detail in chapter 4 [1]. Actuating such a device with traveling waves poses stringent demands on the electrical behavior of the device. Moreover, the nanochannels need to be fluidically interfaced which is done by microchannels. A schematical overview of the device including key-parts of the experimental setup is given in figure 1 and 2.

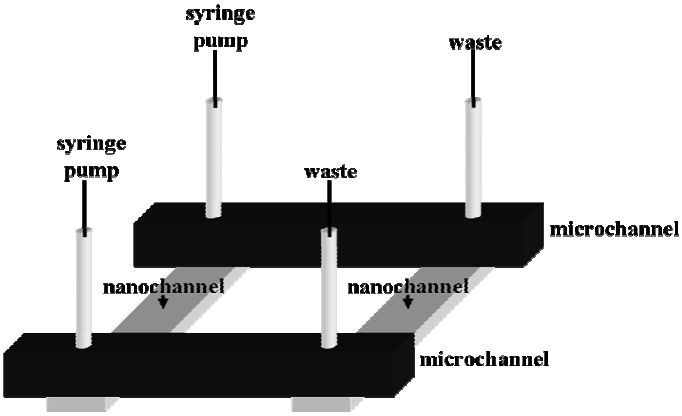

Figure 1: Schematical overview of the fluidic part of the device illustrating its connection to the experimental setup.

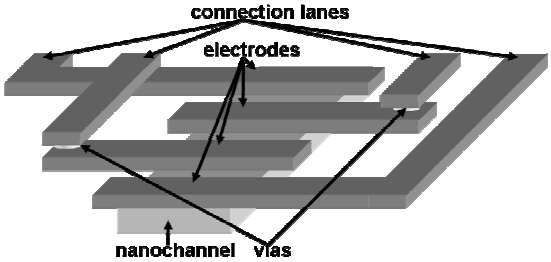

Figure 2: Schematical overview of the electrical part of the device illustrating its connection to the fluidic part.

Next to the obvious difference in channel height between our device and traveling wave or AC voltage driven asymmetric electrode array devices described in literature there is a difference in fabrication method. In microfluidic devices with integrated bare metal electrodes described in literature [2,3] bulk micromachining is the method of choice. For microfluidic devices this is possible, because their channel height is at least one order of magnitude higher than their electrode thickness and, therefore, does not cause considerable leakage problems. Since in our case the channel height is in the same order of magnitude as the electrode height, surface micromaching appears to be a better choice. In section 3.3 our choice for surface micromachining is further elucidated.

Manufacturing a traveling wave driven pump in nanochannels generates a list of demands on the fabrication process. Technological possibilities and electrical behavior further confines this list by posing constraints on the design. Both demands and constraints are presented in section 3.2. This results in a system which is systematically described in section 3.3. Subsequently, the fabrication process is described in section 3.4. Finally, the feasibility of the proposed design and manufacturing method is assessed by performing optical and electrical measurements on finished devices in section 3.5. All design and fabrication steps treated in this chapter also apply to the AC voltage driven asymmetric electrode array devices. They, however, lack a secondary connection layer, since they are connected with only two connections instead of four in the traveling wave case.

3.2 Demands and constraints

In this section the demands and constraints on all subsystems of the device are given. Some of them derive from a (chemical-) physical point of view, while others are more of a technological nature. All demands and constraints are treated in 3.2.1. The lists are divided into subsystems, namely, nanochannels, electrodes and insulation/capping layer and microchannels. The most important observations are placed in two tables and are used to assess several technique and/or material choices on their applicability. These tables are presented in subsection 3.2.2, which is used in combination with the other demands and constraints to design the final system in the next section (3.3).

3.2.1 Demands and constraints

In this subsection four lists of demands and constraints are given. Besides physical and technological constraints, also some constraints based on time management are listed. These constraints, mostly, set up demands to use well-known and well-described techniques, with which we preferably have in-home experience.

Nanochannels

- Channel height
    - In the order of the double layer thickness at 100 μM salt strength

  - As high or higher than minimal thickness of sputtered chromium / minimal depth of trench etching
- Channel width
  - At least approximately 500 nm for optical detection
  - At most 5 µm for mechanical stability
- Channel length
  - Not shorter than ~4 mm for fluidic connectivity
  - Not longer than ~4 mm to limit fluidic resistance and in case of surface micromachining etch times
- Material choice
  - Known and well described in literature
  - Known surface chemistry
  - Cleanroom compatible
- Fabrication method
  - Based on standard lithography
  - Consisting of known and well-described techniques
  - Reproducible
- Mechanical strength
  - Ability to withstand capillary filling
- Substrate
  - Optically transparent
  - Electrically insulating
- Two nanochannels on a chip to have a backup in case of fouling (more than two would with respect to fouling be better, however, practically it is hard to connect more than two nanochannels electrically)

Electrodes and insulation layers

Electrodes
- Noble metal
- No oxide layer
- Highly conductive
- Compatible with cleanroom technologies
- Mechanically stable/ Adhesion to the substrate
- Width and separation as small as possible with conventional lithography
- Compatible with surface micromachining:
  - Positively tapered on top (to provide good step coverage for subsequent layers)
  - Good step coverage on the previous layer to seal off the channel (i.e. step coverage will be discussed in more detail in section 3.3.1)
- Resistant to potential differences up to several Volts
  - No dissolution in common electrolytic solutions
  - No delamination from the substrate/capping layer
- Resistant to the chemicals used (e.g. often used salts/etchant)

Insulation layer

- Connections in two layers with minimized crosstalk between layers (i.e. resistance and capacitance as low as possible)
- Breakdown voltage higher than 10 V
- Resistant to the chemicals used (e.g. often used salts/etchant)

Microchannels
- Ability to be placed on top of the nanochannel and electrode structure without creating leakage
- Simple and well-known process parameters
- Easy to interface
- Able to span at least 1 cm between two neighboring nanochannels

Able to flush through at least 10 times the total volume of the nanochannel per second (i.e. ~1 pL/s) driven by a standard syringe pump, in order to make sure the solution composition is a constant factor in the experiments without creating too large pressure drops (<0.2 Bar which is equivalent to a linear velocity in the nanochannel of 1 $\mu m.s^{-1}$ in a 50 nm high, 5 μm wide and 4 mm long nanochannel).

3.2.2 Selection tables

In this subsection tables to assess the important choices for the application of methods and materials are presented. In table 1 the advantages and disadvantages of two main fabrication methods for the nanochannels are given. Table 2 shows important considerations concerning the material choice of the microchannels. Both tables will be used in section 3.3 to come to the final system design.

Table 1: Selection table for the fabrication method of the nanochannels and the electrodes

List of important parameters	*Bulk machining*	Surface machining
Well-described in literature	++ [3-7]	++ [8-12]
In house experience	++	+
Integratability with bare metal electrodes	- *	++
Integratability with microchannels	++	+/-
Observability of the channel with an inverted microscope	++	++
Mechanical stability	++	+/- **
Fluidic connectivity	++	+/- ***

* Fluidic leakage will probably occur, as described in detail in the next section (3.3)
** Errors in the fabrication process could lead to collapsing roofs
*** Channels might collapse if mechanical pressure is applied for the fluidic connections

Table 2: Selection table for the material choice of the microchannels

List of important parameters	*PDMS*	*Glass/Nitride*
Well-known	++	++
In house experience	++	++
Integratability with the nanochannels (in case of surface machining)	++	++
Integratability with the nanochannels (in case of bulk machining)	++	-*
Low auto-fluorescence	+/-	++
Mechanical stability	-	+
Fluidic connectivity	+/-	++

* CMP is necessary to planarize the surface. Anodic and fusion bonding are tricky, because they both could destroy the electrodes.

3.3 System description

Whereas in the previous section the design parameters were reviewed, in this section the system which we eventually chose will be described.

3.3.1 Nanochannels

In literature different ways of nanochannel fabrication can be found. Reviews on nanochannel fabrication methods can be found in [13-15]. In section 3.2.2 bulk machining and surface machining are assessed on their applicability to fabricate nanochannels with integrated electrodes. If microchannels with integrated bare electrodes are fabricated, often bulk micromachining chosen [2-3], however, upon down scaling beyond 100 nm, surface irregularities on the channel surface become important and possibly have the same order of magnitude as the channels themselves. In figure 3 a schematical cross section of a nanochannel, with integrated electrodes, fabricated by conventional bulk micromachining is given.

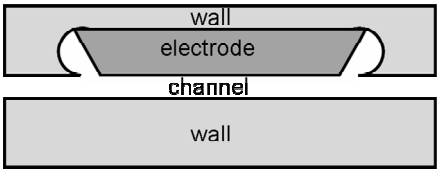

Figure 3: Schematical cross-section of a nanochannel with integrated electrodes fabricated by bulk-micromachining. This figure illustrates leakage problems around the electrodes.

Figure 3 clearly shows the leakage problems that occur when such a device is operated. These problems could probably be overcome by chemical-mechanical polishing (CMP) prior to bonding in combination with sputtering under an angle and rotating the sample. However, CMP is known to be time-consuming and hard to control, hence, we chose not to use bulk micromachining for the fabrication of the device. In surface micromachining all process steps are done subsequently on a single wafer. This means that as long as one is able to have a good step coverage of subsequent layers, surface micro-machining could potentially render leak-free channels including electrodes with minimal effort. With step coverage the coverage of subsequent layers on steps on previously deposited layers is meant (see figure 4 for typical examples of layers which are suited and unsuited for obtaining good step coverage).

As described in chapter 4 we chose to use a sacrificial chromium layer to define the channel geometry and dimensions. The reason for this is that it is easy to sputter, it adheres well to a Pyrex surface and its etching process is well described in literature, amongst others, because of its use in mask fabrication. Furthermore, chromium is low in the electrochemical series making it an interesting candidate for galvanically

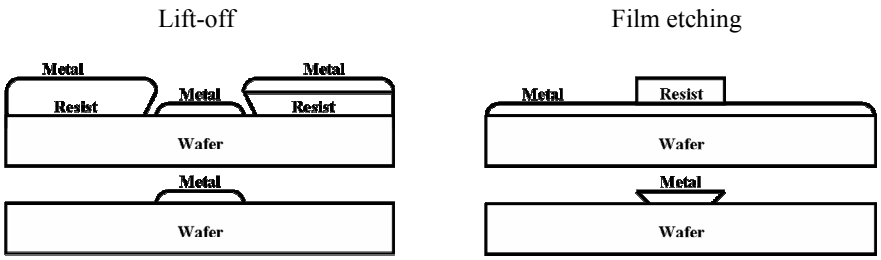

Figure 4: Schematical cross-sections of a typical lift-off process on the left and a film-etch process on the right. This figure illustrates possible step-coverage problems with standard metal film etching.

enhanced etching as is described in chapter 4. As mentioned above, step coverage is important in surface micro-machining. In figure 4 the differences between lift-off and film-etching are shown. This figure illustrates why lift-off enables good step coverage and thin film etching does not. Hence, we chose lift-off as our preferred fabrication method.

For lift-off the development time of the resist layer is of foremost importance. If the resist is developed too short the walls of the resist are positively tapered. This causes deposition of metal on these walls which in turn causes so-called lift-off ears. If the development time is too long, the holes defined in the resist become too big. This causes deposition of metal on unwanted locations. This leads to over sized structures and could also lead to lift-off feet, because the metal deposition at these unwanted positions is often much thinner than on the wanted positions. Both lift-off ears and feet are illustrated graphically in figure 5. From figure 5 problems with step coverage can easily be understood. Since lift-off is also applied to deposit the sacrificial layer, lift-off ears could, in this layer, potentially lead to a mechanically instable roof.

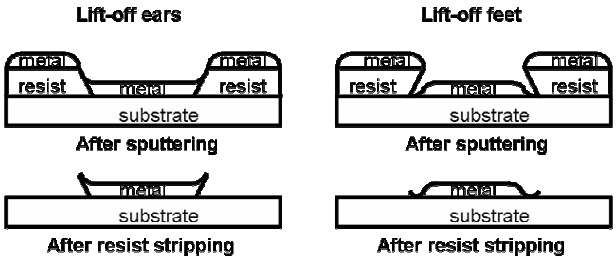

Figure 5: Schematical cross-sections of a metal film with lift-off ears and feet caused by too short and too long development, respectively.

3.3.2 Electrodes

The material choice of the electrode is dictated by at least two considerations. First, it should be cleanroom compatible. Second, it should be a noble metal to keep it electrochemically stable upon application of potential differences in electrolytic solutions. This brings us to two metals, namely, gold and platinum. To choose between them, three other considerations can be made. They are based on possible formation of surface oxide, electronegativity and mechanical stability and in all three aspects gold will prove to be the metal of preference. Platinum is known to slightly oxidize in aqueous solutions [16] and gold is not. Gold, furthermore, has a slightly higher electronegativity as compared to platinum, making it a more interesting candidate for galvanically enhanced etching. And finally, another important factor in the material choice is a mechanical one. For mechanical stability intrinsic stresses are important. Preferably we have tensile stress in our channel roof, because it then stretches the roof across the channel. Because our roof consists of both a capping layer and electrodes in order to prevent delamination it is important that their mechanical properties match. As a roof material we chose silicon nitride because it generally shows intrinsic tensile stress. We chose PECVD as our deposition method for it is a low temperature process (300 °C) and, therefore, causes minimal stresses on the electrodes (because of a possible mismatch in thermal expansion coefficient between the electrode and the capping material). PECVD silicon nitride is known to have hard-to-predict intrinsic stresses and is, therefore, an uncertain factor in the design. Both gold and platinum have a higher thermal expansion coefficient than silicon nitride [17], causing tensile stresses on the roof at room temperature. Because the electrodes and the capping layer form a bilayer at some locations in the chip the difference in thermal expansion coefficients would then cause upward bending of the roof. To prevent the electrodes and capping layer from delaminating, this difference in thermal expansion coefficients should be kept to a minimum. Although platinum has a lower expansion coefficient than gold (8.8 $\mu m.m^{-1}K^{-1}$ for platinum versus 14.2 $\mu m.m^{-1}K^{-1}$ for gold), gold has a much lower Young's modulus making it more resistant to stresses (168 GPa for platinum versus 78 GPa for gold). The stress between the electrodes and the capping layer is a linear function of both the thermal expansion coefficient and the Young's

modulus. If we calculate the ratio of the thermal expansion coefficients and the Young's moduli between both materials (which is shown in equation 1), the ratio of the Young's moduli is 1.3 times larger. This makes gold slightly more favorable also from a mechanical point of view.

$$r_Y = \frac{Y_{Pt}}{Y_{Au}} > \frac{\alpha_{Au}}{\alpha_{Pt}} = r_\alpha \tag{1}$$

The fabrication method will again be lift-off for the same reasons as mentioned above. The downside of the use of gold is that it does not adhere to Pyrex without an adhesion layer. Therefore, an adhesion layer needs to be employed. Often used adhesion layers are chromium and titanium. To prevent under-etching of the adhesion layer during sacrificial layer etching of the channel we choose titanium as the preferred adhesion material. To make sure most of the electrode surface in contact with the solution is gold positions of the electrode which are in contact with the channel only have a titanium layer on top. Everywhere else on the chip titanium is sputtered below and on top of the gold. More details are provided in section 3.4.

3.3.3 Microchannels

The most important consideration here is that the manufacturing technique for the microchannels should be compatible with the surface micro-machined nanochannel and electrode network. See section 3.1 for an overview of all device parts. One method would be to also use sacrificial layer etching for the fabrication of the microchannels. However, while theoretically possible, practically this is inconvenient, because the length of interconnecting microchannels is in de order of cm's, which even with galvanic coupling will lead to excessive etching times (2 weeks for a 2 cm long channel). This leads us to the choice for bulk micromachining. As is described in 3.2.2 we consider either glass or PDMS as the material for creating the microchannels. To bond a second glass wafer to the surface micro-machined nanochannels is hard for several reasons. Firstly, the chip is not resistant to temperatures beyond 300 ˚C because of the different thermal expansion coefficients of the materials (as is described in more detail in the previous subsection (3.3.2). Secondly, anodic bonding is very tricky because it will likely cause breakdown of the insulation layers and thereby destroy the electrode connections. And, thirdly, the chip surface is not flat so prior to bonding CMP is necessary, which is as described in 3.3.1 unfavorable. Considering all of this, we chose PDMS (polydimetylsiloxane). One advantage is that bonding is performed at room temperature. Moreover, the PDMS is flexible, so it conforms to an irregular surface. Some downsides are a low bond strength (resistant up to fluidic pressure differences around 4 Bar), slight auto-fluorescence and, moreover, in practice difficult to interface when using a chip-holder that comprises built-in fluidic connectors. The low bond strength is something we have to work around. The auto-fluorescence can be solved by not placing PDMS above the middle of the nanochannel where optical detection will take place. The interfacing was solved by abandoning the fluidic connectors and replacing them by home made PDMS connectors as is described in [18].

3.4 Fabrication

3.4.1 Pyrex based surface micro-machining of nanochannels with integrated gold electrodes

In this subsection the fabrication of the nanochannels with integrated electrodes is described. The description is complemented by schematical cross sections and top views of the device for several important process steps.

In the following all important fabrication steps are illustrated via cross sections through the device at three important locations. The positions of the cross sections are shown above each process scheme.

The first series of cross sections shows the fabrication steps at the location of the fluidic and electrical connections to the outside world. All metal layers are patterned by lift-off. For lift-off we used a LOR® A5 resist in combination with a standard photo resist (907/17). This sandwich combination of resists proved to be necessary, because single step lift-off resists did not give a reliable negative tapering (see section 3.3.1 for more detailed information on the necessity of a negative tapering).

The second series of cross sections shows the fabrication steps at the location between two electrodes. In this series the first two steps are the same as in the first series and are, therefore, not depicted. These cross sections clearly show that the nanochannel between electrodes is capped by a PECVD silicon nitride layer.

The third and last series of cross sections shows the fabrication steps at the location of an electrode that is connected to the second connection layer through a via. Also in this series the first two steps are not depicted for reasons stated in the previous paragraph. In these cross sections it can be observed that the nanochannel at the location of an electrode is capped by the electrode. Another important feature to notice is that although the electrode is in the same layer as its first connection it is not sputtered in the same fabrication step. The reason for this is twofold. Firstly, no adhesion layer below the electrode in the nanochannel area is used. This is done to create a defined interface (i.e. from an electrochemical point of view) between the electrode and the liquid in the nanochannel. Secondly, to prevent delamination of the gold from the Pyrex surface during PECV deposition of the first silicon nitride layer, we found out that gold layers without an adhesion layer underneath them needed to be kept as short as possible, so the connections outside the nanochannel area are sputtered with an adhesion layer. Furthermore, this series shows the creation of vias by ion beam etching positively tapered through holes and subsequent gold sputtering.

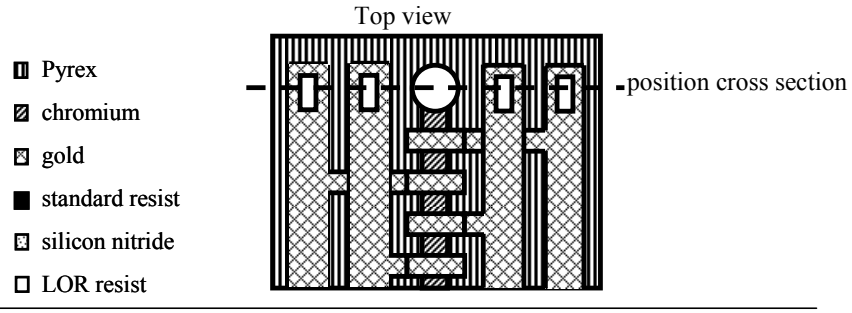

Cross sections during fabrication

1) Patterning and sputtering of a 50 nm high chromium sacrificial layer

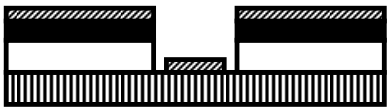

2) Lift-off

3) Patterning and sputtering of 180 nm gold connections sandwiched by two 15 nm titanium adhesion layers

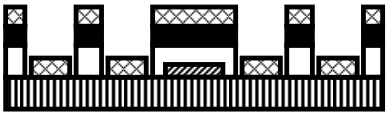

4) Lift-off

5) Deposition of two 400 nm PECVD silicon nitride capping/isolation layers

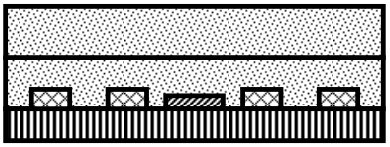

6) Patterning a mask layer for the subsequent ion beam etch

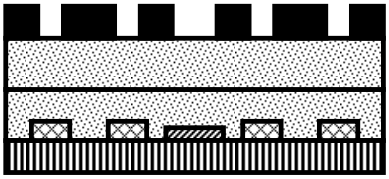

7) Ion beam etch and resist stripping

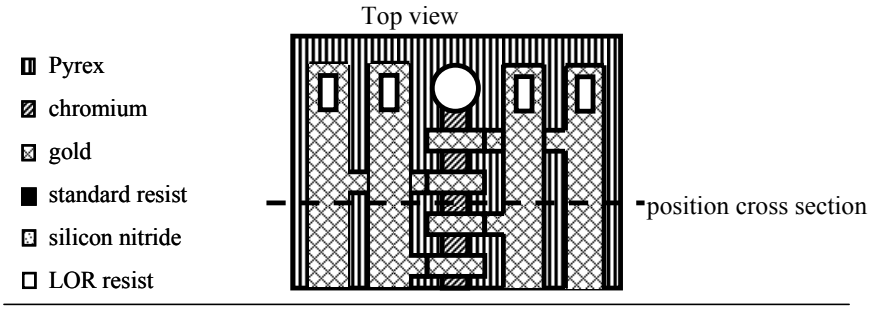

Cross sections during fabrication

1) Patterning and sputtering of 180 nm gold connections sandwiched by two 15 nm titanium adhesion layers

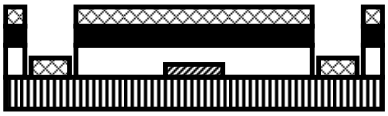

2) Lift-off

3) Deposition of a 400 nm PECVD silicon nitride capping/isolation layer

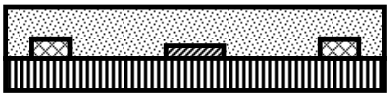

4) Patterning and sputtering of 180 nm gold connections sandwiched by two titanium adhesion layers

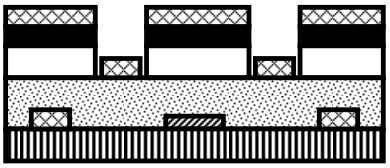

5) Lift-off

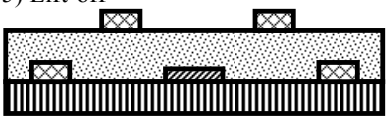

6) Deposition of a secondary 400 nm PECVD silicon nitride layer

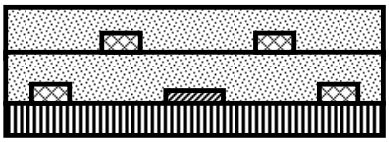

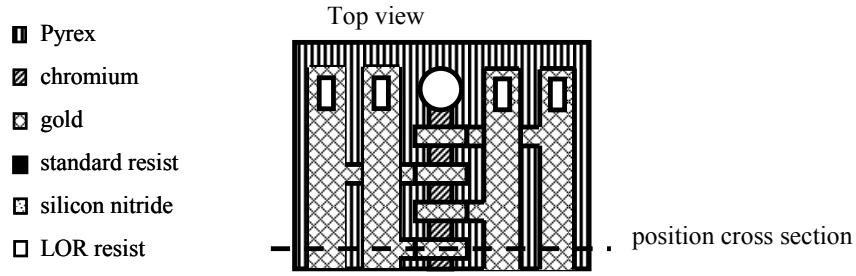

Cross sections during fabrication

1) Patterning and sputtering of 180 nm gold electrodes with a 15 nm titanium adhesion layer on top

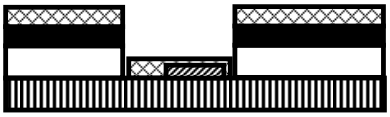

2) Lift-off

3) Patterning and sputtering of 180 nm gold connections sandwiched by two 15 nm titanium adhesion layers

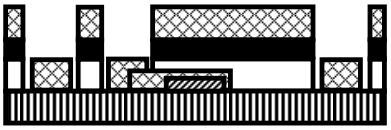

4) Lift-off

5) Deposition of a 400 nm PECVD silicon nitride capping/isolation layer

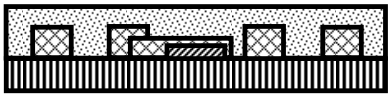

6) Patterning a resist layer to create vias

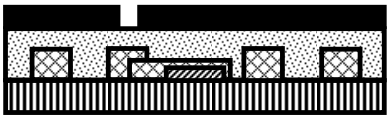

7) Ion beam etch to enable vias

8) Patterning and sputtering of 180 nm gold connections sandwiched by two 15 nm titanium layers

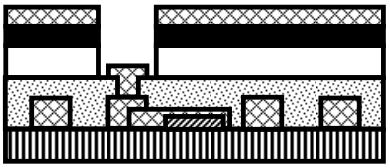

9) Lift-off

10) Deposition of a secondary 400 nm PECVD silicon nitride capping/isolation layer

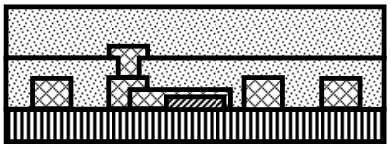

3.4.2 PDMS based molding of microchannels

In this subsection the fabrication steps of the microchannel network are given. Instead of using a silicon mold, we chose to use a PDMS mold. The advantage of this is that a polymer mold is much less vulnerable than a brittle silicon mold. A disadvantage is that with a polymer mold the channels are less well defined than with a silicon one. This is, however, not really important in this case, because we only use the microchannels as a transport medium for the solutions and are not interested in precise flow control in these channels. To prevent the PDMS from flooding of the mold during casting, degassing and hard baking we use scotch tape as a barrier. The final step is puncturing holes for the fluidic connections. We use a special puncturing tool for this that punctures 1 mm diameter holes. All important fabrication steps are given in schematical cross sections below.

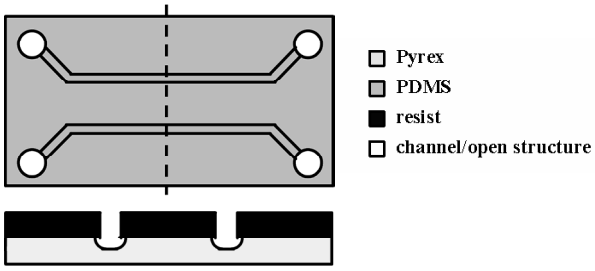

Patterning and BHF etching of 20 x 20 μm (width x height) trenches in Pyrex

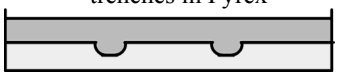

After spin-coating an anti-sticking coating (Teflon, 3M) 30 ml 10:1 (base:curing agent) PDMS is casted

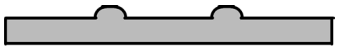

After degassing and subsequent hard bake (2 h @ 60 ˚C) the polymer mask is peeled of the Pyrex master

After spin-coating an anti-sticking coating (Teflon, 3M) 8 ml 10:1 (base:curing agent) PDMS is casted

After degassing and subsequent hard bake (1.5 h @ 60 ˚C) the microchannel network is peeled from the polymer mask

Later on it was found that the bonding of the in this way fabricated microchannel structure was often not reliable enough to last an entire experiment. Therefore, in chapter 6 an alternative fabrication method is presented.

3.4.3 System integration

In this subsection the integration of the nanochannels with the microchannels is shown. Below a list of steps for bonding and schematical top view of both parts (figure 6 and 7 for the part containing the nanochannels and the part containing the microchannels, respectively) and the resultant (figure 8) are given.

1. The Pyrex based chip is placed in slowly stirred acetone for 15 minutes
2. The PDMS based chip is placed in an ultrasonic bath containing acetone
3. Both chips are placed in a slowly stirred DI solution for 15 minutes
4. Both chips are rinsed twice with isopropanol
5. Both chips are dried for 5 minutes in an oven at 60 ˚C
6. Both chips are placed in an air plasma for 4 minutes
7. A droplet of methanol is dispensed on top of the Pyrex chips to enable aligning by preventing immediate bonding
8. The PDMS based chip is aligned on the Pyrex chip using a stereo microscope
9. The methanol is evaporated in an oven at 60 ˚C
10. The integrated chip is submersed in chromium etchant for 12 hours to etch away the sacrificial chromium layer (for more information on the etch process see chapter 4)

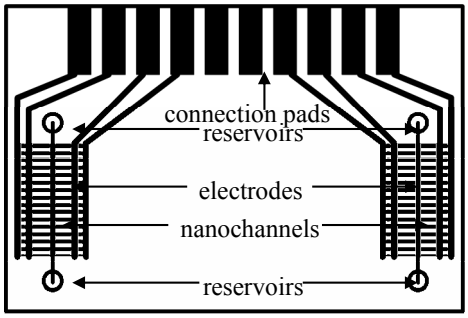

Figure 6: Schematical top view of the Pyrex based chip that contains the nanochannels, electrodes and all electrical connections.

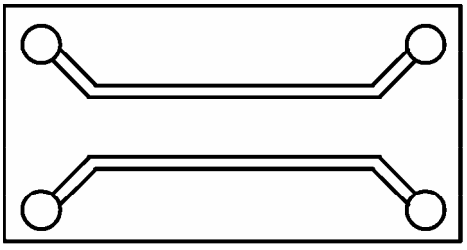

Figure 7: Schematical top view of the PDMS based chip that contains the microchannels and the fluidic through holes.

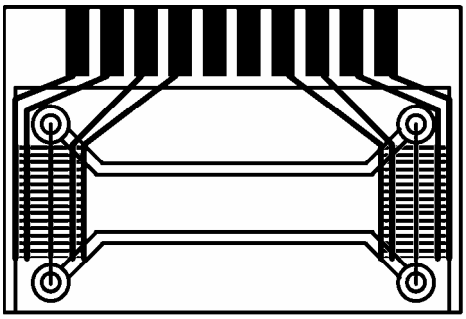

Figure 8: Schematical top view of the integration of the Pyrex and PDMS based chip.

3.5 Design and realization

In this section the design and fabrication process described in the previous sections is assessed both electrically and optically.

Below a table is given showing the most important electrical parameters of the fabricated device. Most of them are measured values, however, where measuring proved to be impossible literature values are used. All values were measured using a PARSTAT 2263 at test structures unless stated otherwise. The test structures were on the same wafer as the final devices and, therefore, represent certain aspects of the device behavior as well as possible. They consisted of multiple lanes (crossing or parallel) of sputtered gold of equal thickness as the device structures but with different widths and lengths and on top of different substrates (i.e. 2^{nd} layer structures are sputtered directly on Pyrex, whereas 3^{rd} layer structures are sputtered on top of the first PECVD silicon nitride layer). Cell constants used to translate resistances and capacitances to conductivities and dielectric constants, respectively, are calculated as follows. For wide and close (distance << width) crossing structures a parallel plate configuration is used, ignoring stray fields. For neighboring structures (distance ~ width) the model presented by Olthuis et.al. [19] is used.

Table 3: Electrical device properties measured using PARSTAT 2263

	Gold	*PECVD Silicon Nitride*
conductivity [S/m] 1st layer	/	5.17e-9 +/-31%
conductivity [S/m] 2nd layer	1.98e7 +/-7%	/
conductivity [S/m] 3rd layer	1.28e7 +/-8%	/
conductivity [S/m] vias	1.55e4 +/-50%	/
conductivity [S/m] bulk	4.52e7*	/
dielectric constant [-]	/	7.5*
breakdown voltage [mV/nm]	/	585 +/-25%**

* Literature value [17]

** The breakdown voltage was determined using a Keithley 2400 Sourcemeter ® for both positive and negative DC voltages. However, no significant difference (i.e. difference was within the measured error) was found between them.

Table 3 shows that planar deposited gold has a conductivity in the same order of magnitude as the literature value for the bulk conductivity. Furthermore, it shows that the conductivity the second layer is ~50% higher than that of the third layer. Dektak measurements of both layers show that their thickness is approximately equal. A possible explanation could be the fact that the second layer is sputtered directly on the Pyrex surface, whereas, the third layer is sputtered on the PECV deposited silicon nitride layer which might be slightly irregular causing a less uniform gold layer. Another remarkable result is the low conductivity of the vias. We characterized a via electrically by a 200 nm thick circular ring with a diameter of 6 μm and a length of 200 nm. An explanation might be a bad step coverage or grain formation on the edges of the through hole. This was investigated by taking a SEM recording of a via (in this case 50 μm wide to improve the visibility of the step) after gold sputtering. Figure 9 shows grain formation at the step, thereby possibly creating a lower conductivity across the step. While the conductivity of the gold in a via is indeed 3 orders of magnitude lower than that of bulk gold, the resulting resistance is still in the order of 1 Ω which is eight orders of magnitude lower than the expected resistance of the liquid in the nanochannel.

Furthermore, table 3 shows that the PECVD silicon nitride behaves as required (see section 3.2.1 for the requirements). Namely, the breakdown voltage is more than an order of magnitude higher than required and the conductivity is close to the literature value (which is in the order of 1 nS/m [17]). The dielectric constant of the PECVD silicon nitride was not reliably measurable using our current setup and was, therefore, copied from literature [17].

The properties given in table 3 lead to the device specifications listed in table 4.

Table 4: Electrical device specifications

total parasitic resistance	1.8 GΩ +/-31%*
total parasitic capacitance	7.1 pF**
sustainable DC voltage	234 V +/-25%***

* Based the measured resistance of the PECVD silicon nitride

** Capacitive behavior chip: 7.1 pF theoretical value. Experimental value is not reliably measurable but is <<39 pF which is the parasitic capacitance of the wiring.

*** There was no significant difference between applying positive or negative DC potentials.

Table 4 shows a high value for the total parasitic resistance which is ~ three orders of magnitude larger than the resistance of a 100 μM KNO_3 solution (for which the expected resistance is ~0.4 MΩ). It furthermore shows that the parasitic capacitance is lower than the parasitic capacitance of the wiring we use. Comparing its value to the expected value for the capacitance caused by a 100 μM KNO_3 solution at the electrode interface, shows it is two to three orders of magnitude smaller (i.e. the expected capacitance at the electrode interface is between 100 pF and 1 nF).

In addition to the electrical measurements we checked the fabricated device optically. Figure 10 shows a photomicrograph of the electrodes and sacrificial layer at 100x magnification. From this photomicrograph we find that the electrodes are 2.6 μm wide and 1.4 μm apart. This a 30 % difference compared to the 2 μm for both the width and the separation of the electrodes in the mask design. The reason for this difference is probably a slight overexposure of the resist layer during lithography. Additionally we find that the sacrificial layer is approximately 5.9 μm wide. This is an 18% difference compared to the 5 μm in the mask design.

Although a lot of effort is put into the fine tuning of the lift-off process, still

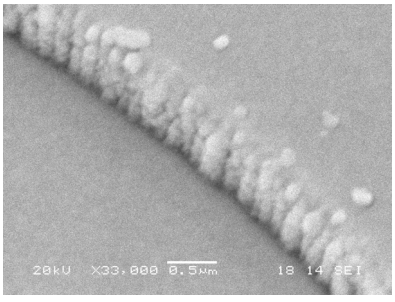

Figure 9: SEM recording of the step at the edge of a 50 μm wide via.

some edge effects were visible after metal deposition (figure 11). These, however could be relatively easily removed by 4 minutes of ozone treatment, which probably causes such a high thermal energy in the relatively thin curled-up edges that they release. The result of the ozone treatment can be seen by comparing figures 10 and 11.

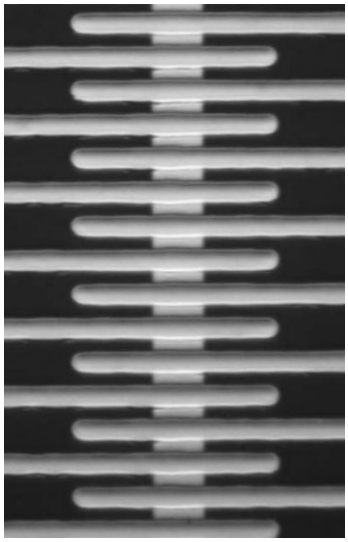

Figure 10: Photomicrograph at 100x magnification of the electrodes and sacrificial layer after lift-off of the electrodes and 4 minutes of ozone treatment. Note that the thin metal layer that surrounds the electrodes is gone.

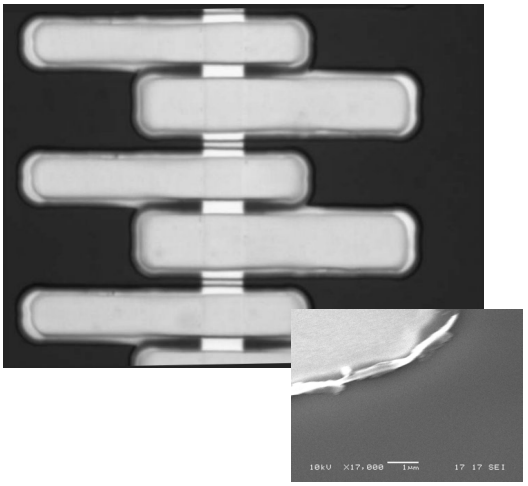

Figure 11: Photomicrograph at 100x magnification of the electrodes and the sacrificial layer after lift/off and prior to 4 minutes of ozone treatment. Note the curled metal layer that surrounds the electrodes. The inset shows a SEM picture of the curled up metal edges.

3.6 Conclusion

In this chapter the design and fabrication of traveling wave driven pumps in nanochannels were described. The fabrication steps also apply to the technologically more simple asymmetric devices. The technology used for fabrication is based on surface micro machining; and proved to be well-suited to fabricate nanochannels with noble metal wall-integrated electrodes. For analyte introduction PDMS based microchannels were bonded by plasma activation to the chip containing the nanochannels and electrode structure. Fabrication results were assessed both electrically and optically. The optical measurements show a small increase in feature size (<1 μm) as compared to the designed masks. The electrical measurements show that all measured specs are within the demands that were setup prior to fabrication.

References

1. Sparreboom, W., J.C.T. Eijkel, J. Bomer, and A. van den Berg, *Rapid sacrificial layer etching for the fabrication of nanochannels with integrated metal electrodes.* Lab on a Chip, 2008. **8**(3): p. 402-407.
2. Garcia-Sanchez, P., A. Ramos, N.G. Green, and H. Morgan, *Experiments on AC electrokinetic pumping of liquids using arrays of microelectrodes.* Ieee Transactions on Dielectrics and Electrical Insulation, 2006. **13**(3): p. 670-677.
3. Ramos, A., H. Morgan, N.G. Green, A. Gonzalez, and A. Castellanos, *Pumping of liquids with traveling-wave electroosmosis.* Journal of Applied Physics, 2005. **97**(8): p. -.
4. Karnik, R., R. Fan, M. Yue, D.Y. Li, P.D. Yang, and A. Majumdar, *Electrostatic control of ions and molecules in nanofluidic transistors.* Nano Letters, 2005. **5**(5): p. 943-948.
5. Plecis, A., R.B. Schoch, and P. Renaud, *Ionic transport phenomena in nanofluidics: Experimental and theoretical study of the exclusion-enrichment effect on a chip.* Nano Letters, 2005. **5**(6): p. 1147-1155.
6. Stein, D., M. Kruithof, and C. Dekker, *Surface-charge-governed ion transport in nanofluidic channels.* Physical Review Letters, 2004. **93**(3): p. -.
7. van Delft, K.M., J.C.T. Eijkel, D. Mijatovic, T.S. Druzhinina, H. Rathgen, N.R. Tas, A. van den Berg, and F. Mugele, *Micromachined Fabry-Perot interferometer with embedded nanochannels for nanoscale fluid dynamics.* Nano Letters, 2007. **7**(2): p. 345-350.
8. Eijkel, J.C.T., J. Bomer, N.R. Tas, and A. van den Berg, *1-D nanochannels fabricated in polyimide.* Lab on a Chip, 2004. **4**(3): p. 161-163.
9. Han, A.P., N.F. de Rooij, and U. Staufer, *Design and fabrication of nanofluidic devices by surface micromachining.* Nanotechnology, 2006. **17**(10): p. 2498-2503.
10. Mela, P., N.R. Tas, E.J.W. Berenschot, J. van Nieuwkasteele, and A. van den Berg, *Electrokinetic pumping and detection of low-volume flows in nanochannels.* Electrophoresis, 2004. **25**(21-22): p. 3687-3693.
11. Stern, M.B., M.W. Geis, and J.E. Curtin, *Nanochannel fabrication for chemical sensors.* Journal of Vacuum Science & Technology B, 1997. **15**(6): p. 2887-2891.
12. Turner, S.W., A.M. Perez, A. Lopez, and H.G. Craighead, *Monolithic nanofluid sieving structures for DNA manipulation.* Journal of Vacuum Science & Technology B, 1998. **16**(6): p. 3835-3840.
13. Abgrall, P. and N.T. Nguyen, *Nanofluidic devices and their applications.* Analytical Chemistry, 2008. **80**(7): p. 2326-2341.
14. Mijatovic, D., J.C.T. Eijkel, and A. van den Berg, *Technologies for nanofluidic systems: top-down vs. bottom-up - a review.* Lab on a Chip, 2005. **5**(5): p. 492-500.
15. Perry, J.L. and S.G. Kandlikar, *Review of fabrication of nanochannels for single phase liquid flow.* Microfluidics and Nanofluidics, 2006. **2**(3): p. 185-193.
16. Bard, A.J. and L.R. Faulkner, *Electrochemical methods : fundamentals and applications*. 2nd ed. 2001, New York: John Wiley. xxi, 833 p.

17. Lide, D.R., ed., *CRC Handbook of Chemistry and Physics, Internet version, _http://www.hbcpnetbase.com_*. CRC Press, Boca, Fl., 2005.
18. Mohanty, S. and D.J. Beebe, *Chips and Tips: PDMS connectors for macro to microfluidic interfacing*. Lab on a Chip, 2006. http://www.rsc.org/Publishing/Journals/lc/PDMS_connector.asp.
19. Olthuis, W., W. Streekstra, and P. Bergveld, *Theoretical and Experimental-Determination of Cell Constants of Planar-Interdigitated Electrolyte Conductivity Sensors*. Sensors and Actuators B-Chemical, 1995. **24**(1-3): p. 252-256.

Chapter 4

Rapid Sacrificial Layer Etching for the Fabrication of Nanochannels with Integrated Metal Electrodes

We present a rapid etch method to surface-micromachine nanochannels with integrated noble metal electrodes using a single metal sacrificial layer. The method is based on the galvanic coupling of a chromium sacrificial layer with gold electrodes, which results in a 10-fold increase in etch rate with respect to conventional single metal etching. The etch process is investigated and characterized by optical and electrochemical measurements, leading to a theoretical explanation of the observed etch rate based on mass transport. Using this explanation we derive some generic design rules for nanochannel fabrication employing sacrificial metal etching.

4.1 Introduction

Nanofluidic systems have an inherent large surface to volume ratio. This renders them interesting for integration with sensor and actuator systems, e.g. to manipulate and sense large bio-molecules such as DNA [1]. However, most nanofluidic systems reported in literature are fabricated by bulk micromachining [2-5], which complicates the integration into more complex systems [6,7]. In bulk-micromachining nanochannels are created by etching trenches and/or cavities in one wafer and bonding a second one on top of the first. An alternative to this fabrication method is surface-micromachining [6-11], where all structures are created on the surface of a single wafer and no bonding step is needed. In surface-micromachining a nanochannel is often created using a sacrificial layer which is covered by a thin film (capping layer). Different sacrificial materials have been proposed in literature [6,9,10]. However, most of them need to be etched away from one or both side-ends of the channel, which is a slow process (from days up to weeks depending on the length of the channels), because it is limited by the transport of etchant and waste products, usually by diffusion. Several solutions for this problem are given in literature [11-13], such as employing a sacrificial polymer that evaporates through the capping layer upon heating [12,13]. However, most of them require either special materials or geometries of the capping layer, which does not make them especially useful to create complex systems with for example integrated electrodes. Recently, a novel method was proposed [14] in which two dissimilar galvanically coupled metals are used as a sacrificial layer. The etch rate of this method is up to 10 times higher than in conventional methods.

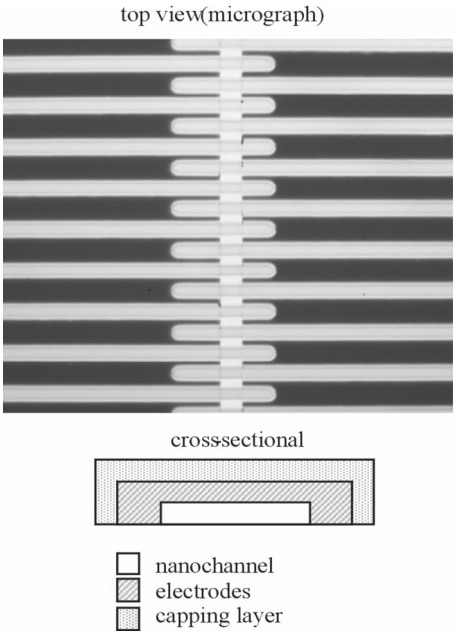

Figure 1: Micrograph and schematic drawing of the device prior to etching at 63x magnification. In this picture the nanochannel runs from top to bottom and the electrodes from left to right.

In this chapter we show that this method is eminently suitable to fabricate nanochannels with integrated bare electrodes using a single sacrificial metal layer. The method is based on the galvanic coupling of a sacrificial chromium layer with gold electrodes. In figure 1 a micrograph and a schematic front view of the device are given. In the future we plan to use this device to electrostatically manipulate ions and charged molecules in a nanochannel with double layer overlap as proposed in [6]. The electrodes can be actuated using traveling waves, as is done in microchannels by [15,16]. An additional application would be electrochemical and/or electric impedance sensing inside the channel. Furthermore, we provide a theoretical explanation of the enhanced etch rate based on mass transport considerations and we investigate the kinetics by performing polarization measurements. A thorough understanding of the underlying processes is important for the design of future devices. Finally, we offer some generic design rules for nanochannel fabrication employing sacrificial metal etching.

4.2 Theory

In this study we remove the sacrificial layer by a wet etchant and enhance the etch rate by galvanic coupling to gold. The etchant has two functions. First, electrochemically oxidize the metal by an electrochemical couple that is higher in the electrochemical series than the metal. Second, dissolve the generated metal ions. In this study the sacrificial metal is chromium and the etchant contains cerium(IV). In equation (1) the electrochemical reactions are given.

$$\begin{aligned} &Cr(s) \Leftrightarrow Cr^{3+}(aq) + 3e^- \\ &Cr(s) + 3Ce^{4+}(aq) \Leftrightarrow Cr^{3+}(aq) + 3Ce^{3+}(aq) \\ &3Ce^{4+}(aq) + 3e^- \Leftrightarrow 3Ce^{3+}(aq) \end{aligned} \tag{1}$$

Because cerium(IV) is higher in the electrochemical series than chromium the reaction above will go from left to right and the chromium is etched. The higher the difference in standard potential between the metal and the etchant the higher the etch rate in a bulky etchant. There are two ways of obtaining an additional increase in etch rate of a metal: First, galvanic coupling to a metal with a higher standard potential. Second, applying an external electric potential to the metal that is positive with respect to the etchant. The first case can only be applied in combination with an etchant, the second can be applied without, however the metal should be in contact with an electrolyte that is able dissolve the generated metal ions. In this chapter we test 1 and a combination of 1 and 2.

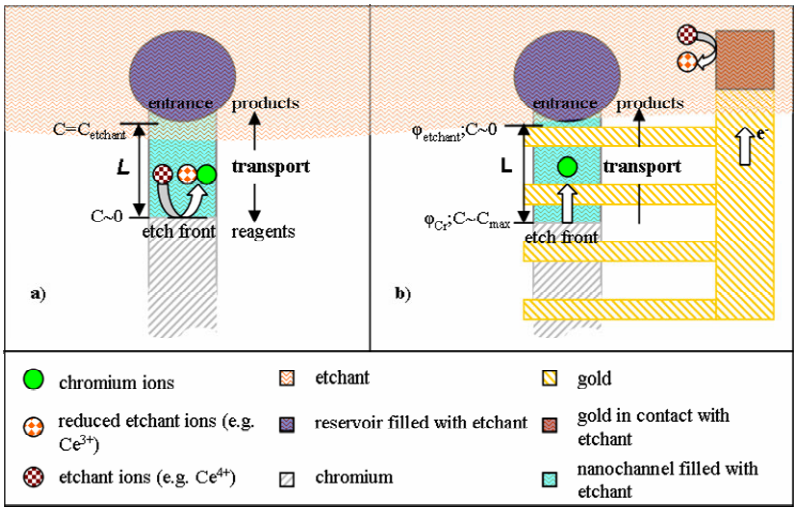

Figure 2: Proposed etching mechanisms: a) Single metal sacrificial layer, transport is diffusion driven. The driving concentration difference is ~0.2 M. b) Galvanically coupled sacrificial layer, transport diffusion and migration driven. The driving concentration difference can be up to 5 M, depending on the metal and the etchant.

We assume that etching in our system is a steady state process and that the Nernst equation applies, therefore, we can describe the electric potential of chromium by equation (2).

$$E = E_{0,Cr} + \frac{RT}{z_+ F} \ln\left(\frac{Cr^{3+}(aq)}{Cr(s)}\right) \tag{2}$$

Here, E_0,Cr [V] is the standard electrode potential of chromium; F [C mol^{-1}] and R [J K^{-1} mol^{-1}] represent the Faraday and the universal gas constant, respectively; z^+ [-] is the valence; T [K] is the temperature and Cr^{3+}(aq) [mol.m^{-3}] and Cr(s) [mol.m^{-3}] represent the concentration of chromium ions and solid chromium, respectively. In electrochemistry Cr(s) is usually taken unity [17]. Equation (2) shows that as the concentration of chromium ions increases, the potential of the chromium increases. The consequence of this is that the potential difference between the chromium and etchant is effectively decreased for increasing chromium ion concentrations at the metal interface, thereby, decreasing the etch rate. In our system reagents and products have to be transported through a 1-D channel, therefore, mass transport is probably a limiting factor as in most systems where convection is negligible [17]. This means that as the potential difference increases, the concentration of chromium ions at the metal surface increases which counteracts the increase in potential difference. Therefore, there will be a steady state etch rate based on the trade-off between potential difference and mass

transport limitations. In the following subsection two etching mechanisms based on mass transport are proposed.

Proposed etching mechanisms

We derived two concepts for etching, one for a single metal sacrificial layer and one for galvanically coupled metals where the chromium forms the sacrificial layer (see figure 2). In the first case, the etching of the chromium and the reduction of the etchant both occur at the etch front. Therefore, transport is limited by the diffusion of reagents to and reaction products from the etch front. In the second case, the oxidation of the metal occurs at the etch front in the nanochannel, whilst the reduction of the etchant occurs both at the etch front and outside the channel at the gold surface. Since, the gold surface is much larger and more easily accessible, the reduction will occur mainly at the gold surface outside the channel. In this case, chromium transport is driven not only by diffusion, but also by migration of reaction products from the etch front due to the potential difference between the metal and the electrolyte. Furthermore, the diffusional transport in the second case can be much higher, because it is only limited by the maximum solubility of chromium and not by the etchant concentration as in the first case. The magnitude of the concentration difference that drives the diffusional transport is dependent on the energy level and hence the electric potential of the metal couple with respect to the etchant.

Mass transport is assessed by the Nernst-Planck equations [18]. These equations describe the current density as a function of diffusion, migration and convection. In our analysis we neglect convection and only consider diffusion and migration. Because of the 1-D geometry of the channel, we will only consider longitudinal mass transport. For clarity, below the simplified equations are given.

$$i_+ = -D_+ F z_+ \frac{\partial c_+}{\partial x} - \frac{F^2 z_+^2 D_+ c_+}{RT} \frac{\partial \varphi}{\partial x} \tag{3a}$$

$$i_- = -D_- F z_- \frac{\partial c_-}{\partial x} - \frac{F^2 z_-^2 D_- c_-}{RT} \frac{\partial \varphi}{\partial x} \tag{3b}$$

Here, $i_\pm$ [A m^{-2}] describe the current density caused by cation and anion transport, respectively; $D_\pm$ [m^2 s^{-1}], $z_\pm$ and $C_\pm$ [mol m^{-3}] represent the diffusion constants, the valence (i.e. positive for cations and negative for anions) and the concentration of the ions in the system, respectively; φ [V] represents the electric potential and x [m] is the position and is defined in the axial direction. To avoid creating a (complicated) moving boundary problem, we assume that the movement of the etch front does not affect the amount of chromium ions per unit time generated at the etch front and removed from it, which results in the assumption that the concentration of chromium ions at the etch front is constant in time. Furthermore, we assume that the electric current in the system with the etch front at a specific position is constant. To translate current density to the length, L [m], which has been etched, we derived the following equation.

$$L = \sqrt{2 \int_0^L \int_0^t \frac{MW}{\rho} \frac{i_+}{zF} dt dx} \tag{4}$$

Here MW [kg m^{-3}] and ρ [kg mol] are the molecular weight and the density of chromium, respectively and t [s] is the elapsed time. To derive an equation that describes L as a function of the concentration at the etch front, we solved equation (3a) for c_+. For this derivation we used a comparable method to [18]. With the assumptions made above, in this case, the migration of anions towards the etch front is counterbalanced by their diffusion away from the etch front. This results in a zero net current of anions, so we can express the potential gradient as a concentration gradient by solving equation (3b) for $i_-=0$.

$$\frac{\partial \varphi}{\partial x} = -\frac{RT}{Fz_- c}\frac{\partial c}{\partial x} \tag{5}$$

We substitute the result in equation (3a). After substitution, we integrate equation (3a) with respect to x and rearrange terms to obtain the concentration of chromium ions as a function of position, $c(x)$. As a boundary condition at the channel entrance we use $c=c_b$, where c_b [mol m^{-3}] is the bulk concentration of chromium ions. The result is given in equation (6).

$$c(x) = c_b + \frac{i_+ x}{D_+ F \nu_- (z_+ - z_-)} \tag{6}$$

Here x is defined as zero at the channel entrance and L at the etch front. $\nu_\pm$ [.] is the number of positive and negative ions per salt molecule. We then calculate the limiting current density using equation (6).

$$i_{\lim} = \frac{c_{\max}}{L} D_+ F \nu_- (z_+ - z_-) \tag{7}$$

Here c_{max} [mol m^{-3}] is the maximum solubility of chromium in the etchant. Equation (7) states that the limiting current density is determined by the maximum solubility of chromium and the length of the channel. As a consequence the same limitation holds for the maximum obtainable etch rate.

By substituting equations (5) and (6) into (3a) and substituting the result in (4) we are able to solve equation (4). The result is given in equation (8) and with this equation we can compare our theory with experimental data.

$$L = \sqrt{2\frac{MW}{\rho}\left(1 - \frac{z_+}{z_-}\right) D_+ c(L) t} \tag{8}$$

As mentioned above the concentration at the etch front depends on the potential difference between the metal and the electrolyte. With equation (8) the influence of changes in the concentration of chromium at the etch front on the etch rate can be clearly seen. The influence of migration can be assessed using the $(1-z_+/z_-)$ term in equation (8). Furthermore, it shows that the etch rate is not a function of the lateral

dimensions of the channel. This is in correspondence with the experimental observations made in [14].

Equation (7) shows that the current and thus the etch rate is limited by the maximum solubility of chromium in the etchant. However, as mentioned above $c(L)$ counteracts electric potential difference and, therefore, in galvanically coupled sacrificial layers, $c(L)$ does not necessarily have to be equal to the maximum solubility of the metal in the etchant. The actual kinetics of this process as a function of the potential difference between the metal couple and the etchant can be examined by performing polarization measurements [17]. Such experiments usually consist of three steps. First, the potential where there is zero current (the anodic and cathodic currents are equal to the corrosion current, i_{corr}) is determined. This is the potential at which etching occurs naturally and we will further refer to this potential as the corrosion potential, E_{corr}. The magnitude of E_{corr} is determined by the choice of metals and etchant. Second, the potential is scanned through values lower than E_{corr}. In this potential regime reduction at the cathode (i.e. reduction of the etchant) will be the dominant reaction. Third, the potential is scanned through values higher than E_{corr}. At these potentials oxidation at the anode (i.e. oxidation/etching of chromium) will be the dominant reaction. Because we are interested in the kinetics of the etching reaction only the first and third step are performed. If during this experiment the electric current between the couple and the electrolyte is monitored, a polarization plot can be obtained. In order to compare the results of these measurements with theory we use the current-voltage characteristic from [17].

$$i = \frac{-\exp\left[z_+ F\left(E - E_{corr}\right)/RT\right]}{\frac{1}{i_{corr}} + \frac{1}{i_{\lim}}\exp\left[z_+ F\left(E - E_{corr}\right)/RT\right]} \qquad c(L) >> c_b \tag{9}$$

This equation is only valid for our system if $c(L)>>c_b$. This equation describes the oxidation/etch current as a function of the potential between the metal and the electrolyte, E, and takes both the reaction kinetics and the current limitation by mass transport into account. We will present the results of these measurements below.

4.3 Experimental

4.3.1 Fabrication

We have fabricated 4 mm long, 5 μm wide and 50 nm high nanochannels with 1000 integrated electrodes. The electrodes are 3 μm wide and 1 μm separated and run across the entire channel width. In our system the metal couple is chromium and gold, where only the chromium acts as the sacrificial part. The gold remains, because it is inert to the etchant, and forms the integrated electrodes. As an etchant standard chromium etch (Merck, 111547.2500) is used. The active component (i.e. oxidizing species) in this etchant is cerium(IV). The fabrication process is described in figure 3.

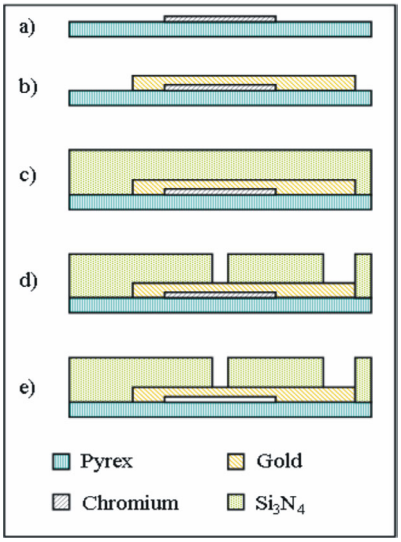

Figure 3: Fabrication process: a) deposition of a sacrificial chromium layer b) deposition of gold electrodes, c) deposition of a 2 µm nitride layer by PECVD, d) ion beam etching of access holes, and e) standard wet chemical etching of the sacrificial chromium layer.

4.3.2 Methods

We attached the chip to the bottom of a Petri dish and made all necessary electric connections (see figure 4). Subsequently, we added etchant such that the chip and the additional electrodes, necessary for the experiments, were immersed. We observed the etching process using an inverted microscope (Leica DM IRM) equipped with a digital camera (Olympus CC-12) focused at the etch front. During etching we also measured the potential between the chromium/gold couple and the etch solution using a potentiostat (PARSTAT 2263) and a double junction AgAgCl/saturated KCl/saturated KNO_3 reference electrode (Radiometer REF251). The reason we used a double junction reference electrode is to prevent the introduction of chloride ions to the system which may influence the etch process. In figure 4 a schematic of the experimental setup is given. As mentioned above the reaction occurs at E_{corr}, which can be measured by applying a potential to the system such that there is no net current (i.e. the cathodic and anodic currents cancel) between the chromium/gold couple and the electrolyte. Furthermore, we performed potential sweeps 300 mV beyond E_{corr}, and meanwhile we observed the movement of the etch front with the microscope.

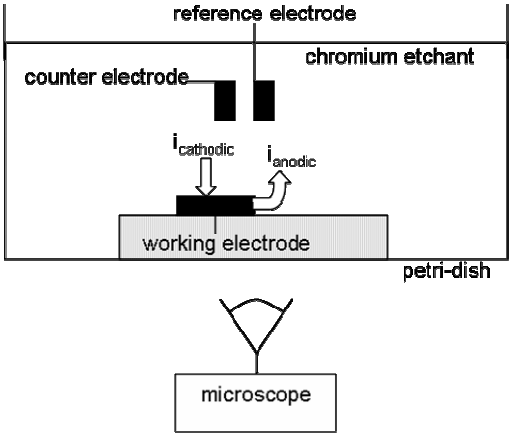

Figure 4: Schematical representation of the experimental setup. The device is connected with its chromium/gold couple to the working electrode of the potentiostat by conductive paint and subsequent silicone coating for isolation.

4.4 Results and Discussion

Figure 5 shows a channel which has been partially etched. In this micrograph the etch front can be clearly observed. During etching we monitored the movement of the etch front as a function of time. The results of this measurement are given in figure 6.

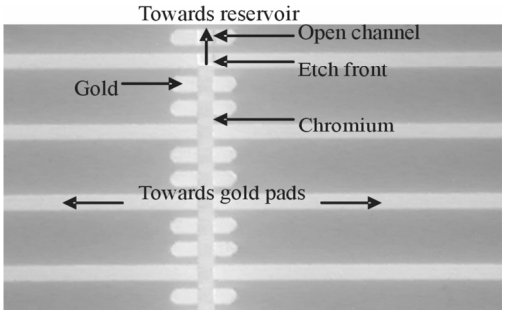

Figure 5: Micrograph of the device during etching at 63x magnification.

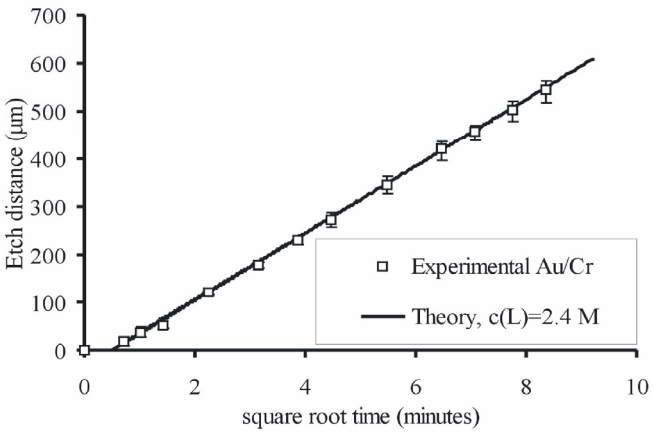

Figure 6: Position of the etch front with respect to the channel entrance as a function of the square root of time. The error bars represent the variation in data of 5 different experiments.

To determine the theoretical etch behavior we compared the experimental data to equation (8), while using $c(L)$ as a fit parameter. The results are given in figure 6. Clearly, the theoretical fit and the measurements coincide well. However, for smaller etch distances the etch rate appears to be slower. This could indicate that first a chromium oxide layer needs to be removed.

Comparison of the presented value of $c(L)$ to the maximum solubility of chromium in the etchant (i.e. 5.5 M) shows that the etch rate is not at its theoretical maximum. Therefore, increasing the potential of the metal couple with respect to the etchant should theoretically increase the etch rate. To investigate the influence of a change in potential on the etch rate, we performed polarization measurements, as described above. We observed clear changes in the etch rate upon the application of different potentials. The measurements were performed after 700 µm of the channel had been etched. In figure 7 we plotted the current density as a function of an externally applied potential. The experimental curve is obtained by optical inspection of the etch front. The current density is calculated by dividing the measured currents by the cross-sectional area of the channel. Moreover, we plotted two theoretical curves based on equation (9). Figure 7 shows that by increasing the potential beyond E_{corr} the anodic current density (i.e. the etch rate) increases, and by decreasing the potential it decreases. We observed that by applying an external potential to the metal couple the etch rate can be further increased by a factor of two in comparison to a galvanic couple without an externally applied potential. Furthermore, the figure shows that there is a maximum current density, i_{lim}, determined by the maximum concentration of chromium at the etch front as predicted in the theoretical section. Figure 7 shows that at i_{lim} the theoretical curves are in good agreement with the experiments. However, using the tabulated value of the solubility of chromium the current density is slightly overestimated. This is probably caused by the fact that we did not take the conductivity

of the etchant into account which results in an overestimation of the current density for a given concentration difference. The reason for this is that the potential difference in the system also causes a migration current of the ions in the etchant and, therefore, a part of the migration current is carried by these ions and not by the chromium ions.

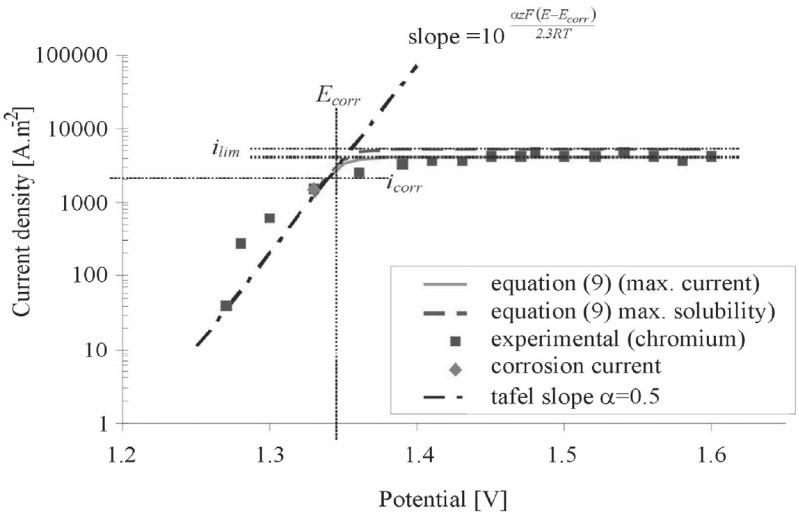

Figure 7: Polarization measurements including theoretical curves. The theoretical curves are determined using equation (9) in two ways. -: via the maximum measured current; - -: via the tabulated value of the maximum solubility.

In figure 7 we also plotted a Tafel slope which describes the current density as a function of potential if the chromium dissolution is primarily determined by the reaction kinetics and mass transport does not play a role [17]. Figure 7 shows that at current densities below i_{lim} the experimental curve does neither coincide well with the theoretical curve, nor with the theoretical Tafel slope. This indicates that the etch rate at this etch distance (700 µm) is determined by mass transport rather than reaction kinetics.

To further test our characterization we compared our results with experimental data of a copper/chromium sacrificial layer presented in [14]. The results of the comparison are given in table 1 and show that our theoretical analysis is in close agreement with values given in literature.

Table 1: Experimental and theoretical etch rates. Literature and present values.

	present data [µm/sqrt(min)]	**literature data** [14] [µm/sqrt(min)]
Experimental	65	72
Theoretical	64.8	74.7

Finally, we consider some consequences of our theory for the design of future nanochannel devices. For devices longer than 4 mm the measured etch rates will still be somewhat slow, so in order to further increase the etch rate, E_{corr} should be increased. This can be done by applying an external potential to the metal couple as we showed above or by electrochemically increasing the potential difference between the two metals in the etchant. The potential between the two metals depends both on the choice of metals and the choice of etchant as discussed in the theoretical section. However, as shown in figure 7 the maximum solubility of the metal in the etchant always determines the limiting etch rate. Therefore, in table 2 we present the maximum obtainable etch rates for several metals, often used in micromachining. The etch rates are based on the maximum solubility in a given etchant. In our analysis we assume a channel length of 1 mm.

Table 2: Predicted etch properties for a 1 mm long nanochannel

Material	**Counter ion**	c_{max} [M]	i_{lim} [A/m^2]	**Maximum etch rate** [µm/sqrt(min)]	**Etch time** [min]
chromium	Nitrate	5.5	5413	107	22
copper	Nitrate	5.0	4107	95	28
aluminum	chloride	3.2	3961	91	30

Table 2 shows that for chromium and aluminum the highest and lowest etch rates can be obtained, respectively, which is a useful observation if an external potential is applied. Differences, however, are small. If to reduce the complexity of etch setup no external potential is applied, table 2 can be used as a guideline, however, the inherent properties of the metals and the etchant should also be considered. For example, if we consider chromium as the sacrificial metal, it should be noted that chromium appears to have a higher standard electrode potential than expected from literature [14], which effectively decreases its potential with respect to that of the etchant and of the more cathodic metals. This is according to [19] caused by its passivity effect which is an energy barrier on the chromium/electrolyte interface. The same holds for aluminum, which appears to have the advantage that it is very low in the electrochemical series, which means that the potential difference with almost any other metal (which is suitable for micromachining) will be high. Therefore, in order to decide on the metal couple with the highest etch rate additional experiments with different metals are necessary.

4.5 Conclusions

We present an etch method for surface micromachining of nanochannels with bare integrated electrodes using a single metal sacrificial layer. An advantage of the etch method is that it is ten times faster than conventional sacrificial methods. Furthermore, a theory based on mass transport using the Nernst-Planck equations is presented that describes the observed etch rates well. To further investigate the kinetics of the etch process we performed polarization measurements. These measurements indicate that etch rates can be further increased by a factor of two by applying an external potential to the metals. The theory we developed enables predictions of etching behavior for future devices using externally applied potentials. For systems employing different sacrificial or electrode metals, however, additional experiments are necessary.

References

[1] J. Eijkel and A. van den Berg, Microfluidics and Nanofluidics, 2005, 1, 249-267.
[2] D. Mijatovic, J. Eijkel and A. van den Berg, Lab Chip 2005, 5, 492-500.
[3] J. Haneveld, H. Jansen, E. Berenschot, N. Tas and M. Elwenspoek, J. Micromech. Microeng., 2003, 13, S62-S66.
[4] R. Karnik, R. Fan, M. Yue, D. Li, P. Yang and A. Majumdar, Nano Lett., 2005, 5, 943-948.
[5] A. Plecis, R.B. Schoch and P. Renaud, Nano Lett., 2005, 5, 1147-1155.
[6] M.B. Stern, M.W. Geis and J.E. Curtin, J. Vac. Sci. Technol., B, 1997, 15 2887-2891.
[7] A. Han, N.F. de Rooij and U. Staufer, Nanotechnology, 2006, 17, 2498-2503.
[8] J.C.T. Eijkel, J. Bomer, N.R. Tas and A. van den Berg, Lab Chip, 2004, 4, 161-163.
[9] M. Foquet, J. Korlach, W. Zipfel, W.W. Webb and H.G. Craighead, Anal. Chem., 2002, 74, 1415-1422.
[10] S.W. Turner, A.M. Perez, A. Lopez and H.G. Craighead, J. Vac. Sci. Technol., B, 1998, 16, 3835-3840.
[11] N.R. Tas, J.W. Berenschot, P. Mela, H.V. Jansen, M. Elwenspoek and A. van den Berg, Nano Lett., 2002, 2, 1031-1032.
[12] W.L. Li, J.O. Tegenfeldt, L. Chen, R.H. Austin, S.Y. Chou, P.A. Kohl, J. Krotine and J.C. Sturm, Nanotechnology, 2003, 14, 578-583.
[13] D.A. Czaplewski, J. Kameoka, R. Mathers, G.W. Coates and H.G. Craighead, Appl. Phys. Lett., 2003, 83, 4836-4838.
[14] H. Zeng, Z. Wan and A.D. Feinerman, Nanotechnology, 2006, 17 3183-3188.
[15] G. Fuhr, R.Hagedorn, T. Müller, W. Benecke and B. Wagner, J. Microelectromech. Syst., 1992, 1, 142-146
[16] A. Ramos, H. Morgan, N.G. Green, A. González and A. Castellanos, J. Appl. Phys., 2005, 97, Art. No. 084906.
[17] A.J. Bard and L.R. Faulkner, Electrochemical methods: Fundamentals and applications, 2nd edition, Wiley Interscience, 2001, ISBN: 978-0-471-04372-0.

[18] R.F. Probstein, Physicochemical hydrodynamics: An introduction, 2nd edition, Wiley Interscience, 1994, ISBN: 0-471-45830-9.
[19] H.P. Hack, Galvanic corrosion, Philadelphia, PA: ASTM, 1988.

Chapter 5

Bi-directional Pumping in Nanochannels Using Integrated Asymmetric Electrode Arrays: Modeling

Flow induced at asymmetric electrodes integrated in a 50 nm high nanochannel is numerically modeled using a finite element method. Ionic transport is described using the full Nernst-Planck equations incorporating the influence of diffusion, migration and convection on transport. Flow of liquid and ions is viscously coupled by employing the Stokes equations. A pulsating flow with a net direction was found to be induced by applying sinusoidal waves to the electrodes. The situation of both overlapping and thick double layers was simulated. To interpret the results, an intuitive picture of the device operation is sketched and analytical equations for the frequency behavior are given.

In the case of overlapping double layers three optimal driving frequencies (50, 200 and 2000 Hz) are found, where both negative and positive velocities occur. In the case of thick non-overlapping double layers only two optimal driving frequencies are found (100 and 2000 Hz), showing both positive and negative velocities.

The induced flow velocity as a function of applied AC potential shows a deviation in behavior commencing beyond 300 mV. In contrast to classical behavior observed in microchannels where the velocity is approximately proportional to the applied AC potential squared, we observe a quasi linear relationship between velocity and applied potential.

5.1 Introduction

Pumping in nanochannels has historically been largely performed by electrokinetic actuation [1,2]. The reason for this is twofold. For one, the linear flow velocity induced by electrokinetics is independent of the channel height (i.e. if electric double layer (EDL) overlap is not considered), whereas for example the velocity in pressure driven flows scales inversely proportional to the channel height squared. Secondly, the electrostatics governing the potential distributions have a length scale (i.e. Debye length, λ_D) in the same order of magnitude as the channel height, which makes nanochannels interesting devices for studying electrostatic interactions, for example between channel walls and charged (bio)-molecules. This influence of electrostatics is even more interesting, because most biomolecules (e.g. DNA, proteins) have a nanometer size, are highly charged and are surrounded by their own EDL [3]. The interactions resulting from the introduction of such molecules into nanofluidic channels and the application of electric fields (for actuation and/or probing) can possibly lead to new separation and/or analysis tools [4-6]. However, while electrokinetics are often applied to nanochannels, up to now little attempt has been made to use more direct methods for ion manipulation with integrated wall electrodes. Although quite some attention has been paid to buried electrodes in nanochannels in order to manipulate the amount and type of double layer overlap [7], no active pumping methods using wall-integrated electrodes have been performed. Advantages of doing so are numerous. Electric fields to manipulate and to transport charged molecules can be applied locally and generally require small driving voltages (<1 V). Moreover, sensing for example by impedance spectroscopy using superposition of a measurement signal on top of the actuation signal becomes easily feasible [8,9]. This chapter presents simulation results of an ion pump that consists of a one-dimensional 50 nm high nanochannel with an integrated asymmetric micro-electrode array. Electrodes are bare, i.e. in direct contact with the electrolyte. The device is able to pump ions and solution by applying low (< 1 V) AC voltages to the electrode array. In microchannels this effect is named AC-electro-osmosis (AC-EO), and a single pumping direction is observed which is maximal at a certain applied frequency [10,11]. The operation in nanochannels with thick or even overlapping electric double layers will proof to be quite different. In this chapter we will show that theory predicts the existence of multiple characteristic frequencies instead of one. The pumping effect becomes more pronounced for higher applied amplitudes, (>200 mV) however, theory predicts a saturation effect beyond 300 mV. As in microchannels the efficiency of the pump depends on applied frequency and potential.

The chapter is organized as follows. In section 2 the principles of operation (including different operation regimes) are explained by using standard network elements (i.e. resistors and capacitors). This formalism will be used to briefly describe in an insightful manner the essence of the outcome of the finite element model which will be presented in more detail in section 4. In section 3, more extensive theory is given that leads to this finite element model. With this model we are able to predict flow velocities as a function of applied voltage and frequency and of chosen geometry (i.e. amount of asymmetry, characteristic lengths). In section 4 finally, the result of numerical simulations employing this model are presented and discussed. The influence

of the different experimental parameters mentioned above on the velocity is thereby investigated.

5.2. Principle of operation

5.2.1 AC electro-osmotic flow in microchannels

In this subsection the operational mechanism of the AC-EO micropump are introduced and explained in a qualitative manner. For clarity a typical device geometry employed in AC-EO micropumps is given in figure 1.

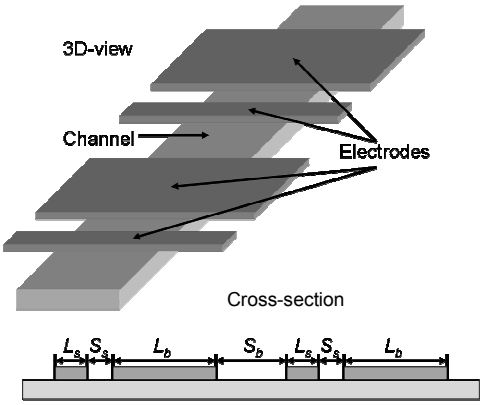

Figure 1: Schematical overview of the device geometry typically employed in AC-EO

As first proposed by Ramos et al. [11] AC-EO device operation can be explained and understood by modeling the device by an equivalent circuit consisting of standard network elements such as resistors, R, and capacitors, C. In microchannels the height of the channels is in the same order of magnitude as the length scale of the electrodes, and the resistances between the electrodes can, therefore, be modeled by semi-circular conduction lanes (figure 3). Since the conduction lane connecting the two inner parts of an electrode pair is shorter than the subsequent conduction lanes the resistance R in this first conduction lane is smaller than subsequent ones, where R continues to increase for increasing distance from the inner electrode edge. This results in an increase in RC time for conduction lanes at an increased distance from the inner electrode edge. At a frequency that corresponds to the RC time of the inner conduction lane the inner sides of an electrode pair are charged most and, therefore, shielded most. This induces an electric field that in case of AC-EO in microchannels always induces a force directed from the center of an electrode towards the edge (i.e. the reason the direction of the induced force is always directed outwards is that on a negative electrode the charge is positive and the field outwards and on a positive electrode the charge is negative and the field inwards, both resulting in a Coulomb force directed outwards). For an AC-EO

pump (or any pump based on electrokinetics) to work, both an electric field, E [V.m^{-1}], and a local net charge, q [C] are necessities. If both are available, a force E times q [N] is exerted by the field E on q and by viscous coupling the charge exerts a body force on the liquid. A schematical view of the description given above is presented in figure 2. The availability of E and q depends on the frequency of the applied driving signal. For frequencies that are very low (lower than the inverse of the RC time corresponding to the outer conduction lane), q is available since there was sufficient time to attract it to the electrodes, but is uniformly distributed thereby not resulting in an induced field E at the electrodes. For frequencies that are too high, E is available, but q does not have enough time to develop at the electrode surface. For intermediate frequencies both E and q are available and pumping can be performed. Here a net velocity is obtained by making one of the electrodes longer, thus inducing a large and a small fluid roll in the liquid. The roll on the large electrode is dominant and determines the net direction of flow. Therefore, the directionality because of asymmetry in electrode size of AC-EO in microchannels is a pure hydrodynamic effect.

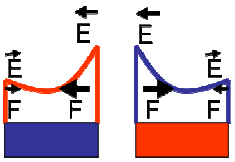

Figure 2: Non-uniform charging of the electrodes and resulting electric fields. Also the resulting Coulomb forces are given. This induces fluid rolls in the liquid with a diameter in the order of the electrode length. A net liquid flow is induced by making an asymmetry in electrode size, thus creating two different fluid rolls of which the big one is more dominant in determining the net flow direction. Blue and red respectively refer to negative and positive potential/space charge.

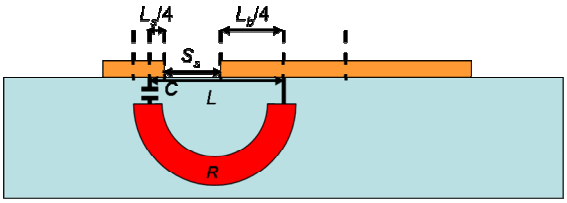

Figure 3: Schematical representation of the RC network as commonly defined to describe the dynamical behavior of AC-EO micropumps.

Theoretically, the optimal driving frequency in AC-EO in microchannels is often defined as the inverse RC time of 50% of the electrode surface. This means that the C is calculated using half the surface area of the small electrode (if assuming a large asymmetry then this is the dominant C) and R is based on a semi circular conduction lane with a diameter equal to, L [m], which is defined as the distance, S_s, between the

two electrodes added to $L_s/4$ and $L_b/4$ (for the symbols used see figure 3). This results in an approximation for the optimal driving frequency of AC-EO devices given by

$$\omega = \frac{1}{RC} = \frac{\sigma}{\varepsilon}\frac{\lambda_D}{\pi L} \tag{1}$$

Equation 1 is only valid for systems of large asymmetry, so for $L_b >> L_s$. Here ω [$2\pi.s^{-1}$] represents the angular frequency, R [$\Omega.m^2$] the resistance of the conduction lanes and C [$F.m^{-2}$] the double layer capacitance of the electrodes. Furthermore σ [$\Omega^{-1}.m^{-1}$] and ε [$F.m^{-1}$] are the conductivity and the permittivity of the solution, respectively, and λ_D [m] is the Debye length, $\sqrt{\frac{\varepsilon RT}{2z^2F^2c_0}}$. In the latter equation R [$J.K^{-1}.mol^{-1}$] represents the universal gas constant; T [K] the absolute temperature; z [.] the ionic valence; F [$C.mol^{-1}$] the Faraday constant and c_0 [$mol.m^{-3}$] the solution bulk salt concentration.

5.2.2 AC electro-osmotic flow in nanochannels

5.2.2.1 Ionic charging

In the nanochannels examined in this thesis, the height of the channel is typically 2 orders of magnitude smaller than the characteristic length of the electrode array, because of restrictions on the electrode width imposed by standard photolithography. Therefore, a more adequate representation for the conductive lanes is needed, with linear instead of semi-circular lanes running from one electrode to another as shown in figure 4. Olesen et al. [12] predicted theoretically that confinement in height (while keeping the size of the electrodes unaltered) will cause a negative shift in optimal driving frequency due to the decrease in conduction volume for decreasing channel heights. By assuming linear conduction lanes between electrodes, we can modify equation (1) to account for the effect of the confinement in channel height. This is done by multiplying equation (1) with $2\pi h/L_s$ term obtaining:

$$\omega = \frac{1}{RC} = \frac{\sigma}{\varepsilon}\frac{\lambda_D 2h}{LL_s} \tag{2}$$

Note that equation (2) is only valid for $h << L$ and for large asymmetry $L_b >> L_s$. While confinement certainly decreases conduction volume and thereby increases the R term in the RC characteristic time, confinement in channel height in nanofluidic channels will eventually lead to thick EDLs and even EDL overlap. This requires ion enrichment/exclusion effects to be taken into account. Plecis et al. [13] described ion enrichment/exclusion both theoretically and experimentally. For a 50 nm high glass

channel and a bulk ion concentration of 100 µM, EDLs overlap and ion enrichment/exclusion occurs at a pH of 7 for counter-ions/co-ions, respectively.

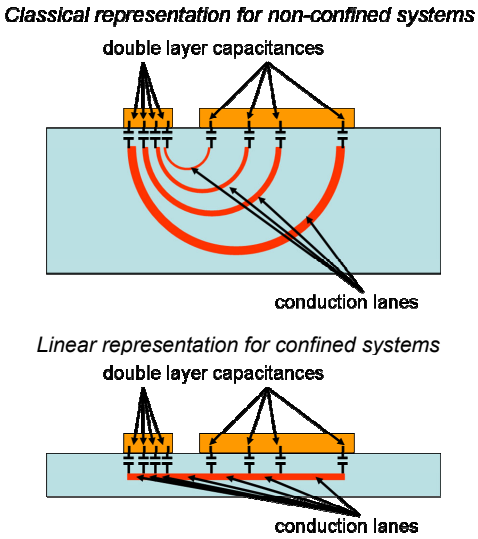

Figure 4: Representation of conductive pathways through a liquid between an electrode pair. Here the classical representation for channels approximately as high as the length of the electrode pair is shown in the top picture. A more adequate representation for channels that are much lower than the length of the electrode pair is shown in the bottom picture.

Plecis et al. introduced the following analytical expression for the factor β [.] which quantifies the ion enrichment/exclusion.

$$\beta = \frac{1}{h}\int_0^h \exp\left[-\frac{\xi\cosh\left((h/2-y)/\lambda_D\right)}{\cosh\left(h/2\lambda_D\right)}\frac{zF}{RT}\right]dy \qquad (3)$$

Here h [m] and y [m] represent channel height and position in the vertical direction. The other parameters were already defined above. Ion enrichment or exclusion in glass nanochannels at pH 7 can be calculated by using positive or negative values for z, respectively. We will further refer to respectively β_+ or β_- for the enrichment or exclusion of respectively cations and anions. $\beta_\pm$ can be used as a scaling factor in equation (2) to incorporate ion enrichment/exclusion effects. It is important to note that incorporating $\beta_\pm$ into equation (2) results in charging processes of cations and anions with different time constants. This means that, since periodic driving signals are considered, in one half of the period the charging of the positive electrode of a pair is much slower as compared to charging of the negative electrode. This will have important consequences on the device behavior as will be elucidated later in this section. For nanochannels with a negative surface charge we have:

$$\omega_{+} = \frac{\sigma}{\varepsilon}\beta_{+}\frac{h\lambda_D}{LL_s}$$
$$\omega_{-} = \frac{\sigma}{\varepsilon}\sqrt{\beta_{-}}\frac{h\lambda_D}{LL_s} \quad (4)$$

Here, ω_+ [$2\pi.s^{-1}$] and ω_- [$2\pi.s^{-1}$] refer to the angular frequencies below which cations and anions charge the respective electrode surfaces more and more uniformly. It is in view of applying an effective Coulomb force important to note that operation below these frequencies means a decrease in induced electric field. The reason why ω_+ has β in its numerator and ω_- has $\sqrt{\beta}$, is because in the case of cations, only the conductance is dominantly altered as compared to the microchannel case; in the case of anions, however, both the conductance and the capacitance are altered as compared to the microchannel case, because λ_D has an inverse square root dependence on concentration and the concentration of anions is drastically decreased with respect to the microchannel case. The increase in cations is expected not to dominantly influence the capacitance, since the cations are electrostatically attracted in the perpendicular direction towards the opposing walls and hence the increase in amount will not, in a steady state case, contribute to an increase in capacitance of the electrode. Note that the equations (4) apply to the case of negatively charged channel walls, where the cations are the counterions and anions the co-ions.

Equations (4) give for the system at hand a frequency of ~1 kHz for cations and of ~10 Hz for anions. Although 10 Hz is a frequency that will be tested in the current analysis, a dominant Coulomb force is not applied to the anions since they are even at 10 Hz outnumbered by the cations (i.e. by the cations that have accumulated on the opposing glass wall) which can, therefore in this system be seen as the majority carriers of mobile charge. They, however, play a role in the distribution of q at the electrode surface at these low frequencies.

Since the system at hand has overlapping double layers, q is available at nearly all times and all positions in this system. To generate an axial Coulomb force qE, it is furthermore important to have axial electric fields. These can, as seen above, be induced by non-uniform charging of the electrodes. In our numerical analysis which will be presented in section 4 of this chapter, we found that non-uniform double-layer charging on the large electrode has the strongest influence on the resulting flow in the channel. Therefore, it is most adequate to determine the frequency below which this non-uniformity of the induced charge on the large electrode starts to disappear and becomes replaced by a uniform distribution across the surface of the electrode due to migration. This charge redistribution process can be described by a capacitor with a surface equal to half the total surface that can be charged and discharged via a resistor with a length of half the total length of the electrode. The characteristic frequency for this charging process can be derived from this RC model, and since cations are the majority carriers only the equation for cations will be given here.

$$\omega_{relax} = 2\frac{\sigma}{\varepsilon}\beta_{+}\frac{h\lambda_D}{L_s^{\,2}} \quad (5)$$

Here, all variables are as defined above. Using this equation the relaxation frequency of cations located on one half of the large electrode surface is calculated to be 200 Hz.

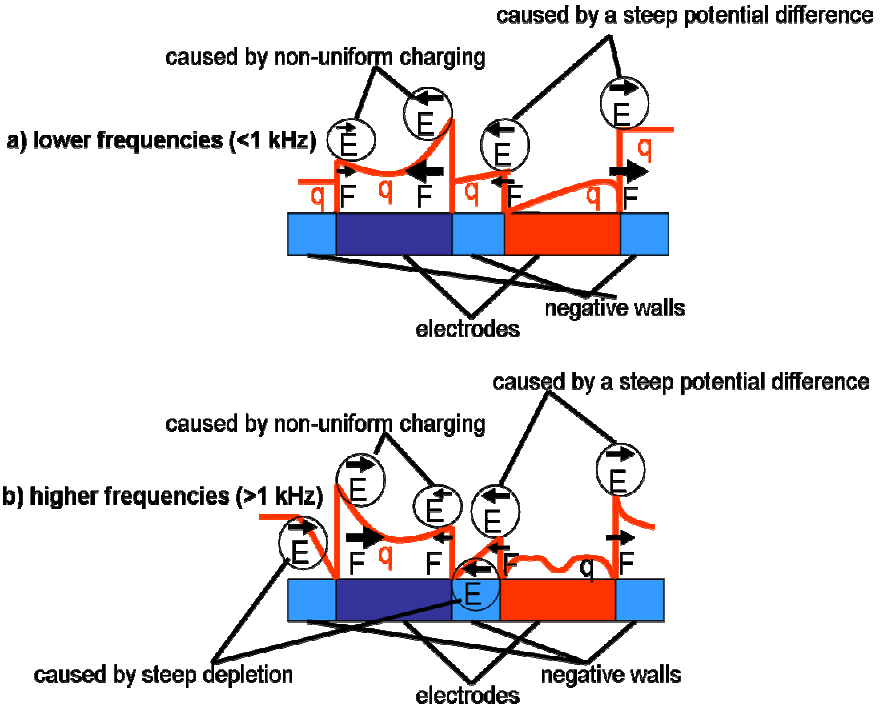

*Figure 5: Schematical representation of the mechanistic principles at work at different frequencies. For simplicity a **symmetric** system is chosen. a) At frequencies < 1kHz depletion effects do not play a significant role. On the negative electrode non-uniform charging causes E fields and generates flow in a way comparable to microchannel AC-EO. On the positive electrode the steep potential difference between the electrode and the wall causes local electric fields which in equilibrium follow a Debye decay of approximately 30 nm in the axial direction. During operation below 1kHz the asymmetric charge distribution above and around the large electrode causes flow away from the gap. Non uniform charging of the negative electrode only occurs for frequencies of 100 Hz and up, causing the effects on the positive and negative electrode to be dominant for frequencies below and beyond 100 Hz, respectively. b) At frequencies > 1kHz depletion effects do play a significant role. Since at these frequencies charge can only come from a small region next to the electrode, these regions get depleted. The cationic distribution in this depletion zone is steep causing an E-field on both sides of the negative electrode. Since the total amount of charge on the inner side of the negative electrode is bigger than on the outer side, the electrode is charged more on the outer than on the inner side. This in combination with the non-uniform charging generates flow in a way comparable to microchannel AC-EO, but reversed.*

5.2.2.2 Coupled ionic charging and hydrodynamics in nanochannels

The analysis up till now mainly considered the dynamical behavior of *ions* in the system. However, in the numerical analysis (see section 4) it was found that the dynamical behavior of the liquid, although caused by the ions in the system, adds a layer of complexity to the pumping behavior. Two flow directions occurred, at intermediate frequencies (~100-1000 Hz): the direction observed in microchannels and at low (<100 Hz) and high (>1000 Hz) frequencies a reversed direction. The behavior at lower frequencies will be further referred to as the **D**ebye **E**lectrode **E**dge **E**ffect (**DEEE**); the behavior at the intermediate frequencies as the **C**lassical **N**on-uniform **C**harging **E**ffect (**CNCE**); and the high frequency behavior as the **D**epleted **N**on-uniform **C**harging **E**ffect (**DNCE**). The mechanistic principles giving rise to this complex behavior for a device with symmetrical electrodes are given in figure 5. The behavior discussed here forms the essence of the numerical simulation results, which are discussed in more detail in section 4 of this chapter.

Lower frequencies (f<1kHz)

The top picture in figure 5 shows two pumping mechanisms that occur simultaneously at frequencies below 1kHz: a mechanism based on non-uniform charging which is identical to the one observed in AC EO in microchannels (left-hand side above the negative electrode) and a mechanism based on the forces exerted in the high electrical field at the electrode edges (right-hand side above the positive electrode). The first mechanism dominates between 100 Hz and 1 kHz and the second mechanism below 100 Hz. They will now be discussed separately, but always occur simultaneously and lead to pumping in opposite directions depending on the frequency.

Low Frequencies (f<100 Hz) (DEEE)

For low frequencies (<100 Hz) the ions are uniformly distributed on the electrode surface thus reducing the pumping mechanism as observed in microchannels to zero. Another pumping mechanism however occurs at the electrode edges, which is caused by the steep axial variation in potential between the electrode and the wall surface (which in equilibrium follows a Debye decay of approximately 30 nm). Since the glass walls at neutral pH have a negative potential which is in the same order as the applied potential, this axial potential variation and, therefore, the axial electric fields at the electrode edges are larger when an electrode is positive. This mechanism is dominant at these frequencies causing the largest force to be applied at the positive electrode directed from the electrode towards the wall surface. Since the system is driven using periodic signals, in the second half of the period a force in the opposite direction will occur at the other electrode. For a system with symmetric electrodes (as depicted in figure 5) this will cause a pulsating flow without a net direction. For a system with asymmetric electrodes, however, the effect in simulations (see later in this chapter) proofs to be more pronounced on a small electrode than on a large electrode because of the higher charge density on the small electrode than on the large electrode. This gives directionality to the flow in a fundamentally different

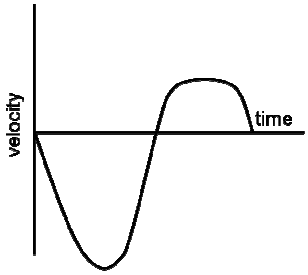

way than in microchannels, since here the directionality is caused by an asymmetry in electrokinetics and not in hydrodynamics as in microchannels. As a result a larger momentum is applied to the liquid in the half of the period where the small electrode is positive. This causes a pulsatile flow with a net direction from the large towards the small electrode. This direction is defined as negative (see the figure on the right), since it is opposite to the AC-EO direction in microchannels.

Intermediate frequencies (100 Hz<f<1 kHz) (CNCE)

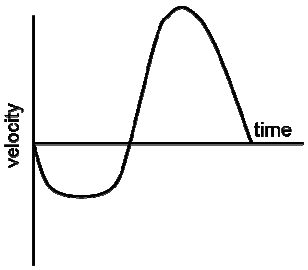

For an applied frequency beyond 100 Hz the electrodes start to be non-uniformly charged. This causes the pumping effect which dominates in AC EO in microchannels (the 'classical effect'). As can be seen in figure 5, the direction of the force is now opposite to the case described for a driving frequency below 100 Hz. However, since the applied signal is periodic and the effect only occurs at the negative electrode, the induced flow is again pulsatile. Furthermore, we found in the simulations (presented in more detail in section 4 of this chapter) that the effect that was described for frequencies below 100 Hz still occurs, but now less dominantly. If the electrodes are of unequal size, the CNCE limits the DEEE especially when the larger electrode is negative and not so much when the smaller electrode is negative. This is because the CNCE in the simulations appears to be most pronounced at the large electrode where the Coulomb force acts on a longer column of liquid, thereby applying a larger momentum on the liquid than at the small electrode. The directionality in this effect just as in microchannels has a hydrodynamic cause, however, without the liquid rolls. This causes the larger momentum to be applied during the half period where the large electrode is negative and causes a pulsatile flow with net direction from the small towards the large electrode which is defined as positive (figure on the right).

High frequencies (f>1 kHz) (DNCE)

For an applied frequency beyond 1 kHz, large fields are generated in a short time so that shielding charges can only be supplied towards the electrode surface from a very short distance, which causes steep depletion regions next to the negative electrode. This steep change in cationic concentration causes strong electric fields on both sides of the electrode, which are of the same order of magnitude as the other axial fields in the system. In combination with diffusion, these fields mediate the supply of cations towards the negative electrode surface. However, at the inner side the amount of charge at the start of a period is slightly lower than at the outer side, because during the previous period the other electrode attracted these charges via both diffusion and migration (via the above mentioned induced sharp concentration gradient and electric field). Moreover, at this field strength the distance traveled by ions by migration in one half period is less than one μm, which makes attraction at this

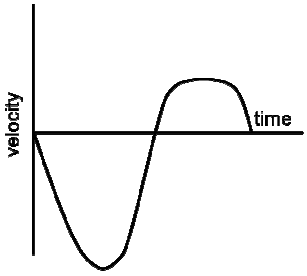

frequency from the previously accumulated charge on the other electrode impossible. This causes the negative electrode to be more charged above the outer side of the electrode than above the inner and the resulting direction of the induced flow is opposite to the classical case. Again if electrode asymmetry is added the effect theoretically appears to be most dominant on the large electrode for reasons described above in the intermediate frequency case. Therefore, also at high frequencies the directionality is caused by an asymmetry in hydrodynamics, making the DNCE fundamentally a hydrodynamic one. Again the larger momentum is applied during the half period where the large electrode is negative and causes a pulsatile flow with a net direction form the large towards the small electrode that is defined as negative (figure on the right).

Applied potential

Besides the complex frequency behavior device operation in nanochannels with double layer overlap differs from that in microchannels by a difference in dependency on applied potential. Whereas in microchannels the induced velocity is dependent on the applied potential squared, in nanochannels, theoretically, this behavior is not shown. From simulation data it was found that the velocity saturates for applied potentials higher than 300 mV. This behavior is caused by the limited availability of charge in the system because of the strong confinement in height, and differs strongly from the behavior in microchannels, where the supply of charge from the bulk is almost infinite. As a result not only the induced fields increase linearly as a function applied potential, but also the induced net charge, leading to the observed dependence on the voltage squared. Since at the moment there is only one calculated potential beyond 300 mV it is unclear if behavior in the nanochannel case is linear for potentials of 300 mV and up, which is expected since the electric field grows linearly with the applied potential.

5.3 Mathematical model

In this section the mathematical model which we used for simulating the device behavior is treated. For this simulation we consider a 50 nm high and 48 μm long slit-shaped nanochannel with two integrated asymmetric electrode pairs. The distance between two electrodes of a simulated pair, S_s, is 2 μm; the distance between two pairs, S_b, is 8 μm; the width of the small electrode, L_s, is 2.6 μm and the width of the large electrode is 11.4 μm. In figure 6 the geometry is depicted schematically.

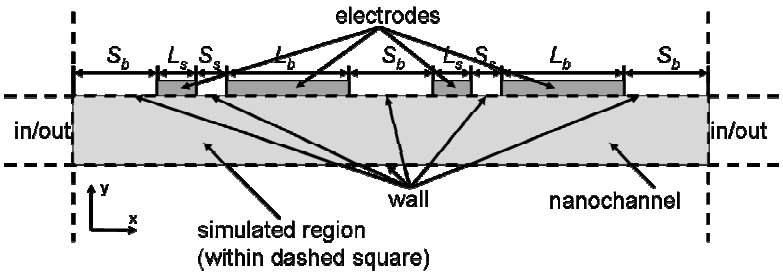

Figure 6: Schematic of the simulated geometry showing all important parts for the simulation.

Since a slit nanochannel is considered here, the width of the channel is much larger than its height (the channel width is 5 μm so the channel is 100 times wider than it is high). Therefore, we assume that the variables of interest do not vary dominantly in the lateral direction and neglect these. As a coordinate system, therefore, a two-dimensional Cartesian system (x,y) is chosen, with the x- and y-axes defined parallel and perpendicular to the length axis of the nanochannel as depicted in figure 6. Furthermore we assume that the walls have a constant wall potential. On the electrodes a variable sinusoidal AC potential is imposed without a DC offset potential. The channel entrance and exit, indicated in figure 6 as in/out, are either closed or set at a so-called convective flux boundary condition. The first condition is used to calculate the initial values, whereas the second condition is used during operation. When the initial values are calculated the system is assumed to be in equilibrium and convection is assumed to be zero. This equates the problem to a numerical computation of the full Poisson-Boltzmann solution. The convective-flux condition represents operation of the device far away from reservoirs and assumes that subsequent electrode pairs only influence one and another by convection and not by migration and diffusion.

For the simulations COMSOL MULTIPHYSICS v.3.4 is used. The software ran on an UNIX driven Pentium IV quad core with four 2.6 GHz cores with 8 GB of internal memory. Our model is defined as a time-variant multiphysics problem. To calculate the potential distribution as a function of space charge the Poisson equation is applied. Mass transport as a function of diffusion, migration and convection is described by the Nernst-Planck equations with a dynamic continuity equation. Finally, fluid motion is assessed by the Stokes equations for incompressible flow. All equations are simultaneously solved numerically by coupling them. The Poisson (P) and the Nernst-Planck (NP) equations are coupled via the concentration distribution obtained by solving the NP equations and the potential distribution obtained by simultaneously solving the P equation, respectively. Furthermore, the Stokes equations are coupled to the coupled Poisson-Nernst-Planck (PNP) equation set by using the potential and concentration distribution as input parameters for the force term in the Stokes equations and taking the result in terms of velocity to obtain the convective contribution to the ionic transport. In the following all governing equations are introduced and applied boundary conditions will be discussed.

5.3.1 Governing equations

In this section the equations that describe the device behavior used in the simulations are given. As mentioned in the introduction of this section ionic transport is based on the Nernst-Planck equation to describe concentration distributions by considering transport. Ionic flux, $\mathbf{J}_{\pm}$ [mol.m^{-2}.s^{-1}] is used to describe ionic transport. Since, we consider a two-dimensional system $\mathbf{J}_{\pm}$ is a vector defined in the x and y direction.

$$\mathbf{J}_{+} = -D_{+}\nabla c_{+} - z_{+}F\frac{D_{+}}{RT}c_{+}\nabla\psi + c_{+}\mathbf{u} \qquad (6)$$

$$\mathbf{J}_{-} = -D_{-}\nabla c_{-} - z_{-}F\frac{D_{-}}{RT}c_{-}\nabla\psi + c_{-}\mathbf{u}$$

Here, ∇ [m^{-1}] represent the gradient operator and is defined in the x and y direction; $c_{\pm}$ [$mol.m^{-3}$] is the molar concentration of positive and negative ions; ψ [V] is the electric potential; **u** [$m.s^{-1}$] is the velocity vector and can be split up in u [$m.s^{-1}$] and v [$m.s^{-1}$] which represent the velocity vectors in the x and y direction, respectively; $D_{\pm}$ [$m^2.s^{-1}$] represents the diffusion constant for positive and negative ions; $z_{\pm}$ [.] represents the ionic valences; F [$C.mol^{-1}$] is the Faraday constant; R [$J.K^{-1}.mol^{-1}$] is the universal gas constant and T [K] the absolute temperature. Since the phenomena we wish to study will generally not be in equilibrium a dynamical continuity equation is applied.

$$\nabla \cdot \mathbf{J}_{\pm} = -\frac{\delta c_{\pm}}{\partial t} \tag{7}$$

Here, t [s] represents time. The set of equations 6 - 7 contains four unknowns namely the concentrations of positive and negative ions, the electric potential and the linear velocity. The electric potential is as already mentioned calculated by the Poisson equation.

$$-\varepsilon \nabla^2 \psi = F(z_+ c_+ + z_- c_-) \tag{8}$$

Here ε [$F.m^{-1}$] represents the permittivity of the electrolyte. The linear velocity, **u,** is as mentioned above described by the Stokes equations for incompressible flow.

$$-\nabla p + \eta \nabla^2 \mathbf{u} - F(z_+ c_+ + z_- c_-)\frac{\partial \psi}{\partial x} = 0$$

and (9)

$$\nabla \cdot \mathbf{u} = 0$$

Here, p [Pa] represents the pressure and η [Pa.s] the viscosity of the electrolyte. The electrical field can have a component in the y-direction, and as a consequence forces can also be directed in the y-direction. Although forces applied in the y direction may have an effect on pumping they are not taken into account because of computational capacity limitations. Furthermore, as a continuity equation we assume that the electrolyte is incompressible, hence the linear velocity directed inwards any volume equals its linear velocity outwards. This in other words states that the mass density in any volume is constant in time. Finally, to limit the need for computational capacity, liquid flow is calculated by a first order approximation, meaning that we assume that between neighboring finite elements flow velocity only varies linearly. This approximation is allowed if the finite elements are small enough to adequately represent the problem. This was tested by decreasing the finite element size until variation in resulting flow velocity had saturated. To further keep within the limits of computational capacity finite elements at positions in the system where strongly varying variables had to be calculated (i.e. close to the walls and at the electrode edges) were minimized at the cost of a larger element size at positions where weakly varying

variables had to be calculated (i.e. in the center of the channel and in the center of the electrodes).

5.3.2 Boundary conditions

To solve the governing equations a set of boundary conditions is necessary. In the following, boundary conditions for each set of equations will be chosen.

5.3.2.1 Walls

The walls are assumed to be electrically isolating, negatively charged and to have a zero velocity at the interface with the liquid (no-slip conditions). This amounts to the following boundary conditions. The ionic current density normal to the wall surface is zero:

$$\mathbf{n} \cdot \mathbf{J}_{\pm} = 0 \text{; for } y = 0 \text{ and } y = h \tag{10}$$

Here **n** is a unit vector normal to the wall surface and h is the channel height. The wall potential of the electrodeless wall is set to -100 mV .

$$\psi = -0.1 \text{; for } y = h \tag{11}$$

The potential for the wall with electrodes is set to -121 mV which decays to -100 mV in 0.5 nm across a purely dielectric layer with a dielectric constant of 11. This layer is defined after Bard and Faulkner [14] and is named the Stern layer. Since it is a purely dielectric layer, the amount of mobile charge in this layer is assumed to be zero, this implicitly results in neglecting the conductivity of the Stern layer.

$$\psi = -0.121; \text{ for } y = 0 \tag{12}$$

The no-slip boundary condition for the Stokes equations is setup as follows:

$$u = 0 \text{; for } y = 0 \text{ and } y = h \tag{13}$$

5.3.2.2 Electrodes

For the electrodes just as for the walls an electrically isolating interface is assumed (equation 10). Furthermore, the electrode potential fluctuates described by a sinusoid. The electrode potential is given by

$$\psi = A \sin\left(2\pi f t + \varphi\right) + B \text{; for } y = 0 \text{ and } y = h \tag{14}$$

Here, A [V] and f [Hz] represent the amplitude and frequency of the sinusoid, respectively, φ [rad] is a phase shift with respect to an original sinusoid and is set to π on one of the electrodes of a pair, and B [V] is a DC offset, which is usually set to zero. A zero velocity is assumed at the electrode surface just as for the walls (equation 13).

5.3.2.3 Entrance/exit

Finally, the behavior at the entrance and exit of the device should be defined. As mentioned above for the Nernst-Planck equation, the migration and diffusion contribution to the flux normal to the entrance and exit of the channel are set to zero, resulting in a solely convective contribution to the ionic density across this interface.

$$\mathbf{n} \cdot \mathbf{J}_{\pm} = c_{\pm}\mathbf{u}\,;\ \text{for}\ x = 0\ \text{and}\ x = L \tag{15}$$

Here L is the channel length. Since migration is assumed to be zero normal to the interface, the electric field in the x- direction should be zero.

$$\frac{\partial \psi}{\partial x} = 0\,;\ \text{for}\ x = 0\ \text{and}\ x = L \tag{16}$$

For the Stokes equations a zero pressure gradient is applied by setting an equal normal force on both ends of the channel.

$$-p + \frac{\partial u}{\partial x} = p_0\,;\ \text{for}\ x = 0\ \text{and}\ x = L \tag{17}$$

Here p_0 [Pa] represents atmospheric pressure and equals 100 kPa.

5.4 Results and discussion

In this section simulation results will be presented and compared to the intuitive picture of the device behavior which was sketched in section 2. In figure 7 the simulated device behavior as a function of frequency for three different amplitudes of the applied sinusoidal potential is given. This simulation was performed at a KNO_3 electrolyte concentration in the reservoirs of 100 µM, corresponding to a λ_D of 30 nm bringing the 50 nm high device in the regime of overlapping electrical double layers.

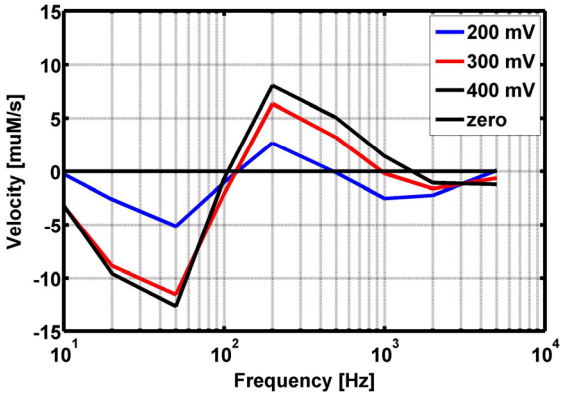

Figure 7: Simulated average velocity as a function of frequency for three different applied AC potentials at a reservoir concentration of 100 µM.

Using equation (4) of section 2 a lower frequency of ~10 Hz and a higher frequency of ~1000 Hz are found for the relaxation frequencies of negative and positive ions, respectively. The frequency below which cations start to uniformly distribute across the big electrode surface is calculated to be 200 Hz, which corresponds nicely to the positive velocity peak in figure 7, indicating the importance of the non-uniformity on the large electrode for this peak. Later in this section we will show that indeed theoretically the cations are non-uniformly distributed across the large electrode surface at 200 Hz. Since the behavior of the device is a superposition of the three effects that resulted from the simulations, the effect for each potential and frequency the relative importance of the two effects at different potentials and frequencies needs to be assessed. By looking at the net charge density and the concentration and (non-) uniform distribution of positive and negative ions for different frequencies (figure 8 and 9, respectively) one can see that our intuitive picture of section 2 of different relaxation frequencies for positive and negative frequencies is correct. Namely, while in the attraction phase at 50 Hz the cationic distribution is rather uniform, the anionic is not. For the higher frequencies it can be seen that both the anionic and cationic distribution are non-uniform, however the anionic concentration is decreased, especially on the small electrode.

The optimal driving frequencies do not exactly correspond to the values calculated with equation (4). The reason for this is that although both the novel and the classical effect exploit the different relaxation frequencies for positive and negative ions they do not have their optima exactly at these relaxation frequencies. In case of the spectrum shown in figure 7 the optima at the lowest frequency are typically caused by DEEE as is defined in section 2 of this chapter. Apparently in this case at 50 Hz the force asymmetry between the small electrode and the large electrode is at its maximum. This can also be seen by looking at the simulated values of the net charge and the electric field at 50 Hz (figure 10 and 11, respectively).

In these figures it can be seen that the electric field strength at the electrode edges is not so much influenced by the frequency, but that rather the asymmetry in concentration of net charge around these edges depends on the frequency and dictates a net flow direction. Since the difference between the amount of charge around the inner edge and around the outer edge is bigger at the small electrode than at the large electrode, the effect is most prominent on the small electrode and the flow will be pulsating with a net direction from the large towards the small electrode.

The second optimum in the spectra of figure 7 at 200 Hz can be attributed to the superposition of the DEEE and the CNCE as are defined in section 2 of this chapter. By looking at the net charge distribution and the electric fields in both half periods (figure 10 and 11, respectively) at this frequency, one interestingly can note that the DEEE still generates a considerable force on the liquid. The flow direction caused by the DEEE is however opposed to the CNCE as discussed qualitatively in section 2, and the CNCE is the largest at this frequency. This effect is especially pronounced in the second half period. The field strength generated above the electrodes is in the order of 10 $kV.m^{-1}$ and is slightly stronger above the inner side than above the outer side of the electrodes. Furthermore, on the large electrode the effect occurs over a longer length, thereby applying a force on a longer column length of liquid. The behavior described above cause a pulsating flow with a net direction from the small towards the large electrode.

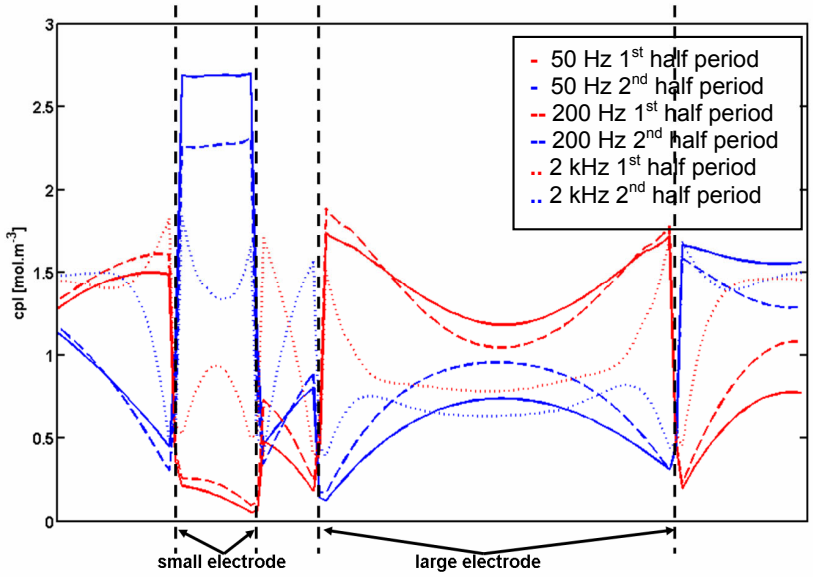

Figure 8: Average cationic concentration as a function of position above an electrode pair. The red and blue lines correspond to the values of maximum effect during the first and second half period, respectively. The full, dashed and dotted line correspond to 50, 200 and 2000 Hz, respectively. The reservoir concentration is 100 μM (double layer overlap).

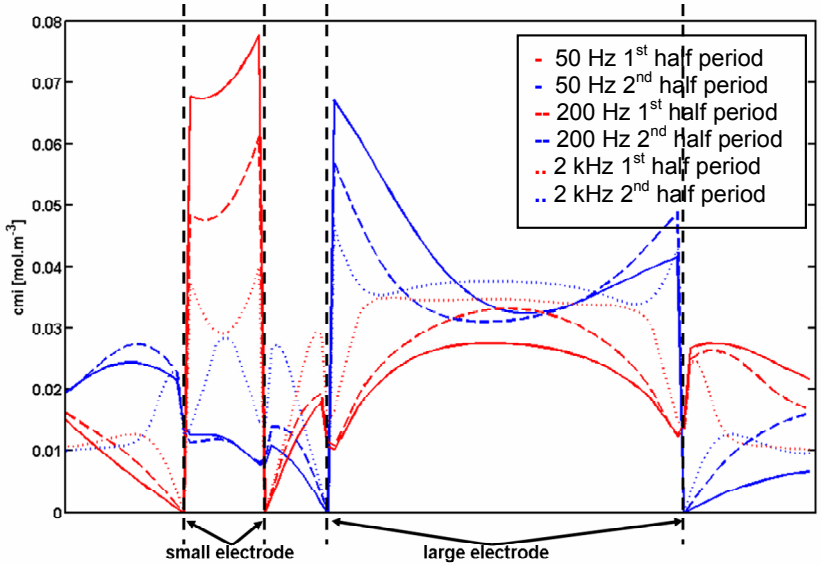

Figure 9: Average anionic concentration as function of axial position above an electrode pair. The red and blue lines correspond to the values of maximum effect during the first and second half period, respectively. The full, dashed and dotted line correspond to 50, 200 and 2000 Hz, respectively. The reservoir concentration is 100 μM (double layer overlap).

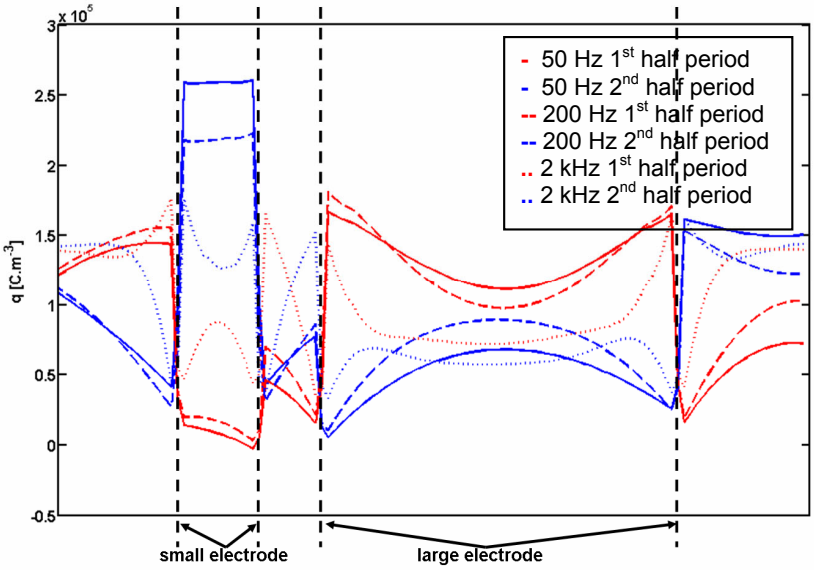

Figure 10: Average net charge, q, as a function of the axial position in the channel. The red and blue lines correspond to the values of maximum effect during the first and second half period, respectively. The full, dashed and dotted line correspond to 50, 200 and 2000 Hz, respectively. The reservoir concentration is 100 μM (double layer overlap).

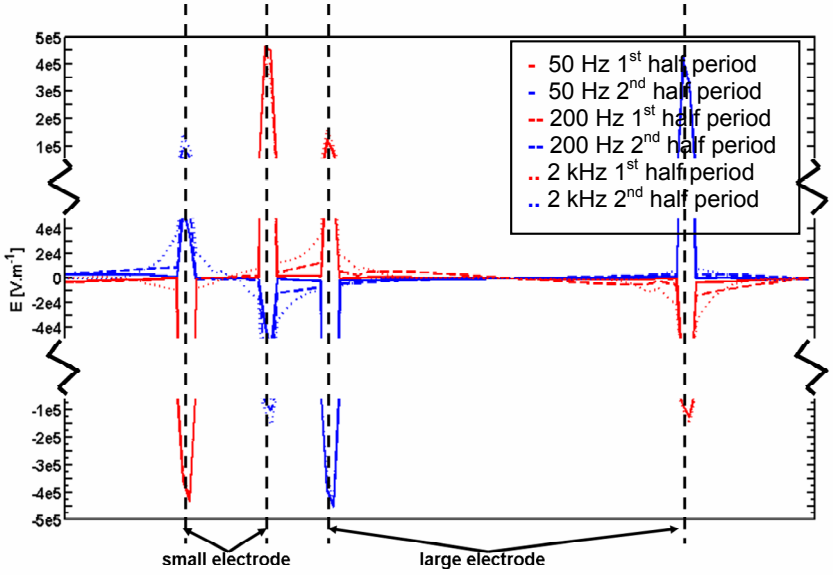

Figure 11: Average electric field, E, as a function of the axial position in the channel. The red and blue lines correspond to the values of maximum effect during the first and second half period, respectively. The full, dashed and dotted line correspond to 50, 200 and 2000 Hz, respectively. The reservoir concentration is 100 μM (double layer overlap).

At 2000 Hz the non-uniformity in the cationic distribution is very pronounced, which makes the CNCE as defined in section 2 of this chapter even stronger than at 200 Hz. Indeed 2000 Hz is quite close to the calculated relaxation frequency of positive ions. The flow direction at this frequency, however, is opposite to the CNCE direction, as can be seen in figure 7. This unexpected behavior is caused by the fact that at this high frequency charge can only be transported towards the electrode surface over a short distance, which causes steep depletion zones next to the electrodes as can be seen in figures 8 and 10. This depletion induces electric fields that are in the same order as the other induced fields and are approximately equal on both sides of the electrodes. However, at the inner edge the amount of charge at the start of a period is slightly lower than at the outer edge, because during the previous period the other electrode attracted these charges via both diffusion and migration (via the above mentioned induced sharp concentration gradient and electric field). Moreover, at this field strength the distance traveled by ions by migration in one half period is less than one μm, which

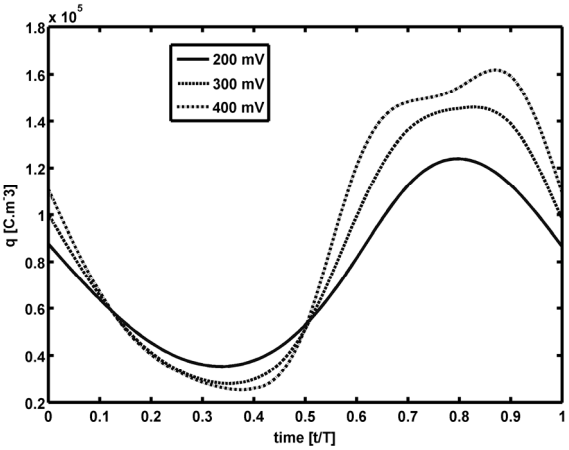

Figure 12: Total net charge above a small electrode as a function of time for different applied AC potentials.

makes attraction from the previously accumulated charge on the other electrode impossible within the time span of half a period. This causes the negative electrode to be more charged above the outer side than above the inner. This behavior is opposite to the CNCE and is referred to as DNCE, where the electrodes charge more strongly above the inner side of the electrode because of a higher field strength at these positions and enough time to transport from one electrode to the other. Therefore, around 2000 Hz the flow is again pulsating, with a non-classical net direction.

Another important property seen in figure 7 is a negative change in velocity dependency on applied potential beyond 300 mV. This is in clear contrast to the potential-velocity relationship in microchannels where the velocity is proportional to the applied voltage squared. The velocity dependence in microchannels is caused by a simultaneous linear increase in induced electric field strength and a linear increase in induced net charge causing an approximate quadratic increase in applied body force for increasing applied potential. In nanochannels with thick or overlapping electric double

layers a limited availability of ions causes a saturation in induced net charge as can be clearly seen in figure 12. In microchannels depletion does not occur due to the practically unlimited electroneutral bulk. Since only one potential beyond 300 mV is simulated it is unclear if the dependency of the velocity on applied potential goes from squared to linear as is expected theoretically.

Finally the influence of the extent of double layer overlap is assessed by simulating the same device at a virtual reservoir concentration of 1 mM KNO_3 of which the results are given in figure 13. At a reservoir concentration of 1 mM the Debye length is ~10 nm long, so that double layers although considered do not strongly overlap.

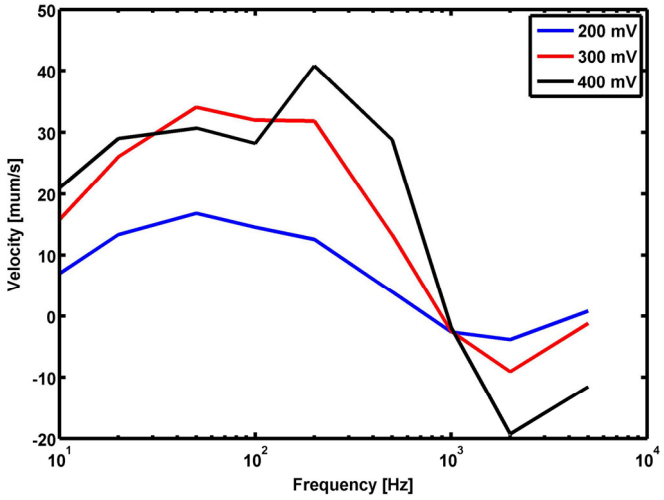

Figure 13: Simulated velocity as a function of frequency for three different applied AC potentials at a reservoir concentration of 1 mM

Interestingly in this case the velocity appears to be positive (i.e. corresponding to the classical direction of flow) up to approximately 1 kHz. This shows that the DEEE predicted at low frequencies only dominantly occurs in the case of strong double layer overlap. The relaxation frequencies calculated with equation (4) for NO_3^- and K^+ now are 60 and 800 Hz, respectively. The frequency below which cations on the large electrode start to uniformly distribute is in this case also around 200 Hz, which more or less corresponds to the positive velocity peak in figure 13.

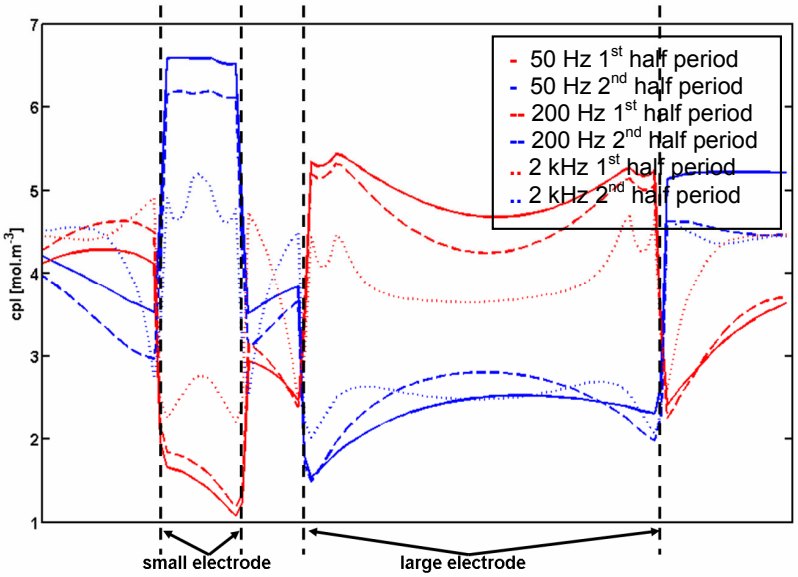

Figure 14: Average cationic concentration as a function of position above an electrode pair. The red and blue lines correspond to the values of maximum effect during the first and second half period, respectively. The full, dashed and dotted line correspond to 50, 200 and 2000 Hz, respectively. The reservoir concentration is 1 mM (thick double layers but no overlap).

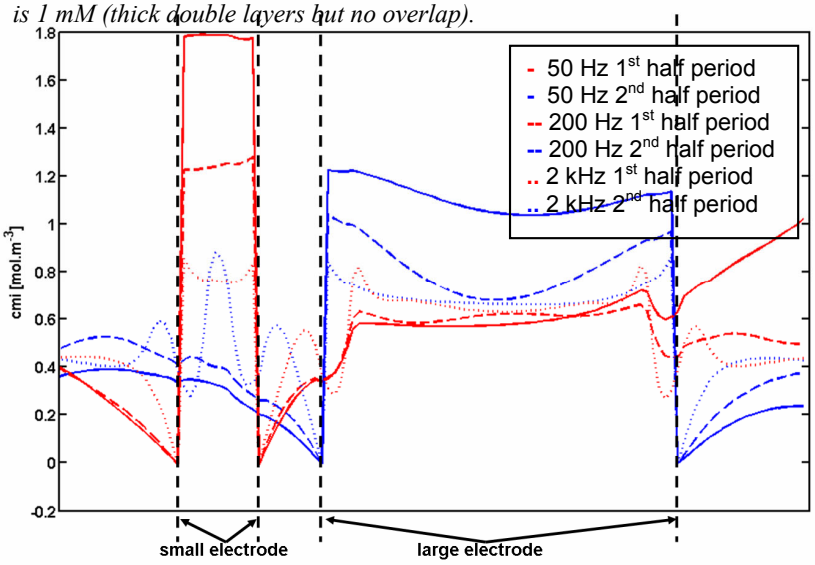

Figure 15: Average anionic concentration as a function of position above an electrode pair. The red and blue lines correspond to the values of maximum effect during the first and second half period, respectively. The full, dashed and dotted line correspond to 50, 200 and 2000 Hz, respectively. The reservoir concentration is 1 mM (thick double layers but no overlap).

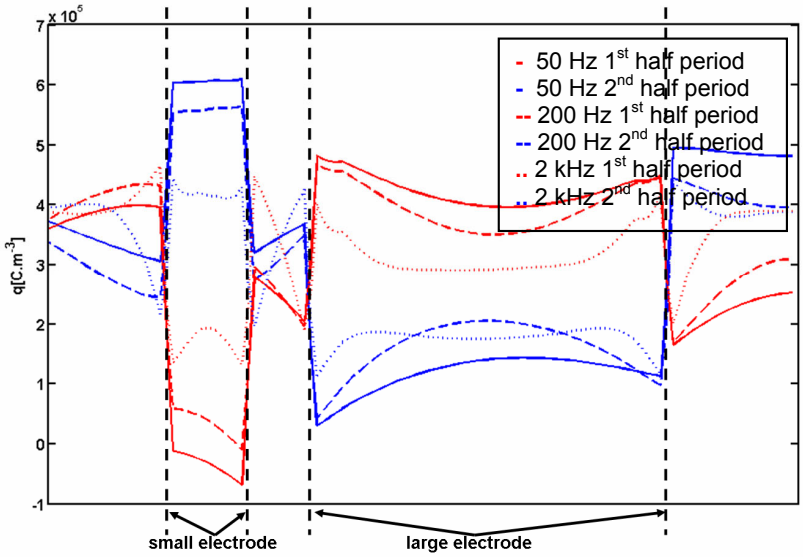

Figure 16: Average net charge concentration, q, as a function of position above an electrode pair. The red and blue lines correspond to the values of maximum effect during the first and second half period, respectively. The full, dashed and dotted line correspond to 50, 200 and 2000 Hz, respectively. The reservoir concentration is 1 mM (thick double layers but no overlap).

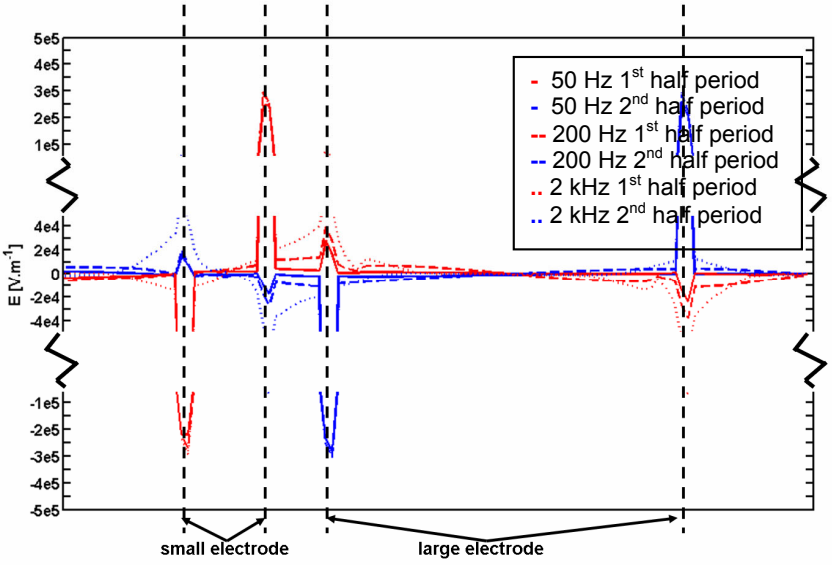

Figure 17: Average electric field, E, as a function of position above an electrode pair. The red and blue lines correspond to the values of maximum effect during the first and second half period, respectively. The full, dashed and dotted line correspond to 50, 200 and 2000 Hz, respectively. The reservoir concentration is 1 mM (thick double layers but no overlap).

Looking both at the cationic and anionic distributions (figures 14 and 15) it can be seen that both concentrations have on average increased. Furthermore, although the double layers no longer overlap at this reservoir concentration still the amount of cations is larger than the amount of anions.

The mechanism can be understood in more detail by inspecting q and E in figures 16 and 17, respectively. At 50 Hz on both electrodes again the concentration of net charge near the outer edge is larger than on the inner edge. However, the difference in q around the inner and outer edges is approximately the same for both the small and the large electrode. This means that the novel effect still occurs at this reservoir concentration, however, does not have a net component. The CNCE as defined in section 2 of this chapter already operates at this frequency and now that it is not dominated by the DEEE already at this low frequency determines the flow. This results in a pulsating flow with a net direction from the small towards the large electrode which is the same direction as was classically observed in microchannels.

At 200 Hz the CNCE reaches a maximum as was approximately predicted by equation (5) and can be seen by inspecting the non-uniform ionic distributions in figure 14 and 15 and the electric field in figure 17. The CNCE is in the case of thick double layer stronger than in the case of overlapping double layers since the concentration of net charge is approximately 3 times larger (e.g. compare figure 10 and 16) which more or less corresponds to the increase in velocity predicted at the low and intermediate frequencies.

At high frequencies (around 2 kHz) and 1 mM reservoir salt concentration, the reversed effect which is dominated by depletion (DNCE as defined in section 2 of this chapter) takes over, as in the case of 100 μM reservoir salt concentration. This can again be understood by observing the larger concentration of positive charge above the outer sides of both electrodes as compared to above the inner sides and also by observing the steep depletion zones of cationic concentration next to the electrodes.

A final typical characteristic of the spectrum in figure 13 is that just as in the case of double layer overlap, a change in velocity as a function of applied AC potential occurs. This is again caused by saturation in generated net charge, q, as can be seen in figure 18. Theoretically this should result in an approximate linear function of velocity on applied potential, but is as discussed in the 100 μM not yet theoretically proven by the numerical simulation. Furthermore, in the intermediate frequency regime the velocity at 400 mV applied potential appears to be smaller than at 300 mV. This is probably explained by depletion and can be seen in figure 18 where the concentration of charge on the inner edge of the large electrode in the first half period does not increase for an increase in applied potential from 300 to 400 mV while the concentration at the outer edge does. This makes the net effect smaller in case of the 400 mV applied potential, since the forces on both edges of the electrode are oppositely directed.

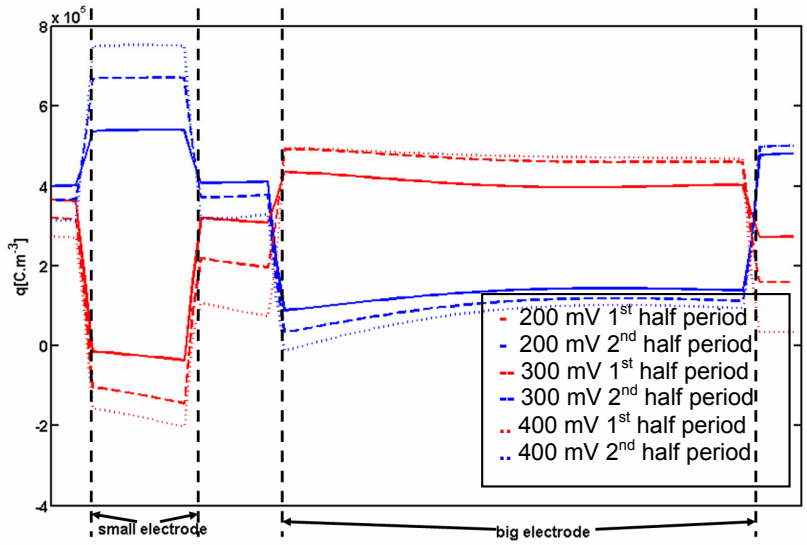

Figure 18: Average net charge concentration, q, as a function of position above an electrode pair at an applied frequency of 50 Hz. The red and blue lines correspond to the values of maximum effect during the first and second half period, respectively. The full, dashed and dotted line correspond to 200, 300 and 400 mV applied AC potential, respectively.

5.5 Conclusions

AC electro-osmotic flow induced at asymmetric electrodes integrated in a 50 nm high nanochannel is theoretically treated by numerical modeling using the finite element method. A pulsating flow with a net direction was predicted to occur when applying sinusoidal potential waves to the electrodes. Flow direction is predicted to be bi-directional, depending on applied frequency. The situation of both overlapping and thick double layers was simulated.

In the case of overlapping double layers (corresponding to a reservoir salt concentration of 100 μM) three optimal driving frequencies are found, showing both negative and positive (i.e. corresponding to the direction classically observed in microchannels) velocities. The optimal frequencies that are found are around 50 Hz, 200 Hz and 2 kHz, showing a negative, a positive and again a negative direction of flow, respectively.

In the case of thick but non-overlapping double layers (corresponding to a reservoir concentration of 1 mM) only two optimal driving frequencies are found, showing both positive and negative velocities. Optimal driving frequencies are determined around 100 Hz and 2 kHz, showing a positive and a negative direction of flow, respectively.

The induced flow velocity as a function of applied AC potential shows different scaling behavior beyond 300 mV. It appears to scale linearly, in contrast to classical behavior observed in microchannels where the velocity is approximately proportional to the applied AC potential squared.

References

1. Yuan, Z., et al., *Electrokinetic transport and separations in fluidic nanochannels.* Electrophoresis, 2007. **28**(4): p. 595-610.
2. Schoch, R.B., J.Y. Han, and P. Renaud, *Transport phenomena in nanofluidics.* Reviews of Modern Physics, 2008. **80**(3): p. 839-883.
3. Watson, J.D. and A. Berry, *DNA: The secret of life.* 2003. ISBN: 0-375-41546-7.
4. Pennathur, S. and J.G. Santiago, *Electrokinetic transport in nanochannels. 1. Theory.* Analytical Chemistry, 2005. **77**(21): p. 6772-6781.
5. Pennathur, S. and J.G. Santiago, *Electrokinetic transport in nanochannels. 2. Experiments.* Analytical Chemistry, 2005. **77**(21): p. 6782-6789.
6. Salieb-Beugelaar, G.B., et al., *Field-dependent DNA mobility in 20 nm high nanoslits.* Nano Letters, 2008. **8**(7): p. 1785-1790.
7. Karnik, R., et al., *Electrostatic control of ions and molecules in nanofluidic transistors.* Nano Letters, 2005. **5**(5): p. 943-948.
8. Gawad, S., L. Schild, and P. Renaud, *Micromachined impedance spectroscopy flow cytometer for cell analysis and particle sizing.* Lab on a Chip, 2001. **1**(1): p. 76-82.
9. Morgan, H., et al., *Single cell dielectric spectroscopy.* Journal of Physics D-Applied Physics, 2007. **40**(1): p. 61-70.
10. Prost, J., et al., *Asymmetric Pumping of Particles.* Physical Review Letters, 1994. **72**(16): p. 2652-2655.
11. Ramos, A., et al., *AC electric-field-induced fluid flow in microelectrodes.* Journal of Colloid and Interface Science, 1999. **217**(2): p. 420-422.
12. Olesen, L.H., H. Bruus, and A. Ajdari, *ac electrokinetic micropumps: The effect of geometrical confinement, Faradaic current injection, and nonlinear surface capacitance.* Physical Review E, 2006. **73**(5): p. -.
13. Plecis, A., R.B. Schoch, and P. Renaud, *Ionic transport phenomena in nanofluidics: Experimental and theoretical study of the exclusion-enrichment effect on a chip.* Nano Letters, 2005. **5**(6): p. 1147-1155.
14. Bard, A.J. and L.R. Faulkner, *Electrochemical methods : fundamentals and applications*. 2nd ed. 2001, New York: John Wiley. xxi, 833 p.

Chapter 6

Bi-directional Pumping in Nanochannels Using Integrated Asymmetric Electrode Arrays: Experiments

In this chapter we describe an experimental setup to determine the fluid flow velocity induced by asymmetric electrode arrays integrated into a 50 nm high nanochannel. The setup is built up and successfully employed. Theory explaining the employed measurement method is described and compared to the experimental results. Two chips with different electrode sizes and spacings are experimentally tested on their ability to generate flow inside a nanochannel with overlapping electrical double layers, by applying a low voltage AC potential to the asymmetric electrode array. The measured velocities as a function of frequency show a qualitatively comparable trend as the calculated velocities in chapter 5. A bi-directional flow is observed, with both a classical flow direction and an opposite flow direction, depending on the applied frequency. Theory in chapter 5 had already predicted these opposing flow velocities. At applied potentials of 400 mV a maximum velocity of 6 μm/s was found in the classical direction and of 8 μm/s in the opposite direction.

6.1 Introduction

Electrokinetic generation of transport in micro- and nanofluidic channels is largely performed by applying DC electric fields along such channels [1-3]. If liquid transport is involved this method is generally referred to as DC electro-osmosis. The disadvantage of doing so is that the necessary voltage for a given flow is a linear function of channel length. This results in high applied voltages and therefore necessary safety precautions for long channels. A method presented in literature where velocity does not scale with channel length is AC electro-osmosis [4-7]. Here, liquid flow is induced by applying a sinusoidal potential wave to an array of electrodes that is integrated in one or more of the channel walls. To obtain a net directive flow asymmetry is introduced either in time as in traveling wave electro-osmosis [8] or in space by fabricating an asymmetric electrode array [4,7]. The latter method will be considered here implemented in a nanochannel with overlapping double layers.

This chapter presents an AC electro-osmotic pump that consists of a one-dimensional 50 nm high nanochannel with an integrated asymmetric micro-electrode array. Since the device fundamentally transports ions, we will further refer to it as an ion pump. The device is able to pump ions by applying low (< 1 Vpp) AC voltages to the electrode array. The liquid flow resulting from this by viscous coupling is measured by the current monitoring technique; which here differs form the original technique introduced by Huang et al. [9] since here the conductivity is measured locally inside the channel instead of only at both ends of the channel. This has the advantage of an amplified current as compared to the original method, where the measured current tends to be small. To apply this technique, liquids of different electrical conductivity are introduced to both channel ends after initial equilibration. Following engagement of the pump, a change in complex current between the electrode pairs is a measure of liquid velocity. In fact, the length of the channel divided by the time it takes for the conductivity to go from the initial value to a new constant value corresponding to the newly introduced liquid is a measure of the time and space averaged velocity of the liquid.

The theoretical treatment of chapter 5 predicted that the operation in nanochannels with overlapping electrical double layers would be different from that in microchannels with thin double layers. Multiple characteristic frequencies were predicted in nanochannels instead of one. The experiments presented in this chapter confirm these theoretical predictions.

The chapter is organized as follows. First theory, especially concerning flow detection is treated. Secondly, an experimental section is presented where details about both the device and the setup are given. In the following section the experimental results are presented and compared to theory. Finally some conclusions will be drawn.

6.2 Theory

In this section theory necessary to interpret and discuss the experimental results is presented.

6.2.1 Modeling of device behavior

Device behavior was described using finite element simulations. The implementation and results of these simulations are thoroughly explained in chapter 5 of this thesis, where, moreover, an intuitive picture of the operation principles was derived from the model. This model was based on a slightly different geometry than the ones on which the experiments were performed in this chapter. In detail, the small and the large electrode are 2.6 μm and 11.4 μm, respectively; the small and the large gap are 2 μm and 8 μm, respectively. It is not expected that this small difference leads to fundamentally different results.

6.2.2 Impedance measurement with integrated electrodes in nanochannels

As already stated in the introduction, the induced flow is determined by measuring the change in current between electrode pairs in the integrated array when liquid of a different conductance gradually replaces the original liquid in the channel. This current results from the application of the same sinusoidal potential wave between the electrode pairs that causes the liquid pumping and is measured using an impedance analyzer. In this section the theory behind such measurements will be described, to enable proper understanding and the interpretation of the measurement results.

The electrical impedance of an electrolytic solution measured by metal electrodes in contact with it, is strongly frequency dependent. In this subsection the origins of this frequency dependency will be explained by using the equivalent circuit given in figure 1. More detailed information on the impedance of electrolytes at electrodes can be found in textbooks such as [10]. Olthuis et al. both experimentally and theoretically determine the impedance cell constant of micromachined interdigitated electrodes [11], whereas examples of applications of impandance measurements with such devices can be found for example in [12,13].

The equivalent circuit given in figure 1 is a simplified one, where the resistance and inductance of the leads and the transfer resistance to describe Faradaic currents at the electrode/liquid interface are not taken into account. The first simplification is allowed since for systems with high impedance, the resistance and inductance of the leads can be neglected for frequencies below 1 MHz (which is well within the operating regime). This high impedance will, however, make the measurement more sensitive to the parasitic capacitance which will be treated later in this section. The second simplification means that the charge transfer between the electrode and the electrolyte is neglected and therefore assumes that electrical communication between the electrodes and the electrolyte is purely capacitive. This is allowed for potentials (far) below the electrolysis potential of water (~1 V) and not too low frequencies as

will be shown in section 6.4. A simple linear equation to calculate R_{el} [Ω] is given in equation 1.

$$R_{el} = \frac{d}{A}\frac{1}{\sigma} \tag{1}$$

Here, d is the distance between an electrode pair and A is the cross-sectional area of the nanochannel (height times width) and σ [S.m^{-1}] is the conductivity of the solution. As can be seen from equation 1 R_{el} is dependent on the geometry and size of the electrodes and the channels. Also, R_{el} is influenced by the conductivity of the solution inside the nanochannel and therefore a function of the electrolyte strength inside the reservoirs and moreover strongly influenced by the amount of double layer overlap as is discussed

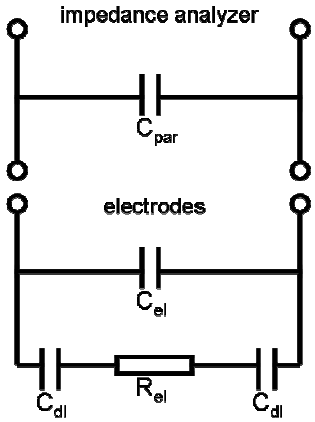

Figure 1: Simplified equivalent circuit to describe the complex impedance between electrode pairs inside electrolytic solutions. C_{par} [F], C_{el} [F], C_{dl} [F] and R_{el} [Ω] represent the total parasitic capacitance in the circuit, the capacitance of the liquid, the double layer capacitance and the resistance of the electrolyte, respectively.

in chapter 5. Apart from the conductivity contribution of the electrolyte salt ions, another source of conductivity derives from the protons inside the electrolyte. These protons stem from the electrolyte solution in the reservoirs which magnitude is amplified inside the channel because of double layer overlap and thus cationic enrichment.

According to Stein and coworkers [14] Stern layer conductance is an important contribution to the total axial conduction in nanochannels that becomes increasingly important for decreasing electrolyte strength.

Another important parameter in determining the impedance is the differential double layer capacitance, C_{dl}, which is given by

$$C_{dl} = A\frac{C_{Stern}C_{diff}}{C_{Stern}+C_{diff}}, \tag{2}$$

where A [m^2] is the surface area of the electrodes, C_{Stern} [$F.m^{-2}$] is the capacity of the Stern layer and the differential capacity C_{diff} is defined as [10]:

$$C_{diff} = \frac{\partial\sigma_0}{\partial\psi_0} = \sqrt{\frac{2z^2q^2\varepsilon_r\varepsilon_0N_l}{kT}\cosh\left(\frac{zq\psi_0}{2kT}\right)}, \tag{3}$$

where σ_0 [$C.m^{-2}$] ψ_0 [V] are the charge and the potential at the surface, respectively; z [.], q [C] and the product $\varepsilon_r\varepsilon_0$ [$F.m^{-1}$] are the ionic valance, the elementary charge and the electrical permittivity of in this case water, respectively; N_l [m^{-3}] is the amount of ions per cubic meter; k [$J.K^{-1}$] is Boltzmann's constant and T [K] is the absolute temperature. For the surface area of the electrodes we will take that of the small electrode, since the small one will be dominant over the bigger one in the series circuit at hand here.

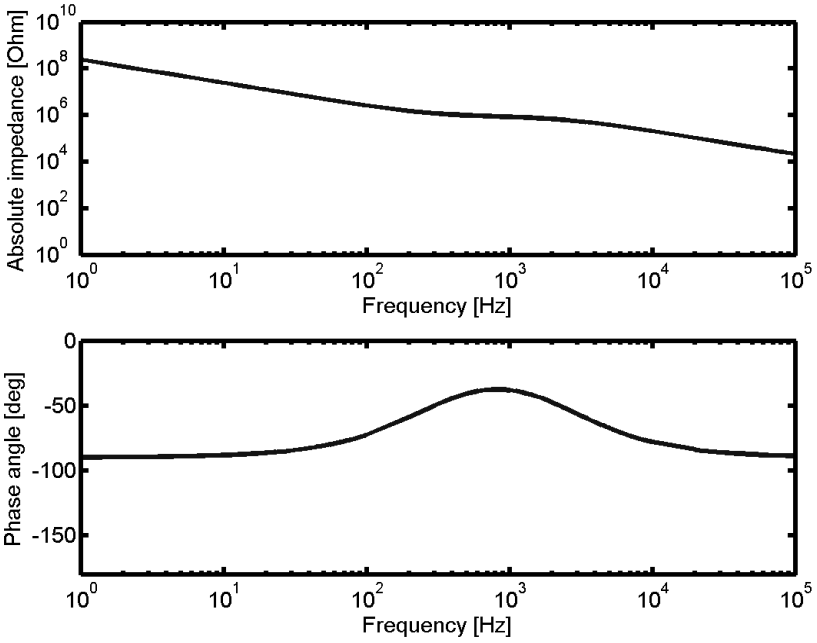

Figure 2: Ideal calculated impedance plot for a 50 nm high and 5 μm wide channel with the following electrode specifications: number of electrode pairs: 203; size of the small electrode 2.6 μm; size of the large electrode 8.6 μm; size of the small gap 1.4 μm; size of the large gap: 9.4 μm. The electrolyte concentration is 100 μM and ion enrichment/exclusion is taken into account using equation 3 of chapter 5.

The last important parameter is the combined capacitance of the solution and the parasitic capacitance. As discussed in chapter 3 this capacitance is dominated by the parasitic capacitance of the wiring and the impedance analyzer and therefore for the remains of this chapter the solution capacitance will be neglected.

In figure 2 an example of the ideal calculated impedance/frequency characteristic is given. The point where the optimum driving frequency is found according to literature (i.e. classical behavior known from microchannels without double layer overlap) is located close to the point where the phase angle of the impedance hits 45° for the first time (i.e. for increasing frequency). Increasing the conductivity of the solution shifts the plateau in the absolute impedance data downwards. This causes the optimum driving frequency to shift to the right. The opposite shift holds for a decrease in conductivity.

Finally for a better understanding of the experimental results other sources of ionic transport are considered; starting with convection induced by axial pressure differences, which may stem from deviations in pressure drop along the microchannels. Using the following equation to calculate the pressure drop, δP [Pa], across the microchannels we are able to assess the influence of pressure fluctuations across the microchannels on convection in the nanochannels [15]:

$$\partial P = Q\frac{\eta L_m}{9d^3}, \tag{4}$$

where, η [Pa.s] represents the viscosity of water, L_m [m] and d [m] represent the channel length and the channel diameter, respectively, and Q [$m^3.s^{-1}$] represents the volumetric flow rate. Equation 4 is only valid for square channels. Plugging δP into equation 5 gives the resulting linear flow velocity of ions, v [$m.s^{-1}$] in the system caused by a possible fluctuation in pressure difference along the nanochannels [15]:

$$v = \frac{\partial P h^3 w}{12\eta L_n} \tag{5}$$

where, h [m], w [m] and L_n [m] represent the channel height and width, respectively. During experiments Q does not exceed 300 nL/min. This results in a maximum velocity of ions in the nanochannel caused by a pressure difference of 1 nm/s which is negligible.

A second source of ionic transport is diffusion. Ions used during the experiments have a diffusion constant of approximately 2.10^{-9} $m^2.s^{-1}$. This gives ions an average velocity of approximately 2 μm/s for 4 mm long channels. This is clearly in the same order as the expected flow velocities induced by the electro-kinetic pump. However, the velocity is dependent on the position in the channel as shown in equation 6 that is derived from the Nernst-Plank equations without a convection and a migration term in it [16].

$$v_D(x) = \frac{D}{x} \tag{6}$$

Here, v_D [m.s^{-1}] is the velocity caused by diffusion, D [m^2.s^{-1}] is the diffusion constant and x [m] is the axial position in the nanochannel which gives a rate of arrival and thus a change in measured current that is a square root function of time as can be seen by deriving the velocity of ions as a function of time as is done in equation (7).

$$v_D(t) = \sqrt{\frac{D}{2t}} \tag{7}$$

This should, however, be clearly observable in the measured current as function of time traces.

6.3 Experimental

In this section both the device preparation prior to experiments and the experimental setup are described.

6.3.1 Device preparation

Layout and fabrication of both the nanochannel devices and the microchannel chips can be found in chapters 3 and 4 of this thesis. For clarity the device layout after all fabriacation steps is given in figure 3.

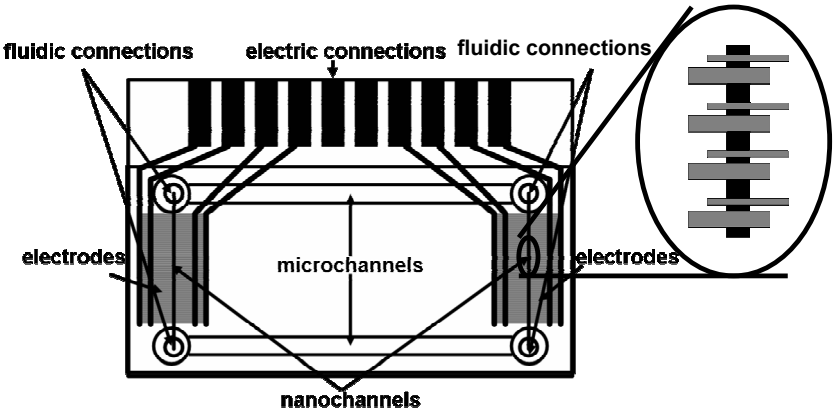

Figure 3: Device layout after all fabrication steps are performed. The important parts of the device are indicated including the external connection spots for both the electronics and fluidics.

Here only the preparation prior to experiments will be treated. Approximately a week before the experiments some final chip preparations are performed. In these final steps PDMS slabs containing microchannels are bonded to the glass chips containing the nanochannels, electrodes and electric connections. In this chapter the experimental

results obtained with two different electrode arrays are described. The dimensions of the devices are given in table 1.

Table 1: Electrode size and spacing for the chips used

chip	big electrode	small gap	small electrode	big gap
	[μm]	[μm]	[μm]	[μm]
82210	8.6	1.4	2.6	9.4
710225	7.6	9.4	2.6	24.4

The PDMS chips with microchannels are fabricated just prior to bonding. The reason for this is that PDMS kept in air will harden and become brittle in time. This causes a lower bond strength which potentially causes problems with leakage. After curing, the PDMS is peeled from the mold and cut into individual chips with a size matching the Pyrex chip containing the nanochannels and electrodes. Then holes are punctured in the PDMS using a 1 mm diameter perforator to create an entrance and an exit to and from the microchannels. Since this procedure causes loose PDMS particles near these ports which may clog the fluidic channels in a later stage, the PDMS slabs are ultrasonically cleaned in acetone. After this step the slabs are subsequently dipped in three DI baths and finally in an isopropanol bath. The glass part of the chip is not cleaned ultrasonically since this could destroy the electrode and nanochannel structures. Instead of the ultrasonic step the glass chips are rinsed with acetone and then the procedure equals that of the PDMS slabs. Both are dried for 15 minutes in an oven at 60°C. After drying the glass chips and the PDMS slabs are cleaned in an air plasma cleaner (Harrick Air Plasma Cleaner/Sterilizer) for 4 minutes. The plasma power is set to 29.6 W (which is the maximum for this cleaner) and the pressure is set to approximately 0.5 mBar. Subsequently a drop of methanol (Sigma Aldrich 99.93%) is placed on the glass channel. This will delay the bonding process and will enable alignment of the PDMS slabs with the glass chip. The methanol is allowed to evaporate in a desiccator for at least 6 hours. Methanol evaporation is performed in a desiccator to have a clean and controlled environment during bonding. This is important both for bonding and to prevent clogging of the device during later steps. After this the microchannels are filled with a chromium etchant (Merck) and in approximately 10 hours the nanochannels are etched. When the nanochannels are etched open the chips are placed in a fresh DI solution for several days to remove the etchant and replace it by water. After this procedure the device is ready for use. In figure 4 a photograph of the fabricated device is shown.

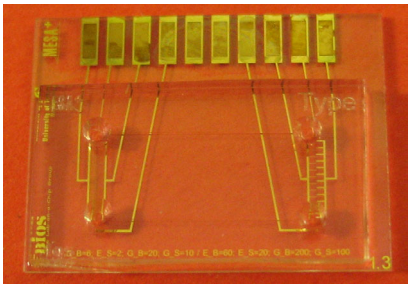

Figure 4: Device after fabrication.

6.3.2 Fabrication of fluidic connectors

To make the necessary fluidic connections between the microchannels and the rest of the setup (i.e. syringe pump and waste), self-sticking PDMS connectors are made. The connectors are based on a chips and tips article in Lab on a Chip [17] with some small alterations.

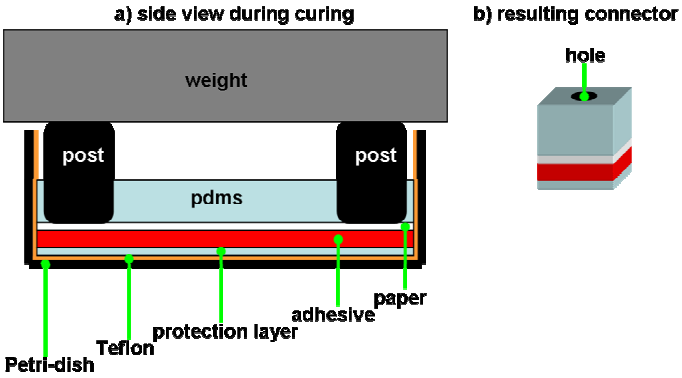

Figure 5: a) Side view of a large batch of connectors as encountered during curing. b) Self sticking PDMS connector after cutting and puncturing.

In figure 5 a side view of the connectors is given during and after fabrication. The fabrication starts by sticking a single layer of paper tissue (Kim Wipe Scientific) to

a sheet of double-sided adhesive plastic (Grace Bio-Labs Secure-Seal Adhesive, SA-S-1L). This is then cut in a circle with a diameter of approximately 6 cm and placed in a 6 cm diameter Teflon (3M) coated (to facilitate easy release after curing) Petri dish with the paper side up. The paper is used to improve the bonding between the double-sided adhesive and the PDMS by increasing the effective surface area. In the mean time approximately 15 ml PDMS (Sylgard 184 Silicone Elastomer, Dow-Corning) is prepared. A standard 1:10 weight ratio of hardener versus base is used. The PDMS is degassed and carefully casted onto the adhesive/paper combination. Prior to casting, 4 plastic posts were placed on the adhesive/paper combination to prevent it from curling up during curing. After casting a piece of metal is placed on top of the 4 posts as weight. The Petri dish is then again placed in the desiccator for degassing. This proves to be an important step since the paper contains lots of cavities where air can be trapped and in order to fully profit from the advantage of an increased surface area on the bonding all air in the paper/PDMS interface needs to be removed. After degassing the Petri dish is placed on a hot plate at 60°C for 4 hours. Slow curing by heating from the bottom of the dish also proved to be important in obtaining full-proof connectors. Curing inside an oven at 60°C was not successful, because it caused delamination at the paper/PDMS interface during operation. Possibly the curing of the paper/PDMS interface must occur prior to the rest of the PDMS, to minimize the intrinsic stress on this interface and prevent delamination. After curing the adhesive PDMS is pealed from the Petri dish. Then a hole is punctured through the PDMS using a blunt needle with a 200 μm inner diameter. Subsequently a square piece of adhesive PDMS is cut around the punctured hole. The plastic protection layer is removed from the adhesive and the connector is ready for use. Great care should be taken while puncturing the holes through the connector. If it is done too roughly the PDMS tears and the connector will leak.

6.3.3 Electrolyte solution preparation

All solutions are aqueous and prepared by dissolving in de-ionized water (Millipore Synthesis A10) which is in the remainder of this chapter referred to as DI. First a 100 mM KNO_3 (Sigma Aldrich 99+% ACS reagent) stock solution is prepared. This solution is subsequently diluted by pipetting specific amounts into 50 ml fresh DI. After preparation, the conductivities and pH of the different solutions are measured using a conductivity/pH meter (Mettler Toledo Seven Multi; conductivity probe: Inlab 730; pH probe: Inlab 413). The conductivity/pH meter is calibrated to both probes prior to the measurement. As electrolytes we used three different concentrations, namely 50, 100 and 200 μM with conductivities of 9, 16.22 and 32.1 $\mu S.cm^{-1}$, respectively. All solutions had a pH of approximately 6 prior to use.

6.3.4 Experimental setup and experimental procedure

In this section the experimental setup will be introduced. A schematic picture of the experimental setup is given in figure 6. Moreover the experimental procedure will be presented.

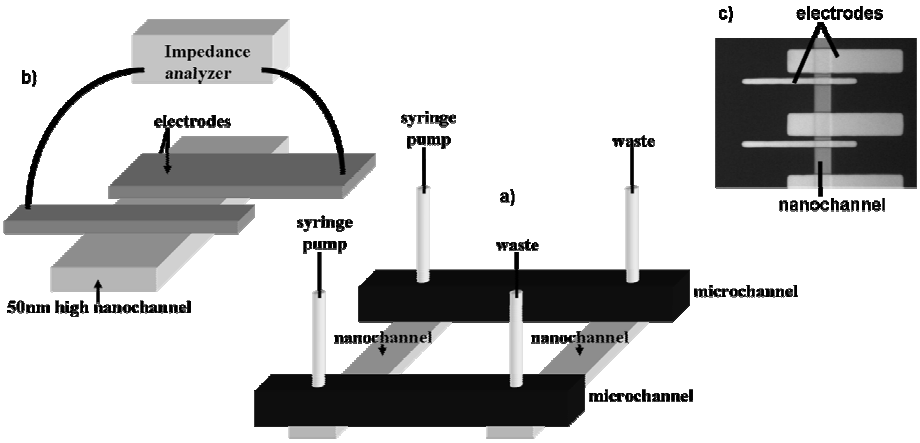

Figure 6: Schematical overview of the experimental setup. a) The fluidic setup where the two nanochannels are connected by two microchannels that are in turn connected to a two-stage syringe pump and two waste vials. b)The connection of the electrodes integrated in the nanochannel wall to an impedance analyzer. c) photo-micrograph of the fabricated device.

After the preparation described in section 6.3.1 the chip is connected to the syringes and waste vials using the home-made connectors described in 6.3.2, short fused silica capillaries (Up Church Sciecntific 360 µm OD and 100 µm ID) and flexible Tygon tubes (VWR International, R-3603, 1.99 mm OD and 190 µm ID). A schematical overview of the fluidics part of the setup is given in figure 7.

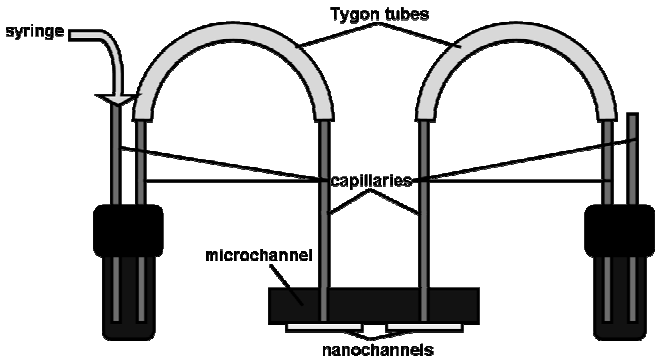

Figure 7: Schematical overview of the fluidics part of the experimental setup (not to scale).

Since the trapping of air bubbles near the micro/nanochannel interface is catastrophic for the device behavior a home-made air bubble trap is placed in between the syringes and the microchannels. This air-bubble trap consists of a 2 ml vial (Emergo, Chromacol vials 2 ml) capped by a PTFE/silicone rubber (Emergo,

PTFE/Silicone rubber cap) which is interfaced by puncturing two fused silica capillaries, a long (~30 cm) and a short (~5 cm) one, through the rubber caps. The long fused silica capillary connects via a fluidic connector (Upchurch Scientific, F330N with F-142N ferule, F-238 (capillary side) and F-142 (syringe side) tubing sleeves connected to a nanotight union (D-779-01)) to a 100 µl syringe (Hamilton, Gastight #1710). The vial is filled completely (this is important to prevent the formation of a large fluidic capacity in the system and hence a long delay between engagement of the syringe pumps and actual volume displacement in the microchannels) with the necessary solution prior to the experiment. If an air bubble arrives from the syringe to the vial it is stored in the vial and air bubble free liquid is passed towards the chip. The short fused silica capillary connects to an approximate 6 cm Tygon tube by simple insertion of the fused silica capillary into the Tygon tube. Tygon tubes are used because the tubing needs to be bended in order to connect the bubble traps to the chip. Tygon tubes are far more flexible than the glass capillaries and thus the connection can be kept as short as possible. This decreases the time it takes to replace electrolytes without generating stress on the PDMS connectors. This Tygon tube then connects to approximately 5 cm long fused silica capillaries again by simple insertion. The 5 cm long capillaries are connected to the fluidic connectors which are stuck to the PDMS part of the chip. Prior to sticking the connectors to the chip the fused silica capillaries were inserted into them and checked for clogging by flushing some DI through. On the other end of the microchannels the same combination of fused silica capillaries and Tygon tubing is used to connect the chip to the waste vials (Emergo, Chromacol vials 2 ml). Liquids are flushed through the microchannels by placing the syringes inside a syringe pump (Harvard Apparatus Pico Plus @300 nl/min). Since we use a wet etchant to open the nanochannels, usually the nanochannels do not have to be filled anymore prior to the experiment. In the case of the 82210 chip, however, the PDMS microchannels appeared to be leaky. After we found this out, the PDMS structure was peeled of and the glass chip was placed inside a polymer remover (Polygone 500) for an hour to remove any PDMS residue. Subsequently, the chip was rinsed with DI and stored in isopropanol for approximately a day. This was done to minimize the chances of clogging of the nanochannels upon drying. After this, the chip was rinsed with acetone and further cleaned as is usually done prior to the bonding to PDMS, as described above. Afterwards a newly prepared and cleaned microchannel structure in PDMS was bonded to the chip as described above again using plasma mediated bonding. Subsequently, methanol was evaporated in a dessicator for 6 hours. After this we filled the structure again in this case using ethanol which fills fluidic channels more easily than water because of a lower surface tension. Filling was done first at one side of one microchannel, after the microchannel was filled the hole on the other side of the microchannel was filled. This was kept filled for a ~5 minutes and than the other microchannel was filled in the same manner. This was done to prevent the enclosure of air somewhere halfway in the channel by two approaching filling fronts. Then the chip was put into DI for a day. After this the chip was connected to the rest of the setup as described above.

A change of electrolyte solution is performed as follows. Every time that electrolytes are replaced, the syringes are flushed with DI twice before filling with the new electrolyte. The bubble trap vials are replaced by vials containing the new electrolyte and the long fused silica capillaries connecting the syringes to the bubble

traps are flushed for 5 minutes at an elevated flow rate of 3 µl/min. The vials are again connected to the chip and after resetting the syringe pump to 300 nl/min, the syringes are connected to the vials.

When all fluidic connections are inspected on leakage by eye the chip is placed inside a home-made chip holder. This chip holder is used to make the necessary electrical connections to the impedance analyzer using gold springs (Easy Interconnect Specialties Inc.) that are integrated in a home-made Delrin block connector. It further consists of an anodized (black) aluminum base plate that is placed on the X-Y stage of an inverted microscope (Leica DM IRM). The microscope is used to inspect the structure on leakage and possible other problems (e.g. air bubble formation) during the experiment. The gold springs in the chip holder are soldered via a PCB to gold coaxial connectors that connect to the impedance analyzer (Princeton Applied Research Parstat 2263) which is controlled using a PowerSine software package (PowerSuite) via 1 m long coaxial cables. During the experiments the DC offset is set to zero and during the impedance versus time measurements each measurement point consists of the average of 10 measurements.

An actual typical experiment is performed as follows. First, a 100 µM solution is flushed through both microchannels. During this replacement of DI by the 100 µM KNO_3 solution, a sinusoidal potential wave with a frequency and AC-amplitude corresponding to the values applied during the remainder of the experiment is applied between the pairs of the electrode array. If at the frequency and AC-potential applied flow in nanochannel is induced the DI is replaced by the 100 µM KNO_3 solution. Since actuation was performed using an impedance analyzer the current resulting from the application of the sinusoidal potential wave is measured and the impedance is determined. The AC-potential is continuously applied and flushing of the 100 µM KNO_3 solution is continued until a stable current is reached. Then the solutions in both microchannels are replaced as described above. One microchannel is flushed with the 50 µM solution and the other with the 200 µM solution. If at the still continuously applied sinusoidal potential wave a net convective flow is induced (i.e. liquid is pumped through the nanochannel) the measured impedance will either increase or decrease. A decrease means that liquid flow was induced from the nanochannel end where the 200 µM solution is flushed pass and an increase means a liquid flow induced in the opposite direction. The time it takes for the impedance to change from the initial constant value to another is a measure of the time and space averaged velocity of liquid inside the channel. During the entire experiment the potential wave is applied and the resulting current at that specific frequency and AC-potential is recorded. Moreover, during the actual experiment (i.e. the measurement of a current change because of a replacement of the 100 µM solution by either the 50 or the 200 µM solution) the syringe pumps remain engaged to ensure a stable arrival of analyte at the nanochannel entrances.

6.4 Results and discussion

In this section the experimental results are presented and discussed by comparison to the theoretical results presented in chapter 5. In a first subsection measured impedance spectra at different electrolyte concentrations are presented. Then some plots of impedance measured as a function of time during pumping are presented and discussed and finally the resulting plot describing velocity versus driving frequency is presented and compared to theory.

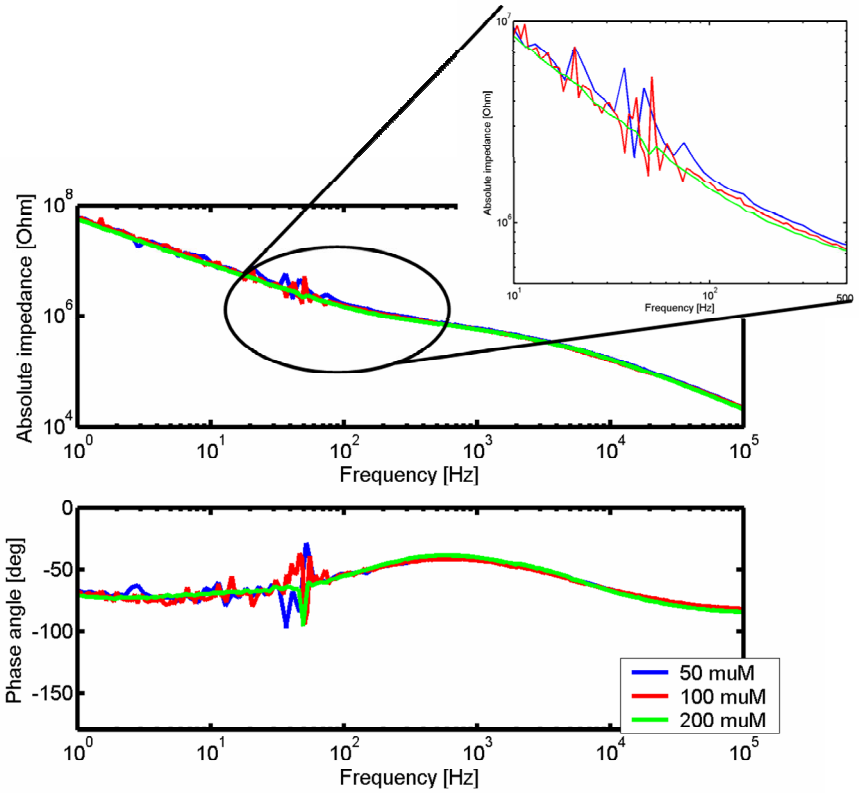

Figure 8: Measured impedance data at 140 mV for different electrolyte strengths inside the nanochannel. The data obtained for the 200 μM solution is 10 times averaged.

In figure 8 the measured impedance at an applied sinusoidal wave potential of 140 mV for the three different solutions is shown. The impedances were measured immediately after the AC-electrokinetic pump in the nanochannel has replaced the initial liquid (i.e. after the measured impedance as a function of time hits a constant

value). It is important to notice that the measured impedance indeed depends on the electrolyte concentration. When the measured impedance at the frequency of the smallest phase angle (i.e. if the impedance data at this point is compensated for a non-zero phase shift the compensated impedance value should be in close agreement with the resistive part of the impedance) is compared to the theoretical one (figure 2), it is interesting to see that the measured absolute impedance is approximately 2 times smaller (0.74 MΩ instead of 1.54 MΩ). The theoretical impedance is calculated using the measured electrode sizes and spacings and a measured channel width of 5.9 μm as described in chapter 3 of this thesis. In this calculation; which was based on the conductivity caused by the KNO_3 ions; ion exclusion and enrichment are already taken into account [18] using equation 3 in chapter 5. An increase in proton conductivity in the nanochannel originating from the pH 6 in the reservoirs and the ion enrichment in the nanochannels only amounts to approximately 10% of the conductivity caused by the enriched K^+ concentration, so this can not explain the large difference. At the moment it is not clear what causes this discrepancy, it could however, be caused by a considerable contribution of the Stern layer to the total conductivity as proposed by Stein and coworkers [14]. However, fortunately it does not bring the system in another operating regime since the amount of double layer overlap is hardly changed (the Debye length is at most decreased by 10%) In table 2 the measured and calculated magnitudes of the absolute impedance for the three different electrolytes are given.

Table 2: Measured and calculated values of the absolute impedance, |Z|, at 500 Hz for different KNO_3 concentrations.

concentration KNO_3 [μM]	**measured** |Z| [MΩ]	**calculated** |Z| [MΩ]
50	0.77	3.11
100	0.74	1.54
200	0.72	0.86

Although there is a large discrepancy between the calculated values and the actually measured one, clearly it is possible to discriminate between the three different ionic concentrations in the channels using the current setup. A final important observation to be made from figure 8 is that the phase for frequencies below 3 Hz decreases corresponding to a shift to more resistive behavior. This probably indicates Faradaic behavior and limits the applicability of the model applied currently to frequencies beyond 3 Hz. It should, however be noted that the impedance scans are obtained at 140 mV and the actual measurements are performed at a 400 mV sinusoidal amplitude which could potentially increase the lower frequency limit of our capacitive model.

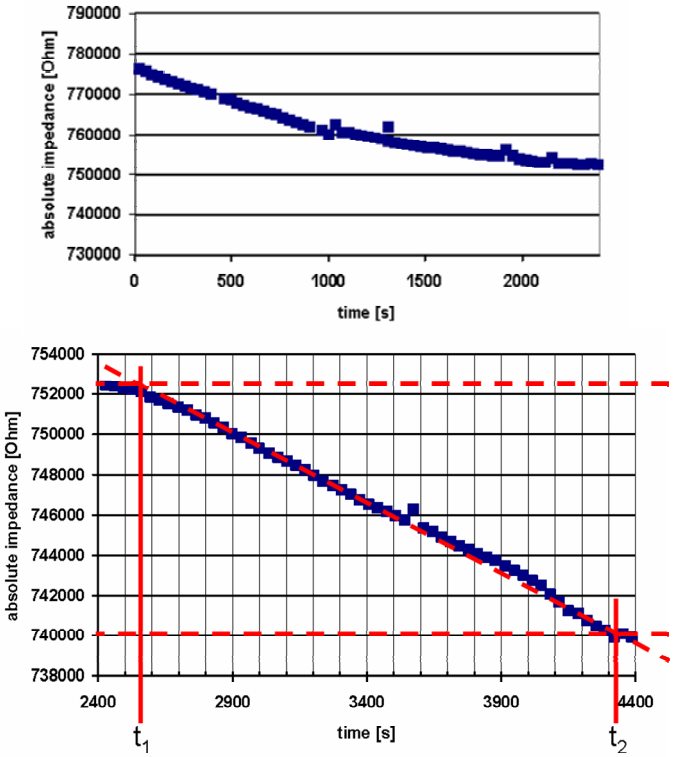

Figure 9: Measured absolute impedance at 500 Hz as a function of time. The upper plot shows the initial time trace indicating the replacement of DI by 100 µM KNO_3. The lower plot shows the impedance change caused by replacement of the 100 µM KNO_3 by 200 µM.

In the top plot of figure 9 a 500 Hz sinusoidal potential is applied immediately after flushing a 100 µM KNO_3 through the microchannels. Lowering of the impedance is observed corresponding to the replacement of DI by the 100 µM KNO_3 solution inside the nanochannel probably by the action of the AC-electrokinetic pump. In the first 2000 s the impedance decreases gradually towards a constant value around 2200 s. Once this constant value is reached the liquid in the microchannels is quickly replaced. At the end of the nanochannel that starts with a small electrode the 200 µM solution is flushed and at the end that starts with a big electrode the 50 µM solution is flushed. The lower plot of figure 9 shows the subsequent change in impedance, which was used to determine the average pumping velocity. After approximately 2500 s the absolute impedance again starts to deviate from the constant value and drops after approximately 4300 s towards a new constant value. This decrease corresponds to a flow from the small towards the big electrode and thus shows classical behavior at this applied frequency. The resulting velocity is, however low and comparable to a velocity

solely caused by diffusion. The change in impedance, however, appears not to be a square root function of time, which usually indicates diffusional transport. At the moment the reason for this is unclear.

At several frequencies no constant value was reached even after an hour of actuation and probably diffusional behavior was observed. An example of such a time trace measured at 200 Hz is given in figure 10. Here, after an initial constant value the impedance increases linearly as a function of the square root of time, a dependence

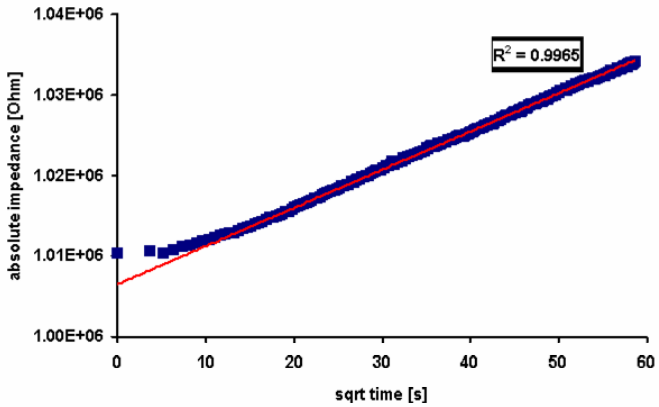

Figure 10: Absolute impedance at 200 Hz as a function of the square root of time displaying probably diffusional behavior.

which can indicate diffusional transport. This can be explained by a diffusional replacement of the 200 μM KNO_3 solution that was pumped into the channel at the 500 Hz experiment proceeding it by the 100 μM KNO_3 solution that at that time was flushed through the microchannels. Comparing the values of the absolute impedance obtained from figure 6 at 200 Hz for the 100 and the 200 μM KNO_3 solutions (i.e. 1.07 MΩ and 1.01 MΩ, respectively) shows that the measured impedance is approximately in that same range.

Finally, all velocities were calculated by dividing the length of the channel (4 mm) by the electrolyte replacement time. Figure 11 compares the resulting velocities for both chips to the numerical results obtained for the chip as presented in chapter 5 (with the following dimensions: big electrode, small gap, small electrode and big gap 11.4, 2, 2.6 and 8 μm, respectively)

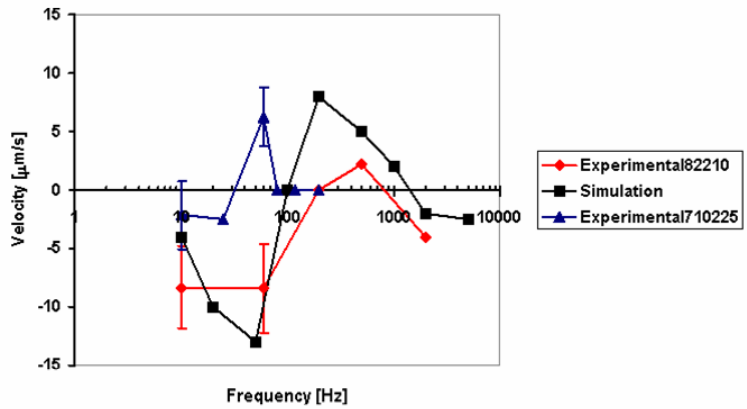

Figure 11: Measured and calculated velocity as a function of frequency at 400 mV. Positive velocities correspond to the classical direction of flow. The characteristic of the devices is given in subsection 6.3.1 of this chapter, details about the model can be found in chapter 5 of this thesis.

Figure 11 shows that the experimental data qualitatively follow the simulation results. For the 82210 chip all three operating regimes predicted in chapter 5 are observed. For the 710225 chip only the lower and the intermediate frequency regimes show up. An explanation for this could be that depletion in this device does not play a dominant role since the inter-electrode spacing at the small gap is approximately 7 times bigger making the axial migration of ions from this small gap possible without (or much less) depletion. Another important observation is a considerable shift of the 710225 experimental data to the left with respect to 82210 data. This could be explained by the increase in inter-electrode distance of a factor 7 in the 710225 chips, increasing the fluidic resistance with a factor of 7, via the increased RC time leading to lower optimal pumping frequencies. For the shift of the positive velocity peak this could be an approximately correct explanation. For the low frequency negative velocity peak the shift is unclear, since there is no clear lower frequency optimum.

Furthermore, the pumping velocity in the 82210 as compared to the 710225 chip is found to be approximately 4 times larger at the lower (10 to 60 Hz) frequencies. If ionic depletion would not play a role and the velocity would be dominantly determined by the electric field strength between the electrodes of a pair one would expect a factor 7 increase in velocity for the 82210 chip with respect to the 710225 chip. The fact that the velocity is increased only by a factor of 4 might indicate that depletion does play a larger role in the 82210 case than in the 710225 chip as can be expected from the smaller interelectrode distance. At intermediate frequency this 4 times increase is not seen, here even a decrease in velocity with the 82210 chip (at 500 Hz) as compared to the 710225 chip (at 60 Hz) is observed. It is at the moment not known what causes this and if this is a typical difference in velocity of the two chips. For this to be conclusive more measurements especially with the 82210 chip at the higher frequencies are necessary. Finally figure 11 shows for intermediate frequency (500 Hz) a shift to higher frequencies for the 82210 chip as compared to the

simulations. The reason for this is probably twofold. First the inter-electrode gap between electrodes of a pair is smaller than in the simulations (~1.4 times) which decreases the R term in the RC time. Secondly, the conductivity is 2 times bigger in the experimental case which also decreases R. Both effects combined would cause an approximate 3 fold shift in frequency, which is roughly in line with the observed shift in frequency (~ 2 fold), although it is impossible to exactly determine the points of optimal frequency from this limited data set. For the lower frequencies a shift in frequency is also hard to determine since obviously there are not enough measurement points. Theoretically, however as discussed in chapter 5, one would expect a smaller shift because since if the conductivity increase as compared to the theoretically expected one is indeed caused by Stern-layer conduction, this increase in conductivity is obviously in case of negative wall caused by cations. This should hardly influence the lower frequency behavior since behavior here is expected to be dominantly caused by anions.

6.5 Conclusion

An experimental setup has been constructed that successfully allows the determination of the pumping velocity induced by an AC voltage applied to asymmetric electrode arrays integrated into a 50 nm high nanochannel. Two chips with different electrode sizes and spacings are experimentally tested on their ability to generate a flow inside a nanochannel with double layer overlap by applying a low voltage AC potential to the asymmetric electrode array. The measured velocities as a function of frequency show bi-directional behavior and display a qualitatively comparable trend as the calculated velocities in chapter 5. Both a classical flow direction in the direction as observed in AC-EOF in microchannels as well as an opposed flow direction are observed experimentally, as predicted by theory in chapter 5. At an applied potential of 400 mV, far below the potential that induces electrochemical reactions in water, a maximum velocity of 6 μm/s was found in the classical direction and of 8 μm/s in the opposite direction. The results obtained illustrate that it is possible to manipulate liquids in nanochannels without the need of high pressures of high voltages at a reasonable linear flow rate.

References

1. Laser, D.J. and J.G. Santiago, *A review of micropumps.* Journal of Micromechanics and Microengineering, 2004. 14(6): p. R35-R64.
2. Yuan, Z., A.L. Garcia, G.P. Lopez, and D.N. Petsev, *Electrokinetic transport and separations in fluidic nanochannels.* Electrophoresis, 2007. 28(4): p. 595-610.
3. Schoch, R.B., J.Y. Han, and P. Renaud, *Transport phenomena in nanofluidics.* Reviews of Modern Physics, 2008. 80(3): p. 839-883.
4. Mpholo, M., C.G. Smith, and A.B.D. Brown, *Low voltage plug flow pumping using anisotropic electrode arrays.* Sensors and Actuators B-Chemical, 2003. 92(3): p. 262-268.

5. Prost, J., J.F. Chauwin, L. Peliti, and A. Ajdari, *Asymmetric Pumping of Particles.* Physical Review Letters, 1994. 72(16): p. 2652-2655.
6. Ramos, A., H. Morgan, N.G. Green, and A. Castellanos, *AC electric-field-induced fluid flow in microelectrodes.* Journal of Colloid and Interface Science, 1999. 217(2): p. 420-422.
7. Studer, V., A. Pepin, Y. Chen, and A. Ajdari, *Fabrication of microfluidic devices for AC electrokinetic fluid pumping.* Microelectronic Engineering, 2002. 61-2: p. 915-920.
8. Ramos, A., H. Morgan, N.G. Green, A. Gonzalez, and A. Castellanos, *Pumping of liquids with traveling-wave electroosmosis.* Journal of Applied Physics, 2005. 97(8): p. -.
9. Huang, X.H., M.J. Gordon, and R.N. Zare, *Current-Monitoring Method for Measuring the Electroosmotic Flow-Rate in Capillary Zone Electrophoresis.* Analytical Chemistry, 1988. 60(17): p. 1837-1838.
10. Bard, A.J. and L.R. Faulkner, *Electrochemical methods : fundamentals and applications*. 2nd ed. 2001, New York: John Wiley. xxi, 833 p.
11. Olthuis, W., W. Streekstra, and P. Bergveld, *Theoretical and Experimental-Determination of Cell Constants of Planar-Interdigitated Electrolyte Conductivity Sensors.* Sensors and Actuators B-Chemical, 1995. 24(1-3): p. 252-256.
12. Krommenhoek, E.E., J.G.E. Gardeniers, J.G. Bomer, A. Van den Berg, X. Li, M. Ottens, L.A.M. van der Wielen, G.W.K. van Dedem, M. Van Leeuwen, W.M. van Gulik, and J.J. Heijnen, *Monitoring of yeast cell concentration using a micromachined impedance sensor.* Sensors and Actuators B-Chemical, 2006. 115(1): p. 384-389.
13. Timmer, B., W. Sparreboom, W. Olthuis, P. Bergveld, and A. van den Berg, *Optimization of an electrolyte conductivity detector for measuring low ion concentrations.* Lab on a Chip, 2002. 2(2): p. 121-124.
14. Stein, D., M. Kruithof, and C. Dekker, *Surface-charge-governed ion transport in nanofluidic channels.* Physical Review Letters, 2004. 93(3): p. -.
15. Oosterbroek, R.E., *Modeling, design and fabrication of microfluidic components.* Proefschrift Universiteit Twente, ISBN: 90-365-1346-4, 1999.
16. Probstein, R.F., *Physicochemical hydrodynamics : an introduction*. 2nd ed. 1994, New York: John Wiley & Sons. xv, 400 p.
17. Mohanty, S. and D.J. Beebe, *Chips and Tips: PDMS connectors for macro to microfluidic interfacing.* Lab on a Chip, 2006. http://www.rsc.org/Publishing/Journals/lc/PDMS_connector.asp.
18. Plecis, A., R.B. Schoch, and P. Renaud, *Ionic transport phenomena in nanofluidics: Experimental and theoretical study of the exclusion-enrichment effect on a chip.* Nano Letters, 2005. 5(6): p. 1147-1155.

Chapter 7

Summary and Outlook

This chapter concludes this thesis. The important results are summarized and for each chapter an outlook for possible future work is presented.

General

Summary

In this thesis transport of liquid and dissolved ions in nanochannels generated by the application of AC-potentials to an array of pairs of asymmetric electrodes is described. The description is both theoretical; using a numerical model; and experimental; using a chip and experimental setup developed in this project. Moreover, a scope of the much broader field of nanofluidics is presented, discussing the basics, applications and the future of transport in nanofluidic channels.

Outlook

The device described in this thesis is believed to have an impact on the AC-electrokinetic research field. The reason for this is that it shows the behavior of an AC-electrokinetic device at the size limit where the channel structure has a size in the order of the typical interaction length of electrokinetic forces in aqueous solutions. Moreover, it shows very interesting behavior as a function of applied frequency with both a classical (as in microchannels) and a non-classical direction of flow that is confirmed by the physical model.

Chapter 2: Nanofluidic Transport: Principles and Applications

Summary

In this chapter transport through nanochannels was assessed, both of liquids and of dissolved molecules or ions. First we reviewed principles of transport at the nanoscale, which involved the identification of important length scales where transitions in behavior occur. The most important being the boundary length scale of 10 nm. Down to which upon downscaling liquid flow and electrokinetics concerning aqueous electrolytes can often be modeled using continuum theory (i.e. the Stokes and Nernst-Planck equations for the liquid flow and electrokinetic problems, respectively). Several important consequences that a high surface to volume ratio has on transport were also presented. We reviewed liquid slip, chemical equilibria between solution and wall molecules, molecular adsorption to the channel walls and wall surface roughness.

Recent developments and trends in the field of nanofluidics were identified, key differences with microfluidic transport addressed and applications reviewed. Hereby novel opportunities were accentuated, enabled by the unique behavior of liquids at the nanoscale. Applications of transport in nanochannels range from pumping and transport control to energy conversion and separation. The main general conclusion that can be drawn is that all applications exploit the large surface to volume ratio in nanochannels. Because of this large surface to volume ratio, interactions of the solution and-or molecules inside it with the walls become increasingly important for decreasing channel dimensions, sometimes also causing problems like adsorption. Moreover, in contrast to transport in microfluidics, in nanofluidics (preferably with double layer overlap) transport control of individual charged molecules becomes feasible. Finally, liquid transport is always accompanied by a net charge displacement inducing potential and/or pressure gradients which have an increasing influence on transport properties for decreasing channel height.

Outlook

Reviewing a decade in which many interesting novel devices in the rapidly expanding field of nanofluidics have been presented, brings us to the conclusion that nanofluidics will most likely play a significant role in various application areas in years to come. We envision an important role of nanofluidics in the following fields:

- Analytical chemistry and biochemistry: From single molecule detection towards spatial and temporal control of individual molecules inside aqueous solutions such as proteins and DNA molecules.
- Liquid transport and dosing: By exploring and exploiting liquid slip conditions to engineer precise and highly efficient transport and dosing systems.
- Energy conversion: Nanofluidics holds potential for high power density energy conversion at high efficiency if liquid slip is introduced.

Finally, with improved control of structures on the nanoscale made possible by nanotechnological developments, more phenomena and applications in the above fields are anticipated.

Chapter 3: Design and Fabrication of Traveling Wave Driven Pumps in Nanochannels

Summary

In this chapter the design and fabrication of traveling wave driven pumps (TW-EOF) in nanochannels is presented. Both the design and the fabrication also apply to the technologically more simple pumps which are actuated by AC voltage driven asymmetric electrode arrays (AC-EOF). Design choices based on technological, physical and time-management considerations are discussed thoroughly. All fabrication steps are explained and described using relevant cross sections of the device during subsequent fabrication steps. Furthermore, the resulting device is tested both electrically and optically. The results of these tests show that the device behaves within the window of the demands given at the start of this chapter. Optical tests show an 18% and a 30% difference in lateral dimensions of the nanochannels and the electrodes, respectively, as compared to the designed masks.

Outlook

Although experiments have been performed with the AC-EOF device as discussed in the following chapters of this thesis, experiments with the TW-EOF device of which the manufacturing procedure is discussed in this chapter were up to now not performed, simply because of time limitations. In the following months we hope to perform the first experiments using this device. Experimental results will be compared to some preliminary simulation results, which just as in the AC-EOF devices showed both a non-classical flow direction (at low frequencies) and a classical flow direction.

Chapter 4: Rapid Sacrificial Layer Etching for the Fabrication of Nanochannels with Integrated Metal Electrodes

Summary

In this chapter a rapid etch method to surface-micromachine nanochannels with integrated noble metal electrodes using a single metal sacrificial layer is presented. The method is based on the galvanic coupling of a chromium sacrificial layer with gold electrodes, which resulted in a 10-fold increase in etch rate with respect to conventional single metal etching. The etch process was investigated and characterized by optical and electrochemical measurements. This led to a theoretical explanation of the observed etch rate based on mass transport. Using this explanation we derived some generic design rules for nanochannel fabrication employing sacrificial metal etching.

Outlook

To further investigate the kinetics of the etch process we performed polarization measurements. These measurements indicated that etch rates can be further increased by a factor of two by applying an external potential to the metals. The theory we developed enables predictions of etching behavior for future devices using externally applied potentials. However, to make a more complete overview of different sacrificial and/or electrode materials, additional experiments are necessary. Such an overview would improve the applicability of the here described technique to a broader set of devices employing different sacrificial and/or electrode materials.

Chapter 5: Bi-directional Pumping in Nanochannels Using Integrated Asymmetric Electrode Arrays: Modeling

Summary

Bi-directional flow induced at asymmetric electrodes integrated in a 50 nm high nanochannel was demonstrated theoretically by numerical modeling using a finite element method. Ionic transport was modeled using the full Nernst-Planck equations considering the influence of diffusion, migration and convection on transport. Flow of liquid and ions were viscously coupled using the Stokes equations. A pulsative flow with a net direction was found to be induced by the application of sinusoidal waves to the electrodes. The situation of both overlapping and thick non-overlapping double layers was simulated. To interpret the results, an intuitive picture of the device operation was sketched and analytical equations for the frequency behavior were given.

In the case of overlapping double layers (at a reservoir concentration of 100 μM) three optimal driving frequencies were found, showing both negative and positive (i.e. corresponding to the direction classically observed in microchannels) velocities. The optimal frequencies that were found are around 50 Hz, 200 Hz and 2 kHz, showing a negative, a positive and again a negative direction of flow, respectively.

In the case of non-overlapping double layers (at a reservoir concentration of 1 mM) only two optimal driving frequencies were found, showing both positive and negative velocities. The optimal driving frequencies are around 100 Hz and 2 kHz, showing a positive and a negative direction of flow, respectively.

The induced flow velocity; as a function of applied AC potential; showed saturation behavior probably beyond 300 mV. This is in contrast to classical behavior observed in microchannels where the velocity shows an approximate squared relation with the applied AC potential.

Outlook

This model is very suitable for predicting the pumping efficiency of a given channel and electrode configuration. Since at the moment it is not yet known what the optimal geometry is in case of a system with overlapping double layers, an optimization routine to determine this geometry is very useful. Moreover, since an induced flow in a TW-EOF device is governed by the same equation set, modeling of this device using the available routine is feasible as well and is highly interesting. Moreover, this method would allow for the simulation of AC-EOF in microchannels. This could for the first time show the influence of a non-zero wall potential on the device operation. However, since microchannels have a bigger volume, the number of necessary finite elements increases. This demands more computational resources and probably simulation time. At the moment tests with the current computer indicate that the limit for the channel height is approximately 1 μm. To approach this channel height, however, the size of the finite elements had to be increased quite drastically, making the results at the moment not reliable enough.

Chapter 6: Bi-directional Pumping in Nanochannels Using Integrated Asymmetric Electrode Array: Experiments

Summary

In this chapter we describe experiments determining the pumping velocity induced by asymmetric electrode arrays integrated into a 50 nm high nanochannel. A setup was built and successfully employed. Theory explaining the measurement method was formulated and compared to the experimental results. Two chips with different electrode sizes and spacings (electrode sizes are comparable, however the spacings differ approximately one order of magnitude) were experimentally tested on their ability to generate flow inside a nanochannel with double layer overlap by applying a low voltage AC potential. The velocities measured as a function of frequency show a trend qualitatively comparable to the calculated velocities in chapter 5. A bi-directional flow was observed, with both a classical flow direction (known form microchannels) and an opposite flow direction, depending on the applied frequency. At applied potentials of 400 mV maximum velocities of 6 μm/s and 2 μm/s were found in the classical direction at driving frequencies of 60 and 500 Hz for the long-spaced and the short-spaced electrodes, respectively, and of 3, 8 and 5 μm/s in the opposite direction at driving frequencies of 25, 60 and 2000 Hz for the long-spaced at low frequencies and the short-spaced at low and high frequencies, respectively.

Outlook

More measurements at different frequencies are necessary to more exactly determine the points of optimal driving frequency and flow reversal. Also the influence

of applied AC-potential and ionic concentration on device behavior needs yet to be assessed experimentally.

Concluding remarks and general outlook for AC- electrokinetic pumping in nanochannels

In the previous, the application of bi-directional pumping using AC-electrokinetics is presented. Besides fluid transport, it was found that potentially a new separation technique for ions can be developed based upon AC-electrokinetics. Since the frequency, at which ions in the device are transported most efficiently, depends on the mobility of the ions, this device could possibly be used to separate ions and/or charged molecules based on mobility by tuning the frequency. Here ions or charged molecules, to which the frequency is tuned, travel faster and in larger amounts in the axial direction through the channels than other ions or charged molecules. At the moment the device seems to be most interesting for the separation of ions or charged molecules with high mobility (i.e. at least an order of magnitude higher than the background electrolyte) in case of cations or positively charged molecules. For anions or negatively charged molecules the choice of mobility is less important since ion-exclusion prevents complete shielding of the positive electrodes (i.e. to which the anions and/or negative charged molecules are attracted). An example of a negatively charged molecule would be DNA, where in confined channels the mobility is found to be a function of length. The positive species could then be separated at a frequency higher than the high frequency optimum (>1 kHz) which can also be lowered by choosing an electrolyte composed of lower mobility cations. The second species could probably be separated in all three frequency regimes. The frequency, however, should be matched to the time it takes for an ion or molecule of interest to travel from one electrode to another. This makes the TW-EOF device a better candidate for this application since in this device all electrode spacings are equal and as such a more constant transport rate of the ions or molecules of interest is expected. The reason why cationic or positive molecules can only be separated in the high frequency regime is that otherwise the cations in the background electrolyte (which will probably be available in a larger amount than the analyte ions or molecules) will shield potentials on the electrode before an ion or charged molecule of interest can reach the next electrode. This makes the movement of the ion or molecule of interest through the system very inefficient, preventing separation based on the AC-electrophoretic effect. To conclude, this new method of separation could be named AC-electrophoresis and deserves further research in a future project.

Abstract

AC Electro-osmosis (AC-EO) is the movement of liquid induced by the application of alternating current potential waves to wall-integrated electrodes. In symmetric systems (both spatial and temporal) the resulting liquid flow is alternating in direction with a zero offset. To obtain directionality asymmetry is added either in space (by electrode geometry) or in time (by applying asymmetric AC signals). This thesis is written as part of the Nanoned PhD project: "Flow sensing and control in nanochannels". This project was set out to explore new ways of generating and monitoring flow in nanochannels. In this thesis design, fabrication, experiments and modeling of a system employing AC-EO in a 50 nm high slit-like nanochannel are described. Asymmetry in this device was obtained by an asymmetry in electrode size.

To provide reference, in chapter 2 existing theory and applications concerning transport in nanofluidic channels are described. Literature on the subject is dominated by electrokinetic phenomena and applications employing electrokinetics. This can be explained by at least two reasons. First, electrokinetics scale favorably with decreasing channel dimensions. Second, nanochannels have one or more of their dimensions close to the Debye length. This has lead to new applications and leads to deviated behavior as compared to transport in microchannels. This deviating and most interesting behavior has triggered us to explore AC-EO in nanochannels with the channel height close to the Debye length.

In chapter 3 the design and fabrication of the device is described. Here a description is given of a technologically more challenging; namely a traveling wave driven; version of the AC-EO device.

During fabrication a method to galvanically enhance the etch rate of the nanochannels was explored. It was found that the etch rate of a chromium sacrificial layer could be enhanced approximately 10 times by galvanic coupling to noble metal electrodes integrated in the channel wall. This brought the etch time down to approximately 10 hours for a 4 mm long channel. To better understand this enhanced etch rate and possibly take advantage of it theory was developed. Both the method and theory are described in chapter 4.

Because of the possible complex nature of the device behavior and experimental results that were hard to interpret, we decided to model the behavior using a finite element model. The model consisted of a strongly coupled set of equations to describe electrostatics (Poisson and part of the Nernst-Planck equations), ionic (Nernst-Planck equations) and fluidic (Stokes equations for incompressible flow) transport. A description of the model and results can be found in chapter 5 of this thesis. The model indeed predicted complex, but interesting device behavior. Especially the behavior as a function of applied frequency turned out to be very different than that observed in microchannels. Three different frequency regimes were predicted. At low frequencies ($f < 100$ Hz) the AC-EO effect was mainly concentrated at the electrode edges and was predicted to be reversed as compared to standard behavior in microchannels; at intermediate frequencies ($100 \text{ Hz} < f < 1000$ Hz) the AC-EO effect was predicted to

behave quite similar (including the direction) to that in observed in microchannels; and at high frequencies (f > 1000 Hz) again the flow direction was predicted to be reversed and was mainly dominated by depletion effects. The predicted velocity was in the order of 10 $\mu m.s^{-1}$.

Since a defined electrolyte concentration at the nanochannel interface is important in interpreting the experimental results a reliable fluidic connection to the *outside world* is important. This, however, proved to be quite challenging. PDMS as a core material for the microfluidic network interfacing the nanochannels to the experimental setup appeared hard to integrate into the fluidic part of a chip holder. This was finally solved by fabricating PDMS disposable connectors. Flow detection was performed by an impedance measurement simultaneously with actuation. Measured velocity as a function of frequency was in qualitative agreement with the theoretically predicted behavior; showing as predicted flow reversal as a function of frequency. The measured velocities were between 2 and 10 $\mu m.s^{-1}$ at an applied amplitude of 400 mV.

Samenvatting

AC Electro-osmose (AC-EO) is de vloeistof beweging in een kanaal opgewekt aan elektrodes in de kanaalwand die worden aangestuurd met periodieke potentiaal golven. In symmetrische systemen (zowel in plaats als in tijd) varieert de resulterende vloeistof stroming van richting en is er geen netto component. Om een netto richting te geven aan het transport wordt er een asymmetrie aangebracht, in plaats (elektrode geometrie) of in tijd (door asymmetrische periodieke signalen aan te leggen). Dit proefschrift is geschreven als onderdeel het Nanoned AIO project: “Flow sensing and control in nanochannels”. Het doel van dit project was om nieuwe manieren van vloeistoftransport en detectie in nanokanalen te onderzoeken. In dit proefschrift wordt het ontwerp, de fabricage, het experimenteren met en het modelleren van een AC-EO systeem in een 50 nm hoog nanokanaal beschreven. Directionaliteit is in dit systeem verkregen door een asymmetrie in elektrode grootte.

Om een referentiekader te schetsen zijn in hoofdstuk 2 bestaande theorie en toepassingen van het transport in nanokanalen beschreven. De literatuur over dit onderwerp wordt voor een aanzienlijk gedeelte bepaald door elektrokinetische verschijnselen en toepassingen. De reden hiervoor is minstens tweeledig. Ten eerste schalen elektrokinetische effecten gunstig bij afnemende kanaalgroottes. Ten tweede hebben nanokanalen een of meer afmetingen met een grootte die vergelijkbaar is met de Debye lengte. Dit laatste heeft al geleid tot nieuwe toepassingen en leidt tot afwijkend gedrag in vergelijking met het transport in microkanalen. Dit afwijkende, maar zeer interessante gedrag heeft ons aangezet om AC-EO in nanokanalen met een kanaalhoogte vergelijkbaar met de Debye lengte te onderzoeken.

In hoofdstuk 3 is het ontwerp en de fabricage van het systeem beschreven. Het systeem beschreven in dit hoofdstuk is een lopende golf versie van het AC-EO systeem welke technologisch ingewikkelder, maar vergelijkbaar is met het systeem met asymmetrische elektroden.

Tijdens de fabricage is geëxperimenteerd met een methode waarbij de etssnelheid van de nanokanalen galvanisch wordt versneld. Door een *sacrificial* laag van chroom galvanisch te koppelen aan de gouden electrodes in de kanaalwand werd de etssnelheid ongeveer met een factor 10 verhoogd. Op deze manier konden de 4 mm lange nanokanalen opengeëtst worden in ongeveer 10 uur. Om het begrip en dus de toepasbaarheid van de techniek te verbeteren is er een theorie ontwikkeld die het versnelde etsgedrag kan verklaren. Zowel de methode als de theorie worden uitvoerig beschreven in hoofdstuk 4.

We hebben besloten het gedrag van het systeem te modeleren met behulp van eindige elementen simulaties vanwege het mogelijk complexe gedrag en de interpreteerbaarheid van de experimentele resultaten. Het model bestond uit sterk gekoppelde vergelijkingen voor elektrostatica (Poisson en een gedeelte van de Nernst-Planck vergelijkingen), ionisch (Nernst-Planck vergelijkingen) en vloeistof (Stokes vergelijkingen met onsamendrukbaarheid aanname) transport. Een beschrijving van het model en de resultaten staan in hoofdstuk 5 van dit proefschrift. Het model voorspelde

inderdaad complex, maar interessant gedrag. In het bijzonder de snelheid als functie van de frequentie bleek zeer anders te zijn dan in microkanalen. Er werden drie verschillende frequentiegebieden gedefinieerd. Bij lage frequenties ($f < 100$ Hz) was het effect voornamelijk geconcentreerd aan de uiteinden van de elektroden en was de richting tegengesteld aan deze bekend van de literatuur over AC-EO in microkanalen; ook bij hoge frequenties ($f > 1000$ Hz) was het effect tegengesteld gericht en werd voornamelijk gekenmerkt door depletie gerelateerde effecten; echter bij tussenliggende frequenties ($100 \text{ Hz} > f > 1000$ Hz) bleek het AC-EO effect vergelijkbaar van aard en richting te zijn met het AC-EO effect in microkanalen. De voorspelde snelheid bij een opgelegde spanningamplitude van 400 mV lag in de orde van 10 $\mu m.s^{-1}$.

Doordat een goed gedefinieerde elektrolyt concentratie aan de uiteinden van het nanokanaal van belang is bij een juiste interpretatie van de meetresultaten, is een betrouwbare en robuuste vloeistof aansluiting met de *buitenwereld* van belang. Dit bleek echter een grote uitdaging te zijn. Het bleek lastig om de microkanalen gemaakt in PDMS met behulp van een chiphouder lekvrij aan te sluiten op de rest van de experimentele opstelling. We hebben dit uiteindelijk opgelost door zelfklevende aansluitingen te maken in PDMS. De uiteindelijk geïnduceerde gemiddelde vloeistofsnelheid werd bepaald door de elektrische impedantie te meten tijdens actuatie. De zo bepaalde vloeistofsnelheid bleek kwalitatief overeen te komen met de theoretische voorspelling, waarbij ook draaiing van de vloeistofrichting geobserveerd werd als functie van de frequentie. De gemeten snelheid bij een opgelegde spanningamplitude van 400 mV lag tussen de 2 en 10 $\mu m.s^{-1}$, wat vergelijkbaar is met de voorspelde waarden voor snelheid.

List of publications

1. *Fast etching of sacrificial galvanic coupled metals for nanochannel fabrication: experiments and theory.* In: Eleventh International Conference on Miniaturized Systems for Chemistry and Life Sciences - The proceedings of microTAS 2007 Conference, 7-11 october 2007, Paris. pp. 515-517. Micro Total Analysis Systems 1. Chemical and Biological Microsystems Society. ISBN 978-0-9798064-0-7 (**Chapter 4**)

2. *Rapid Sacrificial Layer Etching for the Fabrication of Nanochannels with Integrated Metal Electrodes*, Lab on a Chip, 8(3), 2008 (**Chapter 4**)

3. *Ion pumping in nanochannels using an asymmetric electrode array*. In: 12th International Conference on Miniaturized Systems for Chemistry and Life Sciences, 12-16 Oct 2008, San Diego, California. pp. 206-208. Micro Total Analysis Systems 1. Chemical and Biological Micro Systems Society. ISSN 1556-5890 ISBN 978-0-9798064-1-4 (**Chapters 5 and 6**)

4. *Nanofluidic Transport: Principles and Applications, Nature Nanotechnology*, manuscript under consideration (**Chapter 2**)

5. *Bi-directional Pumping in Nanochannels Using Integrated Asymmetric Electrode Arrays*, manuscript in preparation (**Chapters 5 and 6**)

Dankwoord

Met dit dankwoord sluit ik vier boeiende jaren van mijn leven af. Tijdens mijn individuele onderzoeksopdracht die ik gedaan heb bij Björn Timmer kwam ik in contact met de BIOS groep, toen nog onder leiding van Piet Bergveld. Om redenen die ik zelf eigenlijk niet goed begrijp heeft het gedrag van vloeistoffen op de microschaal, of kleiner, me vanaf dat moment enorm gebiologeerd. Tijdens mijn afstudeeropdracht bij Erik "*vaak figuurlijk, maar soms ook letterlijk met zijn hoofd in de wolken*" Faber werd deze interesse alleen maar groter. Toen Wouter Olthuis mij vroeg of ik interesse had voor een promotieonderzoek (waarvoor dank) hoefde ik daar niet lang over na te denken. Na één gesprek met Jan "*brainstorm*" Eijkel was ik om en heb ik gekozen voor het project waarvan de resultaten zijn beschreven in dit proefschrift.
Ik wil Albert hartelijk bedanken voor zijn kritische en razendsnelle manier van terugkoppelen op mijn werk. Daarnaast wil ik je bedanken voor het opzetten van en sturing geven aan een zeer dynamische en veelzijdige leerstoel waarin het een plezier is om te werken.
Jan E bedank ik voor zijn eeuwige enthousiasme. Ik heb erg veel van en door jou geleerd. Dit dank ik aan jouw manier van begeleiden, waarbij je me erg vrijgelaten, maar altijd voorzien hebt van jouw veelal zeer omvatrijke visie op uiteenlopende onderwerpen. Het ging hierdoor een aantal keren bijna mis en heeft me van tijd tot tijd de nodige stress opgeleverd, maar het zijn ervaringen/lessen geweest die ik mijn leven niet meer zal vergeten.
Johan "*tweezers*" Bomer dank ik voor zijn werk in de cleanroom. Het was altijd weer indrukwekkend je daar aan het werk te zien. Vaak was je met meerdere projecten tegelijk bezig, maar je zag er altijd uit als een vis in het water.
De tukkerclan (Paul "*de celfluisteraar alias Bob de Sloper*" ter Braak, Floor "*theeleutje alias knutsel*" Wolbers, Loes "*ik heb geen microohfoohn noohdig dit goat zooh wah*" Segerink) dank ik voor de lachmomenten in de koffiekamer. Mathieu "*promoveren en computers zijn appeltje eitje*" Odijk voor de interessante en soms ook diepgaande gespreken op onze kamer. Jan "*ik heb overal over nagedacht en zo niet ga ik dat bij dezen doen*" van Nieuwkasteele, dank je voor je interessante theorieën over van alles en nog wat en je kennis op het gebied van microtechnologie en microscopen in het bijzonder. Hermine "*regelt het wel*" Knol dank je voor je hulp met de administratieve dingen en het uit de brand helpen als ik weer eens iets vergeten was. Georgette "*ik maak de haan wakker*" Salieb-Beugelaar en Ana "*kwebbel*" Valero dank jullie dat jullie me af en toe bij jullie werk betrokken, ik heb zo ook wat kunnen opsteken bij andere projecten. De rest van de groep (Egbert, Ad, Daniel, Lingling, Mingliang, Masood, Songyou, Ganeshram, Iris, Evelien, Cathelijn, Rex, Arpita, Edwin, Hans, Istvan, Severine, Eddy, Richard) inclusief oude leden dank ik hartelijk voor de gezelligheid en/of de input in mijn project. Jacob "*hé kan het nog iets zachter*" Bart, dank je voor de goede gesprekken die we gehad hebben. Ik vind jouw manier van omgaan met het geloof, waarbij je anderen in hun waarde laat, maar er toch duidelijk voor uitkomt indrukwekkend en een voorbeeld voor anderen.

Paul dank je voor de leuke momenten en je vriendschap. Vanaf het moment dat we letterlijk met elkaar in contact kwamen hebben we altijd erg kunnen lachen, het is geweldig iemand in de buurt te hebben met hetzelfde gevoel voor humor.
Tijdens het project heb ik het genoegen gehad om geholpen te worden door verschillende studenten met elk een zeer uiteenlopend karakter. Yang, ik verbaas me soms nog wel eens over de hoeveelheid werk (en dan vooral schrijfwerk) wat jij kon neerzetten in een korte periode. Cristian, I have learned a lot from you, this was partly due to your character, sometimes your stubbornness strained my explanation skills and patience to and sometimes beyond the maximum, but your original point of view enabled me to look at several parts of the project from a broader perspective. Marco, tenslotte, bedankt voor je bijdrage. Jij bent in staat erg snel op een hoog niveau aan de slag te gaan. Ook kon je me af en toe vragen stellen die me erg aan het denken zetten, ik heb daardoor veel geleerd in een korte tijd, mijn dank daarvoor. Je strakke manier van plannen die nodig was, omdat je “ook nog ff moest kunnen relaxen” was mooi om te zien.
Mijn ouders wil ik bedanken voor de mogelijkheid tot studeren, maar vooral voor het bieden van een leerzame, prikkelende en vooral warme omgeving tijdens mijn jeugd. Marloes, zussie, dank je voor je lieve karakter. Thijs, broedâh, achter je af en toe wat ruwe manier van doen, zit een mooi en erg gevoelig mens, dank je. Opa Bob, dank u dat u mij al op zeer jonge leeftijd hebt laten kennis maken met techniek.
Erica, lieffie, jou wil ik uit het diepst van mijn hart danken voor je liefde en je geduld met mij en mijn werk. Ik weet dat vooral het laatste half jaar zwaar voor je is geweest, dank je dat je altijd weer in staat bent me weer met mijn gedachten bij jullie te krijgen.
Amber, papa’s schatje, wat ben je lief. Jij zorgt er voor dat ik me af en toe weer kind voel en dat gevoel is onbetaalbaar, dank je.
Uk, we hebben alleen nog kennis kunnen maken via echo’s en de nodige trappen via mama’s buik. Ik ben niet altijd bij je geweest met mijn gedachten, ik hoop dit straks als je geboren wordt allemaal goed te maken en hoop dat ik net zo’n fijne band met je kan opbouwen als met je grote zus.